Analytical and Numerical Investigation of an Intracellular Calcium Dynamics Model

Dissertation

zur Erlangung des akademischen Grades

doctor rerum naturalium
(Dr. rer. nat.)

von **M. Sc. Jared Ouma Okiro**
geb. am: 18.08.1973 in Kisumu, Kenya

genehmigt durch die Fakultät für Mathematik

der Otto-von-Guericke-Universität Magdeburg

Gutachter:

Prof. Dr. Mostafa Bendahmane

Prof. Dr. Nagaiah Chamakuri

Prof. Dr. Gerald Warnecke

eingereicht am: 02.11.2016
Verteidigung am: 02.05.2017

Analytical and Numerical Investigation of an Intracellular Calcium Dynamics Model

Dissertation

Submitted for the academic degree

doctor rerum naturalium
(Dr. rer. nat.)

by: **Jared Ouma Okiro, M. Sc.**
born on: 18.08.1973 in Kisumu, Kenya

Approved by the Faculty of Mathematics

Otto-von-Guericke-University, Magdeburg, Germany

Referees:

Prof. Dr. Mostafa Bendahmane

Prof. Dr. Nagaiah Chamakuri

Prof. Dr. Gerald Warnecke

Submitted on: 02.11.2016
Defended on: 02.05.2017

Acknowledgements

First and foremost I would like to thank the Almighty God for the gift of life and sustenance during the journey to this thesis. I am greatly indebted to my supervisor Professor Gerald Warnecke who has not only encouraged me but has given his remarkable suggestions and invaluable supervision throughout my thesis. His advices and constructive criticism have always been the driving force towards the successful completion of my thesis. I am also grateful to him for the many opportunities I had during my thesis work to attend international meetings and conferences and interact with other researchers from all over the world.

I owe special thanks to my second supervisor Professor Nagaiah Chamakuri for his assistance with numerous aspects of the preparation of this thesis, especially on numerics. This work would be unthinkable without his guidance and persistent help with programming and usage of the public domain software package DUNE.

I would also like to thank Professor Michel Pierre for the state of the art lectures (3rd Spring School, University Duisberg-Essen, 2011) on the question of global existence of solutions to reaction diffusion systems with two important natural properties. This contributed immensely to the analysis work in this thesis.

I am very grateful to Dr. Vincent Ssemaganda for his untiring mentorship throughout the research work. I would like to express my special thanks to Dr. Walfred Grambow for his technical assistance. I also express my deepest appreciation to the staff and students of the Institute for Analysis and Numerics for providing a pleasurable and stimulating environment to carry out this research. Many thanks also to all my friends and colleagues for their cooperation, guidance and moral support.

I am overwhelmingly grateful to the German Academic Exchange Service (Deutscher Akademischer Austausch Dienst - DAAD) for funding this work. Furthermore, I sincerely thank the developers of the software “Distributed and Unified Numerics Environment” (DUNE) for providing their PDE and iterative solver code as open source to the public.

Finally, a special profound acknowledgement go to my wonderful loving wife Edna whose forbearance and emotional support have been invaluable. I owe whole hearted gratitude to my mother and parents in law for their encouragement and immeasurable support throughout this work. To my beloved daughter Jean and son Eden, this thesis is dedicated.

Abstract

Calcium ions are an important second messenger in living cells. Indeed calcium signals in the form of waves have been the subject of much recent experimental interest. In this thesis we investigate a model for intracellular calcium dynamics. The model is comprised of a system of semilinear reaction-diffusion equations with discontinuities in the source terms. The equations in two-dimensions model the diffusion, reaction, binding and membrane transport of calcium ions within a cell.

We prove global existence of strong solutions for this system using semigroup theory and the invariant regions approach. Our results give a mathematical justification to the widespread use of computer simulations for this model and other related ones.

The real challenge of the computations for calcium dynamics is that the source terms in the model equations make the problem highly stiff. The channels open and close on a very short time scale and they are highly localized in space while there are intermittent time periods and spatial regions with slight change in activity.

We present high resolution numerical solutions in space and time for this calcium dynamics model. We consider the model using discontinuous Galerkin (DG) methods which are attractive because of the following features: their formal high-order accuracy, their nonlinear stability, their high parallelizability, their ability to handle complicated geometries and their ability to capture the discontinuities or strong gradients of the solution without producing spurious oscillations. Our numerical implementation is based on the software package called DUNE, which is an open source to the public written in C++.

The numerical results are demonstrated for several higher order spatial methods. These have involved using the DG method of weighted interior penalties (WIP) in space and the adaptive and higher order linearly implicit Runge-Kutta methods of Rosenbrock type for the time integration. The WIP method we adopt is more robust in handling heterogenous diffusion, i.e., where the diffusion coefficients takes locally small values leading to reaction dominated regimes, which suits well the model equations. A hybrid method that couples the solution of the deterministic and stochastic part of the model is adopted. By generating adaptive grids a priori and automatically adapting the time steps to the proper scales during the transition of channel states, the evolution of calcium ions and buffer concentrations have been resolved accurately.

To ensure computational efficiency, the deterministic and hybrid models are implemented using parallel numerical methods based on domain decomposition algorithms. Our results from the parallel version of the simulation have demonstrated the efficient parallelizability of DG methods resulting in the achievement of good parallel efficiency.

Zusammenfassung

Kalziumionen sind ein wichtiger sekundärer Botenstoff in lebenden Zellen. In der Tat sind Kalziumsignale in Form von Wellen das Thema vieler neuer experimenteller Interessen. In dieser Arbeit untersuchen wir ein Modell für die intrazelluläre Kalziumdynamik. Das Modell besteht aus einem System von semilinearen Reaktions-Diffusionsgleichungen mit Unstetigkeiten in den Quelltermen. Die Gleichungen im zwei-dimensionalen Modell enthalten Diffusion, Reaktion, Bindung und Membrantransport von Kalziumionen in einer Zelle.

Wir beweisen globale Existenz von starken Lösungen für dieses System unter Verwendung von Halbgruppentheorie und der Methode der invarianten Gebiete. Unsere Ergebnisse geben eine mathematische Begründung zu dem weit verbreiteten Einsatz von Computersimulationen für dieses und andere damit zusammenhängende Modelle.

Die eigentliche Herausforderung der Berechnungen für die Kalziumdynamik ist, dass die Quellterme in den Modellgleichungen das Problem sehr steif machen. Die Kanäle öffnen und schlieÃen sich auf einer sehr kurzen Zeitskala, und sie sind im Raum stark lokalisiert, während es intermittierende Zeiträume und räumliche Bereiche mit geringer Ãnderung in der Aktivität gibt.

Wir stellen hochauflösende numerische Lösungen in Raum und Zeit für dieses Kalziumdynamik-Modell dar. Wir betrachten das Modell unter Verwendung von diskontinuierlichen Galerkin (DG)-Verfahren, die aufgrund der folgenden Eigenschaften interessant sind: ihre formale Genauigkeit hoher Ordnung, ihre nichtlineare Stabilität, ihre hohe Parallelisierbarkeit, ihre Fähigkeit, mit komplizierten Geometrien umzugehen, und ihre Fähigkeit, die Unstetigkeiten oder starken Gradienten der Lösung zu handhaben ohne Störschwingungen zu erzeugen. Unsere numerische Implementierung basiert auf dem Software-Paket DUNE, das eine in C++ geschriebene Open-Source-Software ist.

Die numerischen Ergebnisse werden für mehrere Methoden höherer Ordnung im Raum präsentiert. Dies umfasst die DG-Methode der Weighted-Interior-Penalties (WIP) im Raum und die adaptiven und linear-impliziten Runge-Kutta-Verfahren höherer Ordnung vom Rosenbrock-Typ für die Zeitintegration. Die WIP-Methode, die wir anwenden, ist robuster im Umgang mit heterogener Diffusion, bei der die Diffusionskoeffizienten lokal kleine Werte annehmen und dies zu reaktions-dominierten Bereichen führt, was auch den Modellgleichungen entspricht. Es wird eine Hybrid-Methode angewendet, die die Lösung des deterministischen und des stochastischen Teils des Modells koppelt. Durch das Erzeugen eines adaptiven Gitters a priori und das automatische Anpassen der Zeitschritte an die richtigen Skalen während des Ãbergangs von Kanalzuständen, wurden die Entwicklung von Kalziumionen und Pufferkonzentrationen genau aufgelöst.

Um die Recheneffizienz zu gewährleisten, werden die deterministischen und Hybrid-Modelle unter Verwendung von parallelen numerischen Methoden auf Basis von Gebietszerlegungsalgorithmen implementiert. Unsere Ergebnisse aus der parallelen Version der Simulation demonstrieren die effektive Parallelisierbarkeit der DG-Methoden, die zum Erreichen einer guten parallelen Effizienz führt.

Contents

Acknowledgements **i**

Abstract **iii**

Glossary **ix**

1 Introduction **1**
- 1.1 The subject of the thesis 1
- 1.2 Layout of the thesis 5

2 Modelling issues **7**
- 2.1 Introduction 7
- 2.2 Intracellular Calcium dynamics 10
- 2.3 Governing equations 12
- 2.4 Stochastic behavior of intracellular Ca^{2+} dynamics 14
- 2.5 Hybrid stochastic and deterministic model 17

3 Global existence of strong solutions **20**
- 3.1 Introduction 20
- 3.2 The structure conditions (**P**) and (**M**) 23
- 3.3 Existence of local strong solutions 27
  - 3.3.1 Elliptic boundary value problems and semigroups in $L^p(\Omega)$ . . 30
  - 3.3.2 Semigroup formulation for the system 32
- 3.4 Invariant regions and global existence 40

4 Discretization **43**
- 4.1 Aims and Outline 43
- 4.2 Background 43
- 4.3 A brief historical perspective of DG methods 45
- 4.4 Numerical methods 47
  - 4.4.1 Mathematical notations and function spaces 47
  - 4.4.2 The basic aspects of the DG method 50

4.4.3 Model Problem 53
4.4.4 Choice of basis functions 59
4.4.5 Symmetric Weighted Interior Penalty (SWIP)method 60
4.4.6 Matrix assembly 64
4.5 Time discretization 67
4.6 Solution of algebraic equations 70
4.6.1 Inexact Newton method 71
4.6.2 Solution of linear equations 72
4.7 Parallel implementation 73

5 Numerical results **75**
5.1 Introduction 75
5.2 Numerical tests on a scalar problem 76
5.3 Numerical tests on a 2 × 2 system 81
5.4 Generation of initial unstructured grids 84
5.5 Numerical tests for the deterministic model 86
5.5.1 Opening and closing results 86
5.5.2 DG vs FEM solutions 91
5.5.3 Parallel efficiency test 94
5.6 Numerical results for the hybrid model 97
5.6.1 Numerical results with one cluster set up 97
5.6.2 Numerical results for multi cluster set up 98

6 Summary and future work **105**

Appendices **106**

A Standard definitions and theorems **107**

B Hybrid algorithm and simulation parameters **112**

Bibliography **115**

Curriculum Vitae **128**

Glossary

Apoptosis - The process of programmed cell death that may occur in multicellular organisms.

Astrocytes - are characteristic star-shaped glial cells in the brain and spinal cord that are widely regarded as cells that propagate intercellular Ca^{2+} waves over long distances in response to stimulation.

ATP - A ribonnucleoside 5-triphosphate functioning as a phosphate group donor in the cell energy cycle; carries chemical energy between metabolic pathways by serving as a shared intermediate coupling endergonic and exergonic reactions.

Buffer - Usually any substance which binds protons. Used here for binding most of the Ca^{2+} in a cell.

Cell signaling - Part of a complex system of communication that governs basic cellular activities and coordinates cell actions.

Cytoplasm - The portion of a cell's contents outside the nucleus but within the plasma membrane; includes organelles.

Cytosol - The continuous aqueous phase of the cytoplasm, with its dissolved solutes; excludes the organelles.

Dissociation constant - An equilibrium constant (K_d) for the dissociation of a complex of two or more biomolecules into its components; e.g., dissociation of a subtrate from an enzyme.

Endoplasmic Reticulum - An extensive system of double membranes in the cytoplasm of eukaryotic cells; it encloses secretory channels and is often studded with ribosomes (rough endoplasmic reticulum).

Glial cells - non-neuronal cells that provide support and nutrition, maintain homeostasis, and participate in signal transmission in the nervous system.

IP_3 receptor - also called inositol 1, 4, 5-triphosphate, is a secondary messenger molecule used in signal transduction and lipid signaling in biological cells.

M (molar) - Unit of solute concentration corresponding to 1 mole solute per liter of solution.

Oocytes - Cells from which an egg or ovum develops by meiosis.

Receptor - Protein that binds a specific signaling molecule (ligand) and initiates a response. Intracellular receptors bind ligands that diffuse into or inside the cell.

Sarcoplasmic Reticulum - Network of internal membranes in the cytoplasm of a muscle cell that contains high concentrations of sequestered Ca^{2+} that is released into the cytosol during muscle contraction.

SERCA pumps ($\underline{S}$arco - and $\underline{E}$ndoplasmic $\underline{R}$eticulum $\underline{C}$alcium $\underline{A}$TPases): Ca^{2+} pumps located in the membrane of the sarcoplasmic and endoplasmic reticulum whose function is to accumulate Ca^{2+} into these organelles, using ATP as the energy source.

Chapter 1

Introduction

1.1 The subject of the thesis

This thesis is dedicated to the analytical and numerical study of a semilinear reaction-diffusion system describing intracellular calcium dynamics. Calcium is an important intracellular signalling molecule with rapid effects on the kinetics of many processes. The immediate consequence of this has warranted almost all biophysically realistic models of cells to account for Ca^{2+} dynamics in some sense. The type of mathematical model equations depicting most Ca^{2+} dynamics models are highly complex and constructing their exact analytical solutions is still a mirage. Therefore, to gain an insight into the solutions of these systems, numerical methods are indispensable to obtain the approximate solutions. Moreover, these equations exhibit intense coupling and it is a momentous task to secure numerical solutions within reasonable computational time. To remedy these high computational costs, parallel programming techniques are used to obtain efficient solutions. In this study, we have focused on the two-dimensional intracellular calcium model taken from Falcke [64]. These model equations in the cytosolic and endoplasmic regions represent a highly coupled semilinear parabolic system, and can be written in the following generalized way

$$\frac{\partial \mathbf{u}}{\partial t} = D\Delta \mathbf{u} + F(\mathbf{u}), \tag{1.1}$$

with suitable boundary and initial conditions. Here, $\mathbf{u} \in \mathbb{R}^n$ denotes the vector of concentrations of n-chemical species, D is the diffusion constant matrix and $F(\mathbf{u})$ describes the chemical reactions. The model considered in this research has a linear diffusion part (with constant diffusion matrix) and a discontinuous nonlinear reaction part, see equation (3.2).

In the cell, the principle intracellular Ca^{2+} store is the endoplasmic reticulum (ER). Within the ER, Ca^{2+} is stored by low affinity high capacity Ca^{2+} binding proteins and is maintained at a free concentration between 0.1 and 1 mM relative to 0.1 μM cytosolic Ca^{2+}, see e.g., Roderick et al. [136]. According to [136], this concentration gradient is maintained by the action of Sarco-Endoplasmic Reticulum ATPases (SERCA) which hydrolyse ATP to pump Ca^{2+} into the ER. Following stimulation, Ca^{2+} is released from the ER through several classes of ligand gated channels. The most well characterized of these being the inositol 1,4,5-triphosphate receptor (IP_3R) and the Ryanodine receptor (RyR) families of proteins. This release of Ca^{2+} results in a drop of ER free Ca^{2+} to levels as low as 10 μM. This decrease in lumenal Ca^{2+} inhibits further release through the channels and increases the rate of re-sequestration of Ca^{2+} into the ER by SERCA pumps, see Roderick et al. [136].

In calcium dynamics, a salient responsibility of the cellular information processes is calcium signalling. Distinct signals can trigger a sudden increase in the cytosolic calcium level by opening channels in the ER. The calcium released by one channel diffuses into the cytosol. This diffusivity raises the opening probability of neighboring channels, leading to the spatial spread of release. The opening and closing of channels transpire in the order of microseconds. The ensuing procedure leads to complicated spatio-temporal signals in the cell. Due to the fluctuations in binding and unbinding of IP_3 and Ca^{2+}, the opening and closing of channels is stochastic. Consequently, the most vital task is to fathom this complex signalling mechanism and to formulate accurate models that couple the stochastic channel transitions. Such type of stochastic models can be found in DeYoung and Keizer [52], Gillespie [69], Falcke [63], Thul and Falcke [154] among others. This thesis addresses the numerical treatment of such models using highly accurate and robust numerical methods. Precisely, the stochastic channel dynamics is linked to the deterministic model presented in Falcke [64] using a hybrid method proposed by Alphonsi et al. [4] and adopted by [140, 115].

The current issues for further research in intracellular calcium dynamics aim to move the modelling and simulation of Ca^{2+} much closer to experimental data. However, in an attempt to achieve this, certain challenges are encountered in the numerical simulations. For instance, due to the diverse length scales of channels and clusters in the membrane, suitable numerical methods are imperative. Admittedly, finite volume methods and finite element methods seem to be suitable. Specifically, the finite element method has been used for the numerical simulation of system (3.2), see e.g., [112, 140, 114, 115]. However, since computation of problems with discontinuous or sharp gradient solutions is not natural to continuous Galerkin (CG) methods, we consider the model using discontinuous Galerkin (DG) methods which are highly accurate methods in space and are well known to capture discontinuities in the computational domain. The DG methods are attractive because of the following features: their formal high-order accuracy, their nonlinear stability, their high parallelizability, their ability to handle complicated geometries and their ability to capture the discontinuities or strong gradients of the solution without producing spurious oscillations, see e.g., Cockburn [43]. In this work, the DG method we adopt is more robust in handling heterogenous diffusion, i.e., where the diffusion coefficients takes locally small values leading to reaction dominated regimes, which suits well the model equations (3.2). In order to encapsulate the original structure of the cell, we use adaptive grids obtained using an a priori error estimator. Precisely, a spatially exponential decay function is used to generate the fine meshes within the channel area.

The real challenge of the computations for calcium dynamics is that the source terms in the model equations (3.2) make the problem highly stiff. The channels open and close on a very short time scale and they are highly localized in space while there are intermittent time periods and spatial regions with slight change in activity. The time and space adaption interacts in a complicated way that is not yet fully understood, see e.g., Zeller et al. [161]. For realistic computations, the triggering of the calcium blips includes a stochastic method based on the Gillespie algorithm, see e.g., Rüdiger et al. [140]. The Gillespie method is based on the assumption that during successive stochastic events the propensities do not change. Notwithstanding, the concentration and propensities are changes based on the channel opening and closing. To cater for the inadequacy of the Gillespie method which assumes constant propensities, we use the hybrid method introduced by Alphonsi et al. [4]. This hybrid algorithm is adapted in our simulation in such away that the spatial-temporal equations are deterministic and the opening/closing of the channels are rendered as stochastic, see e.g., Rüdiger et al. [140] for the hybrid algorithm.

As already mentioned above, the time scale of calcium flux upon opening of a channel is of the order of microseconds. This time scale cannot be ignored since the binding of calcium to the channel can occur on time scales as short as tens of microseconds, see e.g., Rüdiger et al. [140]. However, simulations need to trace the evolution for many seconds in order to achieve statistically significant estimates of stochastic channel gating. The semi-discretized system therefore contains highly stiff ordinary differential equations and necessitates an efficient time-stepping method including time adaptivity for both the stochastic and deterministic equations of the model. We tackle this challenge by implementing the linearly implicit Runge-Kutta methods of Rosenbrock type [98] and a certain class of diagonally implicit Runge-Kutta (DIRK) methods [3] which are well known to handle nonlinear stiff problems. When all channels are closed, the time step is virtually in the order of milliseconds. To contend with such fast changing step sizes, an automatic time step procedure is befitting. This ensures that the step size is as large as possible while guaranteeing the desired precision.

Spatial and temporal adaptive methods are advantageous because they contribute to substantial saving in computational work for a given suitable tolerance. Most realistic large classes of problems in two and three space dimensions give rise to millions of unknowns in the computational domain. For sequential machines, such computations are tedious and may take several months to obtain a numerical solution. Particularly, solving the algebraic system expends much CPU time in computations. On this basis, parallel computing is essential. In spite of the use of modern parallel computers, the utter size of the ensuing system renders too much demand on the available capacity in terms of memory utilization and computational time. Since the practical simulation of the calcium model leads to millions of degrees of freedom, we utilize parallel computing with application of domain decomposition methods.

There has been a tremendous amount of work done in the recent years concerning the mathematical study of global existence for reaction-diffusion equations. This emanates from the fact that these systems characterize many mathematical models of phenomena studied in physics, chemistry, biology, population dynamics, etc. The construction of global solutions has been approached via invariant sets, differential inequalities, semigroup theory, and many other methods, see e.g., [7, 102, 138, 81, 5, 10, 108]. However, most of the research has been concentrated on the study of a single second order parabolic equation for one scalar-valued unknown, at least as far as nonlinear equations are concerned, and on particular systems for a vector-valued unknown describing specific physical situations.

Despite the well established theory for parabolic systems, especially using semigroups, the question of global existence for the calcium model (3.2) poses a great challenge due to the discontinuities in the source terms. This thesis also aspires to establish the existence of global strong solutions to system (3.2) via semigroup theory. The basic idea of this method is to interpret the partial differential equation as an ordinary differential equation in an appropriate Banach space. This assigns a predominant role to the time variable and relegates the spatial dependence to the correct choice of the underlying function spaces and to the properties of the operators representing the partial differential equations, see e.g., Amann [7]. For instance, a scalar reaction-diffusion equation has the form

$$\partial_t u - d\Delta u = f(t,u), \quad \text{on } \;]0,\infty[\, \times \Omega, \tag{1.2}$$

with suitable initial data and various boundary conditions. In the semigroups approach for the case of homogeneous boundary conditions, one interprets (1.2) as an abstract evolution equation in a Banach space X (usually an L^p-space) of the form

$$\dot{u} + Au = f(t,u), \quad t > 0, \qquad u(0) = u_0,$$

where A is an unbounded linear operator whose domain consists of those functions (in an appropriate Sobolev space) satisfying the homogeneous boundary conditions. Then $-A$ is the infinitesimal generator of an analytic semigroup $S(t) := e^{-tA}$, $t \geq 0$, and problem (1.2) is essentially equivalent to the integral equation

$$u(t) = S(t)u_0 + \int_0^t S(t-s) f(s,u(s))\, ds, \qquad t \geq 0. \tag{1.3}$$

This integral equation, which is a consequence of the "variations-of-constants formula", is the basis for the proof of local and global existence theorems and for the study of asymptotic behavior of the solutions, that is, for the study of stability questions, see e.g., Amann [7]. Since the semigroup operator $S(t)$ acts componentwise in the variations-of-constants formula, we extend this abstract theory to the calcium system (3.2). We mollify the discontinuities in the source terms using the standard mollifier described in Evans [62, C. 4].

The following are the main achievements of the thesis:

1. The discontinuous nonlinearities in the model make it unfeasible to apply the existing theory for reaction-diffusion systems using semigroups. Mollifying the discontinuities in the source terms and using an appropriate limiting procedure has resulted in the construction of local strong solutions. Thereafter, invariant regions containing the solutions have been determined leading to a priori L^∞-bounds that imply global existence. This is a new result for this calcium model.

2. The first higher order DG implementation for the model in Falcke [64] is presented. The original structure of the cell has been encapsulated by developing a novel method for randomly generating multiclusters and multichannels within the channel area. By generating the adaptive grids a priori and automatically adapting the time steps to the proper scales during the transition of channel states, the evolution of calcium ions and buffer concentrations have been resolved accurately.

3. A good scalable parallel implementation for this model on highly unstructured grids has been achieved both for the deterministic and hybrid models. The benchmarks performed for upto 64 cores have revealed good parallel efficiency. In contrast to the earlier parallel implementation of this model using the continuous Galerkin (CG) method, the discontinuous Galerkin (D)G method has exhibited strong scalability.

1.2 Layout of the thesis

The majority of the subsequent chapters begin with a preamble to motivate the work of the chapter in addition to a literature review related to the work. The contents of each chapter in the remainder of this thesis is set out as follows:

In Chapter 2 we set the scene for our study, introducing the model equations in intracellular calcium dynamics. We primarily first recap the known results on modelling issues in calcium dynamics. The deterministic equations in 2D presented in Falcke [64] are recalled together with the stochastic channel model based on the DeYoung-Keizer (DYK) model for the subunit dynamics, DeYoung and Keizer [52]. We conclude the Chapter by giving a synopsis of the hybrid stochastic and deterministic model used in the realistic computations.

In Chapter 3, we present global existence results for strong solutions for the calcium system (3.2). The key analytical tools we employ are the basic existence theory for abstract semilinear differential equations [123, 7, 102, 138, 81] and the invariant region approach of Smoller [147]. These results are novel for this model and they hold even with initial data chosen in $L^\infty(\Omega)$, which is a bigger space than the domain $D(A)$ of the elliptic operator.

In Chapter 4, we present the numerical methods which we employ to obtain the approximate numerical solutions. Our methods encompass the discontinuous Galerkin (DG) method in space and semi-impicit methods in time. We begin this chapter by giving a brief background and historical perspective of the DG methods. The basic mathematical notations and appropriate function spaces are highlighted in this chapter. Here, we also recall the basic aspects of DG method for elliptic problems presented in Di Pietro and Ern [129] together with statements on its coercivity, boundedness and convergence rates in appropriate norms. We conclude the Chapter by presenting a synopsis of the time discretization methods, solution methods for the algebraic system and domain decomposition methods used in the parallel computations.

Chapter 5 contains the results of a series of computer experiments to approximate solutions for the calcium model. We first conduct numerical experiments on a scalar problem to check the stability, accuracy and convergence of the DG method. We then verify our DG code for systems by implementing a classical 2×2 reaction-diffusion system. Thereafter, we give an overview of how we generate the highly unstructured simplicial grids used for the spatial resolution of the computational domain. By considering different grid levels, we present the numerical convergence of solutions when a channel is opened and closed deterministically. We also present parallel efficiency results for the deterministic multi-cluster simulations and make some comparisons with the finite element method. We conclude this chapter by exhibiting numerical results for the hybrid model both sequentially and in parallel. Our results depict both the improvements in accuracy and the dramatic increases in parallel efficiency that arise when DG methods are used.

Finally, in Chapter 6, we briefly summarise our work and make some conclusions. These include the results of all the previous chapters. We also indicate possible directions for future research. The Appendix contains some standard definitions and theorems cited in Chapter 3, together with simulation parameters and the algorithm used for implementing the stochastic simulations.

Chapter 2

Modelling issues

In this chapter we introduce the model equations in intracellular calcium dynamics which take the form of reaction-duffusion systems. To this end, we first review pertinent literature pertaining to intracellular Ca^{2+} modelling. Primarily, we recapitulate the salient points regarding Ca^{2+} modelling. The majority of the results in this chapter are already known and we state them to aid the completeness of our work.

2.1 Introduction

Calcium is critically important for a vast array of cellular functions, as can be seen by a quick look through any physiology publication. For example, Sneyd and Keener [148, Ch. 7] discuss the role that Ca^{2+} plays in muscle mechanics, cardiac electrophysiology, bursting oscillations and secretion, hair cells, and adaptation in photoreceptors, synaptic plasticity, among other things. Clearly, the mechanisms by which a cell controls its Ca^{2+} concentration are of central interest in cell physiology. There are a number of Ca^{2+} control mechanisms operating on different levels, all designed to ensure that Ca^{2+} is present in sufficient quantities to perform its necessary functions, but not in too great quantity in the wrong places. For example, cellular Ca^{2+} overload can trigger apoptotic cell death, a process in which the cell kills itself. In muscle cells, high intracellular Ca^{2+} is responsible for prolonged muscle tension and rigor mortis, see Sneyd and Keener [148, Ch. 7].

Berridge, Bootman and Lipp [29], open their review in Nature 1998 with: "Almost everything that we do is controlled by Ca^{2+} - how we move, how our hearts beat and how our brains process information and store memories". The above statement illustrates the universal significance of Ca^{2+} in cell signalling. The list may be continued thus: how eggs are activated upon fertilization, how acinar cells secrete, how wounds heal, how ciliary beat frequency is coordinated, how liver cells coordinate their behaviour, how muscles contract and how cells die in apoptosis, [64].

Berridge, Bootman and Lipp called calcium a life and death signal because of its paramount importance for the control of all these processes.

To perform the above listed functions, Ca^{2+} acts as an intracellular messenger, relaying information within cells to regulate their activity. The Ca^{2+} signal employed by a variety of processes is a transient increase of the concentration in the cytosol, [27, 30, 130]. Increase of Ca^{2+} is due to entry through the cell membrane or to Ca^{2+} release from internal storage compartments, specifically the endoplasmic reticulum (ER) and the sarcoplasmic reticulum (SR). This increase in the cytosolic Ca^{2+} concentration may be organized as localized transients as in Parker [122], propagating waves [64, 107, 133] and global oscillations [26, 137].

As an additional control for the cytosolic Ca^{2+} concentration, Ca^{2+} is heavily buffered, i.e., bound by large proteins with estimates that at least 99% of the total cytosolic Ca^{2+} is bound to buffers, see e.g., Sneyd and Keener [148]. The Ca^{2+} in the ER is also heavily buffered. Ultimately, the information transmitted by these signals arrives as a stimulus at the plasma membrane and is translated into intracellular Ca^{2+} oscillations by well known pathways. If cells are connected, such intracellular waves can spread into neighbouring cells and become intercellular waves to coordinate cellular responses within a tissue. Propagation of a wave allows to transmit local information to a global level as for example upon sperm fusion in oocytes and intercellular signalling in the central nervous system by waves in astrocytes, [78, 116].

The versatility of the use of Ca^{2+} arises from its function as an intracellular messenger. Ca^{2+} relays information arriving at the cell surface to intracellular targets or coordinates groups of cells by intercellular communication, [26]. Ca^{2+} dynamics has obtained large attention in biological research as the number of large publications in high ranking journals illustrate. However, there is still enormous potential in using it as a tool to understand non-equilibrium dynamics and pattern formation. Most of the theoretical research has focused on deterministic models of intracellular Ca^{2+} waves [55, 149, 158, 159]. Only recently, the stochastic nature of intracellular Ca^{2+} release was considered [63, 65, 146].

Ca^{2+} dynamics in living cells has been a major topic of biophysical modelling in the last 15 years with modelling reaching the level of predictive power. The theoretical analysis of waves provided new insight into the mechanisms of Ca^{2+} signalling and led to new concepts of analysis of wave equations with concentration dependent diffusion and novel wave bifurcations. Modelling of oscillations (especially complex oscillations) has provided understanding and allowed for the extraction of information about the underlying cellular parameters and mechanisms, see Falcke [64]. In [64], the author has presented an elaborate review focusing on modelling and theoretical analysis of Ca^{2+} dynamics involving the IP_3 receptor channel. This review has included experimental results on the IP_3 receptor channel, the endoplasmic reticulum, SERCA pumps and mitochondria as the most important elements of intracellular Ca^{2+} handling. The experimental results on oscillations, intracellular waves, intercellular waves and elemental events are provided in conjunction with the corresponding theories in this review.

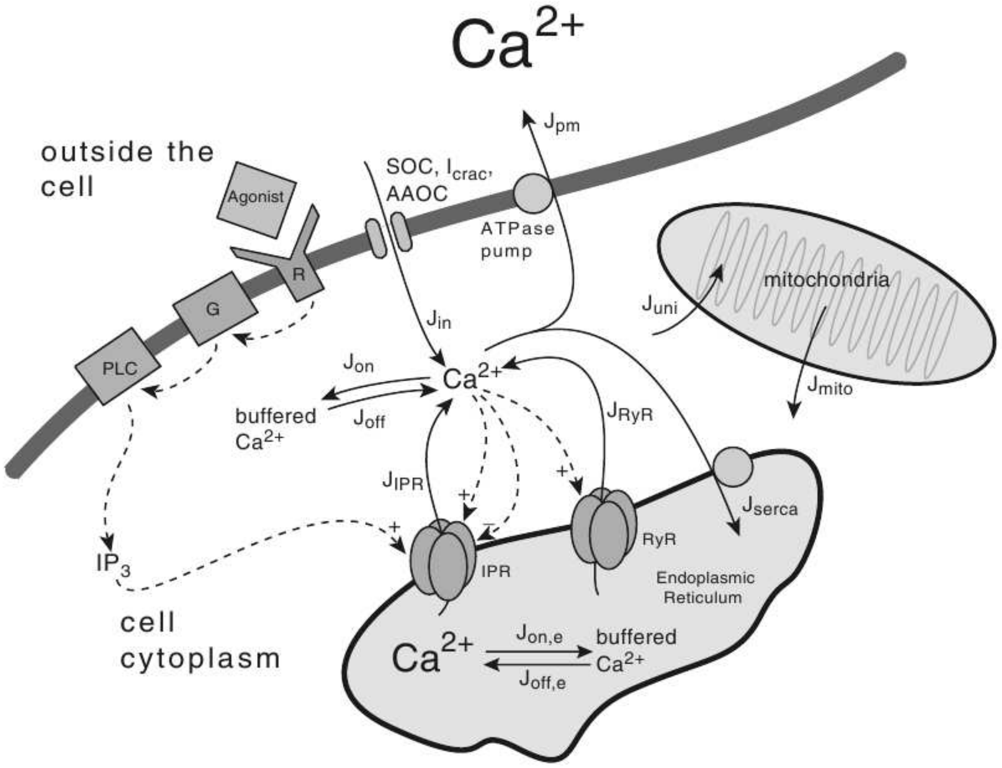
Ca^{2+}
J_{pm}
outside the cell
SOC, I_{crac}, AAOC
Agonist
R
G
PLC
ATPase pump
mitochondria
J_{uni}
J_{mito}
J_{in}
J_{on}
Ca^{2+}
buffered Ca^{2+}
J_{off}
J_{RyR}
J_{IPR}
+
+
+
+
−
J_{serca}
RyR
IPR
Endoplasmic Reticulum
IP_3
cell cytoplasm
Ca^{2+}
$J_{on,e}$
buffered Ca^{2+}
$J_{off,e}$

Figure 2.1: Fluxes controlling cytoplasmic Ca^{2+} concentration: Figure from Sneyd and Keener [148, pp. 275].

We have mentioned a wealth of theoretical and modelling work which have been inspired by intracellular Ca^{2+} dynamics. These have provided an understanding of mechanisms which can generate oscillatory behaviour and allow for wave propagation inside cells. Simplified models have set up frames for understanding of complex behaviour in complicated settings. Detailed models, their analysis and simulations have provided insight into the processes in specific cells or allowed to obtain parameter values. The dual approach of simplified and detailed modelling will remain crucial for further success of this field. There are two recent developments which should be combined in order to move modelling of Ca^{2+} dynamics closer to theoretical experiments. These are the sophisticated methods of fitting models to experimental data developed mainly by Sneyd et al., [150] and stochastic approaches to intracellular Ca^{2+} dynamics using spatially discrete channel cluster distributions.

This research has attempted to present a combination of these methods that improves agreement between model results and experimental observations. In Figure 2.1 we give a summary of the major fluxes involved in the control of cytoplasmic Ca^{2+} concentration.

We give a clarification of Figure 2.1 as follows: Binding of agonist to a cell membrane receptor (R) leads to the activation of a G-protein (G), and subsequent activation of phospholipase C (PLC). This cleaves phosphotidylinositol bisphosphate into diacylglycerol and inositol trisphosphate (IP_3), which is free to diffuse through the cell cytoplasm. When IP_3 binds to an IP_3 receptor (IPR) on the endoplasmic reticulum (ER) membrane it causes the release of Ca^{2+} from the ER, and this Ca^{2+} in turn modulates the open probability of the IPR and ryanodine receptors (RyR). Calcium fluxes are denoted by solid arrows. Calcium can be released from the ER through IPR (JIPR) or RyR (J_{RyR}), can be pumped from the cytoplasm into the ER (J_{serca}) or to the outside (J_{pm}), can be taken up into (J_{uni}), or released from (J_{mito}), the mitochondria, and can be bound to (J_{on}), or released from (J_{off}), Ca^{2+} buffers. Entry from the outside (J_{in}) is controlled by a variety of possible channels, including store-operated channels (SOC), Ca^{2+}-release-activated channels (I_{crac}), and arachidonic-acid-operated channels (AAOC).

2.2 Intracellular Calcium dynamics

Intracellular Ca^{2+} dynamics is the dynamics of Ca^{2+} transport through the plasma membrane, release from and uptake by intracellular stores and binding to buffer proteins. Release is determined by the conduction properties of the release channels and the diffusion characteristics of the storage compartments and the receiving compartments. Opening and closing of Ca^{2+} channels control the release. These channels are packed into clusters on the membrane of intracellular storage compartments like the endoplasmic reticulum (ER) or the sarcoplasmic reticulum (SR) containing 10-50 channels, see Figure 2.2. The maximal number of channels in a cluster is not very well known but it is estimated to be in the range of 20-30, see [36, 56]. These clusters in turn are randomly scattered across the ER membrane. The average distance of clusters is typically larger than the Ca^{2+} diffusion length, see [107, 153]. Stochastic behavior, i.e., random opening and closing of channels, manifests itself as spontaneous release events through single channels or several channels in a cluster, see [32, 107].

A channel type, which control the release of Ca^{2+} , present in the ER membrane of many cells is the inositol 1,4,5-trisphosphate (IP_3) receptor channel (IP_3R). The opening probability of the IP_3 depends on the Ca^{2+} on the cytosolic side of the channel and the IP_3 concentration, see [130, 152] for reviews. It increases nonlinearly with the IP_3 concentration and the Ca^{2+} concentration. Thus, Ca^{2+} released by one

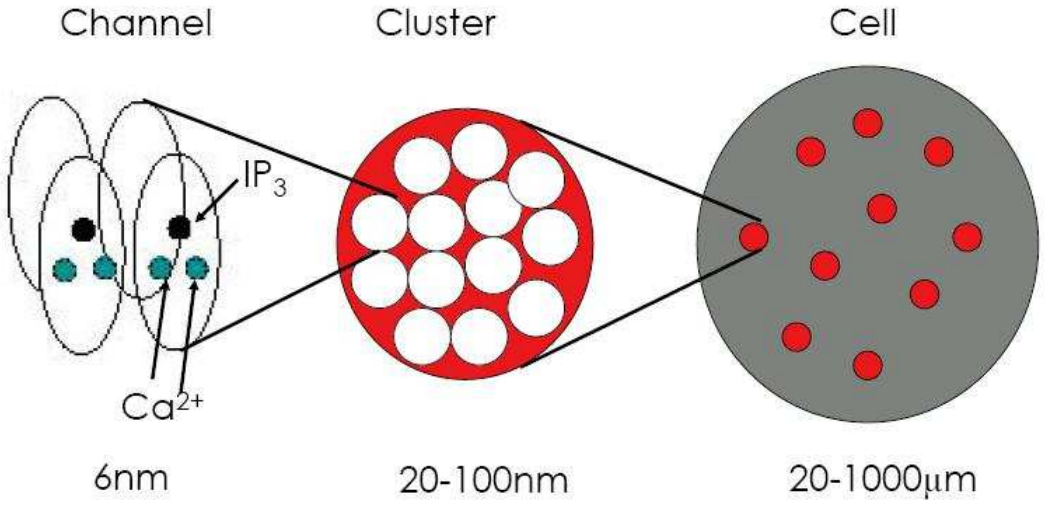

Figure 2.2: The structure of clusters and channels.

channel diffuses in the cytosol and thus increases the opening probability of neighboring channels. This provides a self-amplifying release mechanism and the coupling of channels by Ca^{2+} diffusion causes the spatial spread of release, which is called Calcium Induced Calcium Release (CICR). The IP_3R channel releases Ca^{2+} from the endoplasmic reticulum (ER) upon an increase of IP_3 concentration in the cytosol, see Figure 2.3. Further, a remarkable feature of the conductive channel property is the strong nonlinearity of the Ca^{2+} feedback. For large Ca^{2+} concentrations, which occur in the vicinity of an open channel, Ca^{2+} inhibits its own release.

Another element of intracellular Ca^{2+} handling are buffers. Buffers are proteins binding most of the Ca^{2+} in a cell (up to 99%). They are present in the cytosol as well as in ER and other storage compartments. Buffers are considered as mobile or immobile depending on their diffusion characteristics. The rate constants of Ca^{2+} binding and dissociation allow for a distinction between slow and fast buffers. Buffering of most of the free Ca^{2+} is one of the basic phenomena in intracellular Ca^{2+} dynamics. It influences the time scales and sets the diffusion length scales.

The dependence of the opening probability of the release channels on cytosolic Ca^{2+} creates communication between channels and allows for the formation of spatio-temporal patterns of intracellular Ca^{2+} release. These patterns show a hierarchy of the phenomena. The elementary event of cytosolic Ca^{2+} dynamics is the opening of a single channel with the ensuing Ca^{2+} release called a *blip*. The next larger event is a *puff* and a puff is the opening of several closely packed channels. Puffs are generic elements of Ca^{2+} signalling, see [28, 155]. They can cooperate to set off a wave traveling through the cell.

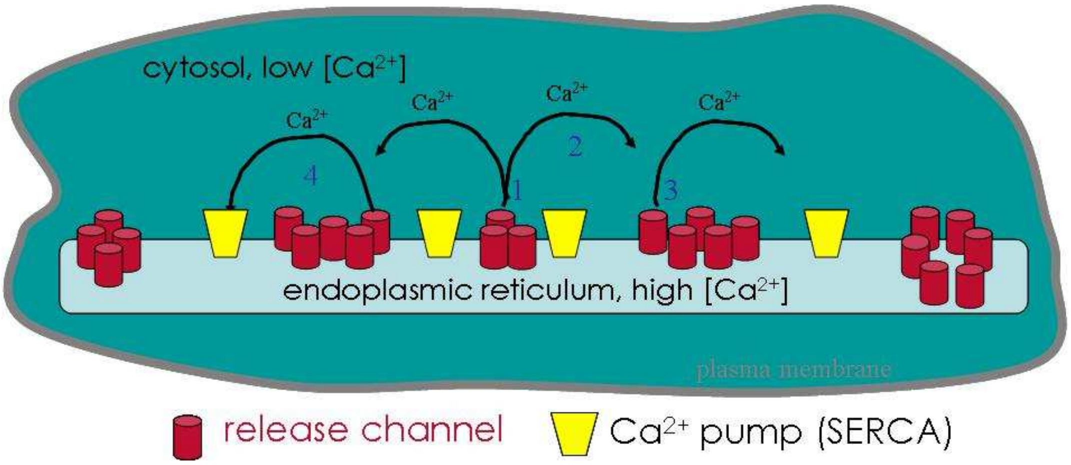

Figure 2.3: The structure of clusters and channels.

2.3 Governing equations

In a cell, the Ca^{2+} is transported through channels and by pumps, diffuses in the cytosol as well as in the endoplasmic reticulum and reacts with buffers. A stationary profile can be reached by assuming the removal of Ca^{2+} from the cytosol by pumps, or imposing boundary conditions which guarantee that the current entering through the channel is equal to the current leaving through the volume surface. The release process is described by the reaction-diffusion equations for the cytosolic Ca^{2+} concentration c and the Ca^{2+} concentration E in the ER as well as the buffer concentrations b_i and $b_{E,j}$, in the cytosol and and ER respectively. We have $i = s, d, m$ and $j = s, m$, where s denotes a stationary, d a dye and m a mobile buffers. These equations are in Cartesian coordinates. It is a spatially two-dimensional model, consequently we consider thin sheets below and above an idealized planar ER membrane of finite dimension. All concentrations are therefore two-dimensional in space, see Falcke [64].

The equations include diffusion of free Ca^{2+} described by $D\Delta c$, diffusion of dye buffers b_d denoted by $D_d\Delta b_d$, diffusion of mobile buffers b_m described by $D_m\Delta b_m$ and the reactions of stationary buffer b_s, dye buffer b_d and mobile buffer b_m with free Ca^{2+} given by $k_i^+(B_i - b_i)c - k_i^- b_i$ where $i = s, d, m$. The total concentration of stationary, dye and mobile buffer $B_i, i = s, d, m$ is usually homogenous before the experiments begin. Therefore, the concentration of free buffer, i.e., buffer with no Ca^{2+} bound can be expressed as $(B_i - b_i)$ at any point in space. The deterministic reaction-diffusion equations in two space dimensions are

$$\frac{\partial c}{\partial t} = \overbrace{D_c \Delta c}^{\text{diffusion}} + \overbrace{(P_l + P_c(\mathbf{x}))(E-c)}^{\text{leak+channel}} - \overbrace{P_p \frac{c^2}{K_d^2 + c^2}}^{\text{pumping}} - \overbrace{\sum_i H_i(c, b_i)}^{\text{buffering}}, \tag{2.1}$$

$$\frac{\partial E}{\partial t} = D_E \Delta E - \gamma \left[(P_l + P_c(\mathbf{x}))(E-c) - P_p \frac{c^2}{K_d^2 + c^2} \right] - \sum_j K_j(E, b_{E,j}), \tag{2.2}$$

$$\frac{\partial b_i}{\partial t} = D_{b,i} \Delta b_i + k_{b,i}^{+}(B_i - b_i)c - k_{b,i}^{-} b_i, \quad i = s, m, d, \tag{2.3}$$

$$\frac{\partial b_{E,j}}{\partial t} = D_{E,j} \Delta b_{E,j} + k_{E,j}^{+}(G_j - b_{E,j})E - k_{E,j}^{-} b_{E,j}), \quad j = s, m. \tag{2.4}$$

In Equation (2.1), the second and third terms model the Ca^{2+} flux through the membrane of the ER. The quantity P_l is the coefficient for a leak flux proportional to the concentration difference $E - c$. The function P_c describes the location and opening state of channel clusters. It depends on the concentration difference $E - c$. The function P_c has a constant positive value P_{ch} at the location of a channel, if channels in the cluster are open, and vanishes outside a channel. Thul and Falcke [154] have proposed a model to determine the cluster radius as follows

$$R_i = R_s \sqrt{N_{open,i}} \quad ,$$

where R_s is the channel radius and $N_{open,i}$ denotes the number of open channels. Clusters are situated at fixed positions $\mathbf{x}_i$. The flux term is then described as follows:

$$P_c(\mathbf{x}, t) = \begin{cases} P_{ch} & \text{if} \quad \|\mathbf{x} - \mathbf{x}_i\| < R_i \quad \text{for a channel } i \text{ with radius } R_s, \\ 0 & \text{otherwise.} \end{cases}$$

Note that in a model including the dynamics of channel gating the number of open channels is time-dependent. Here, however we fix the values $N_{open,i}$ during a simulation. The corresponding value of P_{ch} can be found in Table B.1.

The fourth term in (2.1) models the action of pumps transporting Ca^{2+} from the cytosol into the ER while the last two terms describe the reaction of free Ca^{2+} with buffers. The equation for the dynamics of the lumenal concentration E i.e., (2.2) includes diffusion and the flux through the membrane. The flux terms also appear in the equation for cytosolic Ca^{2+}, only with opposite sign and scaled by the volume ratio γ.

Equations (2.3) and (2.4) describe the dynamics of the buffers with Ca^{2+} bound. The first term of the buffer dynamics in (2.3) and (2.4) is the buffer diffusion, the second term models binding free Ca^{2+} to free buffer while the last term is the rate of Ca^{2+} dissociation from the buffer. Immobile buffers are modeled by setting their diffusion coefficient to zero. All buffers are assumed to be distributed homogenously in the initial state. Total buffer concentrations in the cytosol and the ER are denoted by B_i and G_j, respectively. Experimentally, the total amount in some buffers is known quite well. However, the amount of some other buffers such as the stationary buffer, comprising contributions from different calcium stores such as mitochondria, is not well known. The buffer binding and unbinding of calcium is modeled by the usual mass-action kinetic terms

$$\begin{aligned} H_i(c, b_i) &= k_i^+(B_i - b_i)c - k_i^- b_i, \\ K_j(E, b_{E,j}) &= k_{E,j}^+(G_j - b_{E,j})E - k_{E,j}^- b_{E,j}. \end{aligned}$$

When a channel opens, Ca^{2+} concentration increases in the cytosol and decrease in the ER. A stationary state is reached when free Ca^{2+} has spread far enough so that removal of Ca^{2+} from the cytosol back into the ER balances the flux through the channel. The stationary profiles depend on buffer and cluster characteristics, see Falcke [64].

2.4 Stochastic behavior of intracellular Ca^{2+} dynamics

Ca^{2+} is released from the ER through channels. Channels are closely packed into clusters which are randomly distributed on the ER membrane, see Falcke et al. [65]. As we have already mentioned, this release process is nonlinear, since, as a general pattern, increased Ca^{2+} concentration in the cytosol favours opening of neighbouring channels. This autocatalytic amplification is called Calcium-Induced Calcium Release (CICR), see [65]. There are a variety of channels showing CICR. Here we focus on the inositol 1,4,5-triphosphate(IP_3) receptor channel(IP_3R). This channel consists of four identical subunits. Each subunit has an activating binding site for IP_3, an activating site for Ca^{2+} and an inhibiting Ca^{2+} binding site, see [65].

Experimental findings suggest that the channel is open if both Ca^{2+} and IP_3 are bound to the activating sites and at the same time Ca^{2+} is not bound to the inhibiting site, at at least three out of the four subunits. Binding of Ca^{2+} to the inhibiting site of one of these subunits closes the channel. It can reopen after dissociation of Ca^{2+} from the inhibiting sites, see [65]. The binding and dissociation of Ca^{2+} at the activating and inhibiting sites are stochastic events rendering the opening and closing of the channel a stochastic process. This stochastic process is coupled to the concentration of cytosolic Ca^{2+} because the binding probabilities per unit time depend on it, and vice versa. The number of open channels determines the concentration field. For a detailed theoretical analysis on how the stochasticity of the elemental events show up in global events, see Falcke [63].

Accordingly, the process causing random behavior in intracellular Ca^{2+} dynamics is the transition between the different states of the channel subunits and the channel. The opening and closing probability depends on the state of the channel subunits. The opening probability is the highest, if a minimum number of subunits are activated and very low otherwise. The findings of Mak et al. [105, 106] suggest that the change of opening probability is due to a change of the average opening rate whereas the closing rate is more or less constant. In the sequel, an event resulting in an opening or closing of the channel will be called channel transition. In this section, we give a brief introduction and description of a stochastic model for the gating of subunits. Since we have adopted the same procedure of the stochastic channel dynamics presented in Rüdiger et al. [140] for our numerical simulations, we follow closely the same approach of the model given in [140]. This model is based on the DeYoung-Keizer (DYK) model for the subunit dynamics, see DeYoung and Keizer [52]. It is known that a subunit consists of binding sites for Ca^{2+} and IP$_3$. However, the exact number of binding sites is still under investigation. Based on the results of Bezprozvanny et al. [31], DeYoung and Keizer [52] proposed a model for a single subunit. This model was set up as a deterministic model and used later on as a stochastic scheme by Falcke et al. [63, 65]. The subunit consists of three binding sites: an activating and an inhibitory Ca^{2+} as well as an activating IP$_3$ binding sites. Therefore the state of a subunit can be specified by a binary triplet ijk. The indices are represented by the IP$_3$ binding site, the Ca^{2+} activating and the Ca^{2+} inhibiting binding site respectively. An index is equal to 1 if an ion is bound and 0 if not. Hence, for example, the state 110 refers to IP$_3$ and Ca^{2+} bound to the activating sites, respectively, and no Ca^{2+} attached to the inhibiting binding site.

We assume that the channel is open, if at least three of the subunits are activated, i.e., they have bound Ca^{2+} and IP$_3$ at the activating site. The resulting eight states of a subunit are shown in Figure 2.4. In 2D numerical simulations, the standard DYK model is considered for a subunit dynamics which consists of 8 different states, i.e., see Figure 2.4. In Figure 2.4, the binding rate constants for IP$_3$ activation are given by a_1p and a_3p, whereas a_2c and a_4c refer to Ca^{2+} inhibition. The activation of Ca^{2+} is controlled by a_5c. The dissociation rates for the above processes are denoted by b_1 through b_5. The reactions that occur at a subunit are binding and unbinding of Ca^{2+} and IP$_3$. They determine the state of one subunit. In an ensemble of subunits these processes lead to a fraction X_{ijk} of subunits in a state ijk. If the ensemble is large enough and homogeneous, these fractions can be described by rate equations. For instance, the time evolution of X_{110} is governed by

$$\dot{X}_{110} = -[b_5 + a_2c + b_1]X_{110} + a_5cX_{100} + b_2X_{111} + a_1pX_{010}, \tag{2.5}$$

with p being the IP$_3$ concentration and c the Ca^{2+} concentration. The negative term represents the processes that reduce the value of X_{110}. This can result from unbinding of IP$_3$ with rate b_1, unbinding from the activating Ca^{2+} site with rate b_5 and binding to the inhibiting Ca^{2+} binding site with rate a_2c. The remaining three terms control the increase of X_{110}. This happens for example through binding with rate a_5c to the activating Ca^{2+} site of a subunit that is in the state X_{100}. Similar equations can be derived for all the other states. Together with the remaining rate equations, the state of the ensemble is fully characterized. We associate stochastic variables $X_{000}, X_{001}, \ldots, X_{111}$ to each channel. These variables count the numbers of subunits which are in respective state.

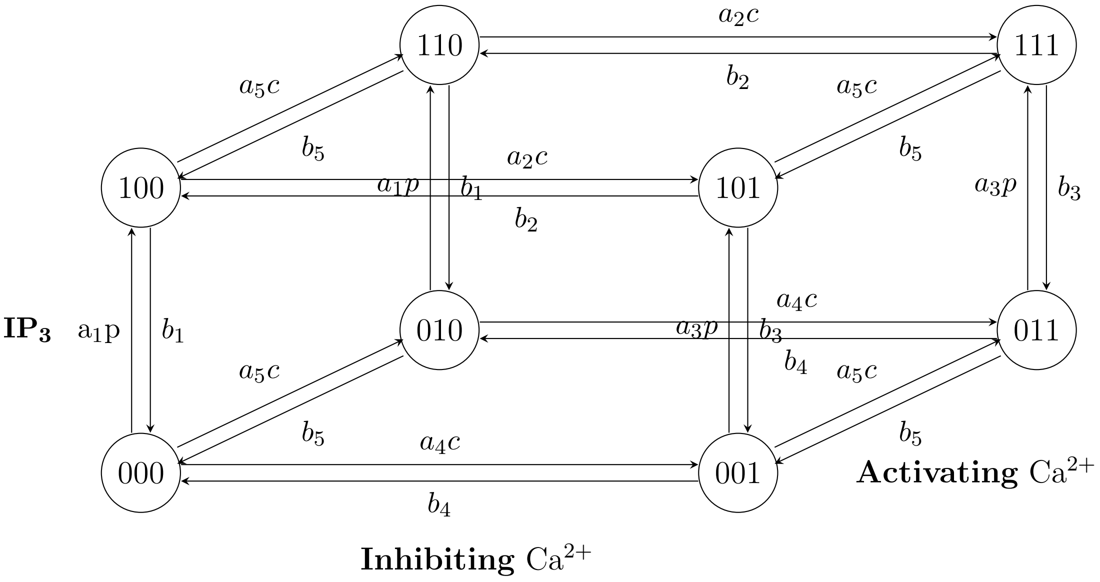

Figure 2.4: Transition scheme of a single unit of the DeYoung-Keizer model: Figure from DeYoung and Keizer [52].

In general, the Ca^{2+} concentration is not constant in time, so that a closed solution for the fractions X_{ijk} is not accessible. The binding and dissociation of Ca^{2+} and IP_3 as well as the conformational change are stochastic events rendering the opening and closing of the channel a stochastic process. That stochastic process is coupled to the concentration of cytosolic Ca^{2+} since the binding probabilities per unit time depend on it and vice versa. The number of open channels determines the concentration fields. The state of active elements can be described as either activated or deactivated. As their number per cluster is rather small and as they are tightly packed, each element occupies a non negligible spatial fraction. Therefore the state of a cluster is well characterized by the area occupied by activated units. We refer to it as the active area of a cluster. Usually this is not a connected patch. Its size equals the sum of the areas of all activated units.

In this thesis we use the stochastic solver based on the Gillespie method [69]. The main algorithm approach is that, given the actual time t, and stochastic events R_i, the probability that the next stochastic event occurs in the infinitesimal time interval $[t+\tau, t+\tau+dt]$ and is an R_i event is given by

$$P(\tau, i)\, dt = a_i \exp(-a_0\tau)dt, \tag{2.6}$$

where a_i is the propensity and $a_0 = \sum_j a_i$ is the sum of all propensities, see e.g., Rüdiger et al. [140]. The reaction propensities, a_i, are the probabilistic rates of the reactions. For more details on propensity functions, see Gillespie [68].

The probability density $P(\tau, i)$ can be realized by drawing two random numbers r_1 and r_2 from a uniform distribution in the interval $[0, 1]$ such that

$$a_0 \cdot \tau = \ln(1/r_1), \tag{2.7}$$

and

$$\sum_{j=1}^{i} a_j \leq a_0 \cdot r_2 < \sum_{j=1}^{i+1} a_j. \tag{2.8}$$

In this way we can find the next event R_i and it will occur after time τ.

2.5 Hybrid stochastic and deterministic model

The Gillespie method is based on the assumption that during successive stochastic events the propensities a_i do not change. Indeed, over those successive stochastic events, there must be a significant activity in all reaction channels. However, when linking the stochastic channel dynamics to the calcium dynamics, we expect the propensity a_i to change in time due to its dependence on the local calcium concentration c. This effect will be particularly strong for openings and closings of channels, since after such events the local calcium concentration c changes dramatically by orders of magnitude. So the propensities can change too rapidly over small time intervals. Moreover, purely stochastic simulations are computationally very expensive when there are many reactions involved in chemical systems. There are some efficient methods available in literature in this direction. However, this is still a buoyant area of research.

To cater for the inadequacy of the Gillespie method which assumes constant propensities, we adopt the hybrid method which was introduced by Alphonsi et al. [4]. In this hybrid algorithm, the calcium dynamics equations are partitioned into deterministic and stochastic equations in order to reduce the computational time and increase the efficiency. This hybrid algorithm is adapted in our simulation in such away that the spatial-temporal equations are deterministic and the opening/closing of the channels are considered as stochastic. Here we will give the brief description of the hybrid method. The reaction probability for each event R_i is specified in terms of the propensity function $a_i = a_i(t, c(t))$. Based on physical laws and the idea that chemical reactions are essentially random processes, the stochastic formulation of chemical reactions is given in terms of a Markov jump process $c(t) \in \mathbb{N}^N$, see Gillespie [70]. Its characterization is based on the probability $a_i(t, c)dt$ of event R_i occurring in the next infinitesimal time interval $[t, t + dt]$. Denoting by $T_i(t)$ the time at which event R_i first occurs after t, this can be written as

$$\mathbf{P}[T_j(t) \in [t, t + dt]|c(t)] = a_i(c(t), t)dt.$$

More details can be found in Alfonsi et al. [4]. Within their setting the time τ to the next stochastic event is determined by solving

$$g_i(t + \tau|t) = \int_t^{t+\tau} a_i(c(t), s)\, ds = \xi, \tag{2.9}$$

with $\xi = \ln(1/r_1)$, where the sum of propensities a_0 may explicitly depend both on time and the local calcium concentration. The function $g_i(t+\tau|t)$ is non-decreasing for $t + \tau > t$, since the propensities a_i are non-negative by definition. Note that the above equation simplifies to the equation determining τ in (2.7) in the case of constant a_0. To determine the time of next reaction τ, condition (2.9) is conveniently rewritten in differential form by introducing a variable $g(t)$ and solving

$$\dot{g}(s) = a_0(c, s), \tag{2.10}$$

with initial condition $g(0) = 0$, along with the deterministic equations for c and buffers. This is the stochastic equation considered in our numerical simulations. To calculate the propensities we follow the dynamics of DYK model. A reaction then occurs whenever $g(s)$ reaches the value ξ. As before, the specific event R_i is determined based on a second random number r_2 solving (2.8) with propensities evaluated at the event time $t + \tau$. This way one can determine the next reaction event and when it occurs.

We would like to give the brief outline of the algorithm here. A special feature of the calcium system is that not all stochastic events change the open/close state of a channel. A channel transition has a major impact on the local calcium concentration c, while nonchannel transitions do not change the local calcium concentration. During the computation of the deterministic part of the calcium dynamics the stochastic events are traced via (2.9) and (2.10) respectively. During the simulation the stochastic system is updated for every stochastic time step dt. The time step dt is determined using the first random number generation, see (2.7), and by fulfilling the requirement $a_0\, dt \leq 1$, where a_0 is the sum of the propensities. Using the second random number the reaction event R_i is determined using (2.8). In this way we can determine the next reaction event R_i and it will occur after the time τ . If a nonchannel transition occurs, the stochastic event is performed. The stochastic channel dynamics is updated correspondingly, while there is no influence on the calcium concentration. On the other hand, if a channel transition takes place, both the channel and the calcium dynamics do change. This typically requires a readjustment of the deterministic time step. The algorithmic realization of our hybrid approach is given in Appendix B.

Note that $\Delta t_{channel}$ should be smaller than or similar to the time scale of stochastic transitions after a channel opening/closing. This is needed since we linearly interpolate the deterministic solution to determine stochastic transitions between succeeding deterministic time steps. Therefore, fast changes of the deterministic variables after a channel opening/closing need to be approximated numerically at time scales comparable to the stochastic transitions. Here we typically use two time steps in the hybrid simulation. One time step is for updating the deterministic solution, which is determined by the adaptive time step criteria of an ODE solver and second time step is used for updating stochastic solver, which is calculated by the Gillespie algorithm. The step by step process of the hybrid algorithm can be found in Appendix B.

Chapter 3

Global existence of strong solutions

In this chapter we prove existence of global strong solutions to the two dimensional calcium system in Section 2.3. The key analytical tools we employ are the basic existence theory for abstract semilinear parabolic differential equations [123, 7, 102, 138, 81] and the invariant region approach of Smoller [147]. We establish that the unique local solution formulated via semigroups theory, is uniformly bounded for all time using invariant regions.

The outline of this Chapter goes as follows: In Section 3.1, we review pertinent literature on global existence results for relevant reaction-diffusion systems and then state our model problem precisely. In Section 3.2, we recall the definition of systems with (**P**)+(**M**) structure and show that our model fits into this family. In Section 3.3, we construct and prove the local existence of strong solutions, while the global existence of strong solutions is proved in Section 3.4. Finally, conclusions are given in the last Section. To help the reader, we have incorporated in Appendix A, some standard definitions and theorems cited in this chapter.

3.1 Introduction

In recent years, profound active research has been ongoing concerning global existence for solutions of reaction-diffusion systems of the form

$$\partial_t u_i - d_i \Delta u_i = f_i(u_1, \dots, u_m), \quad \text{on} \ \ ]0,\infty[\times \Omega, \quad i = 1, \dots, m, \tag{3.1}$$

with suitable initial data and various boundary conditions. The problem has been approached via a combination of invariant sets, differential inequalities, semigroup theory, and many other methods, see e.g., [5, 10, 108]. Particular interest has increased for models with applications in biology, ecology, environment and population dynamics. Two natural properties appear in most of these models: the nonnegativity of the solutions is preserved for all time (**P**); the total mass of the components is controlled for all time, sometimes even exactly preserved (**M**), see Pierre [126]. The model we consider on intracellular calcium dynamics, see Falcke [64], belongs to this family of systems.

Masuda [108], proved global existence for a specific 2×2 system with the above properties using a suitable Lyapunov function. He considered the case

$$f_1(u_1, u_2) \leq 0,\ f_2(u_1, u_2) \leq -\varphi(u_1) f_1(u_1, u_2),\ \ f_2(u_1, u_2) \leq \varphi(u_1)(u_2 + u_2^r),\ r \geq 1.$$

His results were extended by Haraux and Youkana [76], who could handle growth of type $e^{\alpha u_2^\beta}$ with $\alpha > 0$ and $\beta < 1$. The method in [76] could even reach an exponential growth, that is $\beta = 1$, but only with restrictions on the size of $\|u_{1_0}\|_\infty$, see Barabanova [15]. This approach was recently used by Benachour and Rebiai [25], to prove global existence for new specific systems in this family, and with possible quite higher growth, as in the case of

$$f_1(u_1, u_2) = -u_1^\alpha (1 + u_2^2) e^{u_2^2}, \quad f_2(u_1, u_2) = u_1^\alpha e^{u_2^2}.$$

Lyapunov functions have also been used to treat more elaborate polynomial systems with the so called *triangular* structure, see Kouachi [96]. We also mention the global existence results obtained in any dimension for systems with (**P**) and (**M**), and with strictly sub-quadratic growth, see e.g., [92, 93, 94, 37]. The quadratic case is also handled for some systems in dimension $N \leq 2$, see e.g., [72, 51, 83].

The development of the theory of ordinary differential equations with discontinuous right-hand sides has been to a great extent stimulated by its many applications. A large number of problems from mechanics, electrical engineering, and the theory of automatic control are described by these equations, see e.g., Filippov [66]. More results in this direction can be found in [50, 86, 79] and the references therein. Existence results of extremal mild solutions for ordinary differential equations with discontinuous right-hand sides in Banach spaces can be found in Heikkilä and Lakshmikantham [80]. They construct minimal and maximal mild solutions for differential equations with nondecreasing right-hand sides and extend the results to certain parabolic systems.

Here we study the 4×4 system which was developed by Falcke [64] and given by Equations (2.1)-(2.3). We recall this two dimensional calcium dynamics model, defined on the domain Ω, and write it as system of partial differential equations as follows

$$\begin{aligned}\frac{\partial c}{\partial t} =& D_c\Delta c + (P_l + P_c(\mathbf{x}))(E - c) - P_p\frac{c^2}{K_d^2 + c^2} - (k_{b,s}^+(B_s - b_s)c - k_{b,s}^-b_s)\\ &- (k_{b,m}^+(B_m - b_m)c - k_{b,m}^-b_m),\\ \frac{\partial E}{\partial t} =& D_E\Delta E - \gamma\left[(P_l + P_c(\mathbf{x}))(E - c) - P_p\frac{c^2}{K_d^2 + c^2}\right];\ \ 0 < \gamma < 1,\\ \frac{\partial b_m}{\partial t} =& D_{b,m}\Delta b_m + k_{b,m}^+(B_m - b_m)c - k_{b,m}^-b_m,\\ \frac{\partial b_s}{\partial t} =& D_{b,s}\Delta b_s + k_{b,s}^+(B_s - b_s)c - k_{b,s}^-b_s,\\ D_c\nabla c\cdot\mathbf{n} =& D_E\nabla E\cdot\mathbf{n} = D_{b,m}\nabla b_m\cdot\mathbf{n} = D_{b,s}\nabla b_s\cdot\mathbf{n} = 0 \text{ on } \partial\Omega\times[0,T],\\ c =& c_0,\ E = E_0,\ b_m = b_{m0} \text{ and } b_s = b_{s0} \quad\text{on}\quad \Omega\times\{t = 0\},\end{aligned} \tag{3.2}$$

where $\mathbf{n}$ is the unit outward normal to the boundary $\partial\Omega$ of Ω.

As depicted in Section 2.3, the function P_c describes the location and opening state of channel clusters. Channels are situated at fixed positions $\mathbf{x}_i$. We assume that our domain Ω contains a finite number $\ell \in \mathbb{N}$ of channels. For each channel there is a ball $\mathcal{B}(\mathbf{x}_i, R_i) = \{\mathbf{x} \in \mathbb{R}^2 \mid \|\mathbf{x} - \mathbf{x}_i\| < R_i\} \subset \Omega$ on which P_c takes the positive value P_{ch}. The balls do not overlap. Outside, the function P_c vanishes, i.e.,

$$P_c(\mathbf{x}, t) = P_c(\mathbf{x}) = \begin{cases} P_{ch} & \text{if } \ \|\mathbf{x} - \mathbf{x}_i\| < R_i \quad \text{for a channel } i \text{ with radius } R_i,\ i = 1\ldots\ell,\\ 0 & \text{elsewhere.}\end{cases} \tag{3.3}$$

Note that in practice, we want to spontaneously open and close channels. This is predominantly a stochastic process. However, in our analysis, we treat this channel transition as a deterministic process. Since opening and closing introduces a discontinuity in time of $P_c(\mathbf{x}, t)$, we assume for the sake of analysis that all channels are open initially and remain open, i.e., we consider the special case $P_c(\mathbf{x}, t) = P_c(\mathbf{x})$. For a detailed biophysical analysis of the model, see Falcke [64]. Numerical simulation results for system (3.2) will be presented in Chapter 5 but can also be found in Nagaiah [114, 115].

The fact that the total mass of the components, equivalent to the L^1-norm of the solution, does not blow up in finite time suggests that solutions should exist for all time. However, it turns out that the situation is not so simple. Some "good" situations do lead to global existence of classical solutions, while in others, "incomplete blow up" may occur, see Pierre [127]. For system (3.2), we establish using invariant regions that the local solution formulated via semigroups theory, is uniformly bounded for all time.

3.2 The structure conditions (P) and (M)

Throughout this chapter, it is assumed that Ω is a bounded domain in $\mathbb{R}^N$ (where $N=2$) with a smooth boundary $\partial\Omega$. Also, Δ is the Laplacian operator on Ω, and $\partial_n u = \frac{\partial u}{\partial n}$ denotes the outward normal derivative on $\partial\Omega$. The system in (3.2) can be precisely written as a general reaction-diffusion system as follows,

$$\left\{\begin{array}{lcl} \partial_t u_i - d_i \Delta u_i & = & f_i(u_1,\ldots,u_m) \quad \text{on }]t_0,T[\times\Omega,\ t_0\in\mathbb{R},\ T>t_0, \\ \partial_n u_i & = & 0 \qquad \text{on } [t_0,T]\times\partial\Omega, \\ u_i(t_0,.) & = & u_{i0}, \end{array}\right. \tag{3.4}$$

for all $i=1,\ldots,m,$ where the $f_i:\mathbb{R}^m\to\mathbb{R}$ are continuous functions of $\mathbf{u}=(u_1,\ldots,u_m)$, $d_i\in]0,\infty[$ and $u_{i0}\in L^\infty(\Omega)$. We introduce the domains $\Sigma_T=[t_0,T]\times\partial\Omega$ and $Q_T=[t_0,T]\times\Omega$. Note that our specific system (3.2) is such a system with $m=4$.

There are recent results and new tools for the mathematical analysis of systems like (3.4), satisfying the two main properties, see Pierre [126]:

(**P**) *Positivity of the solutions is preserved for all time.*

(**M**) *The total mass of the components is controlled for all time.*

According to [126], positivity (**P**) of the solutions for (3.4) is preserved if and only if $\mathbf{f}=(f_1,\ldots,f_m)$ is **quasi-positive** which means that, for all $i=1,\ldots,m$ and for all $\mathbf{r}=(r_1,\ldots,r_m)$

$$(\mathbf{P}) \qquad f_i(r_1,\ldots,r_{i-1},0,r_{i+1},\ldots,r_m)\geq 0. \tag{3.5}$$

This will be assumed for all nonlinearities throughout this chapter and shown for the system (3.2) at the end of this section. Condition (**M**) on the a priori bound of the total mass is satisfied for instance when for all $\mathbf{r}=(r_1,\ldots,r_m)\in[0,+\infty[^m$ we have the estimate

$$(\mathbf{M}) \qquad \sum_{1\leq i\leq m} f_i(\mathbf{r})\leq C[1+\sum_{1\leq i\leq m} r_i]. \tag{3.6}$$

With good boundary conditions on $\partial\Omega$ like for instance $u_i=0$ or $\partial_n u_i=0$, the inequality (3.6) implies that *the total mass of the solution is bounded on each finite time interval.* To see this, we set $w(t,x)=\sum_{1\leq i\leq m} u_i$ to be the "total mass", even though physically the u_i are concentrations. We integrate the sum of the m equations of (3.4) and use Gauss divergence formula as well as (3.6) to get

$$\partial_t\int_\Omega w(t,x)\,dx-\int_{\partial\Omega}\sum_i d_i\nabla u_i\cdot\mathbf{n}\,ds\leq C\int_\Omega[1+w(t,x)]\,dx.$$

Using the boundary conditions $\partial_n u_i = 0$ and nonnegativity of u_i, we obtain the Gronwall's inequality, see Evans [62, p. 624]

$$\partial_t \int_\Omega w(t,x) \leq C \int_\Omega [1 + w(t,x)],$$

i.e., we have

$$\begin{aligned}\int_\Omega w(t,x)\, dx \leq & e^{tC}\left[\int_\Omega w(0,x)\, dx + Ct\int_\Omega dx\right]\\ \leq & e^{TC}\left[\int_\Omega w(0,x)\, dx + CT\int_\Omega dx\right]. \end{aligned} \tag{3.7}$$

In other words, the total mass $\int_\Omega w(t,x)\, dx$ of the components is uniformly bounded on any finite interval. When the u_i are initially nonnegative, they remain nonnegative so that this implies

$$\sup_{t\in]0,T[} \|w(t,\cdot)\|_{L^1(\Omega)} < +\infty, \tag{3.8}$$

i.e., the $L^1(\Omega)$-norm of each component is uniformly bounded in time.

Instead of (**M**), we could assume that, for some given $a = (a_i)_{1\leq i\leq m}$ with for all i, $a_i > 0$ and for all $\mathbf{r} \in [0, +\infty[^m$,

$$(\mathbf{M}') \qquad \sum_{1\leq i\leq m} a_i f_i(r) \leq C[1 + \sum_{1\leq i\leq m} r_i]. \tag{3.9}$$

Obviously, ($\mathbf{M}'$) may be reduced to (**M**), after multiplying each i-th equation of (3.4) by a_i and upon replacing u_i by $a_i u_i$ and taking $a_i f_i$ for f_i.

For mathematical analysis in the next sections, it is necessary to rewrite system (3.2) in dimensionless form. The dimensions of the variables and parameters are given in Table 3.1. We introduce the characteristic length L and set $\tilde{x}_i = \frac{x_i}{L}$. Then the chain rule for the Laplacian Δ with respect to the x_i in the first equation of (3.2) gives

$$\Delta c(\tilde{x}_i, t) = \frac{1}{L^2}\Delta c(x_i, t),$$

where we use tildes to denote dimensionless dependent variables. The model (3.2)

Quantity	**Unit**
concentrations c, E, b_m, b_s, B_m, B_s	μM
leak flux coefficient P_l	s^{-1}
channel flux coefficient P_c	s^{-1}
single channel radius R_s	μm
pump flux coefficient P_p	$\mu\mathrm{M\ s}^{-1}$
pump dissociation coefficient K_d	μM
diffusion coefficients $D_c, D_E, D_{b,m}, D_{b,s}$	$\mu\mathrm{m}^2\ \mathrm{s}^{-1}$
on-rates of buffers: k_s^+, k_m^+	$(\mu\mathrm{M\ s})^{-1}$
dissociation constants of buffers : k_s^-, k_m^-	s^{-1}

Table 3.1: Dimensions of system (3.2). The units are: s seconds, $\mu\mathrm{M} = 10^{-6}\mathrm{M}$ molar, $\mu\mathrm{m} = 10^{-6}\mathrm{m}$ metres.

can be rewritten in dimensionless form using the following scalings

$$\begin{aligned}
&\tilde{x}_i = \frac{x_i}{L}, \quad \tilde{t} = P_l t, \quad \tilde{c} = \frac{P_l}{P_p}c, \quad \tilde{E} = \frac{P_l}{P_p}E, \quad \tilde{K}_d = \frac{P_l}{P_p}K_d,\\
&\tilde{B}_s = \frac{B_s k_{b,s}^+}{P_l}, \; \tilde{b}_s = \frac{b_s k_{b,s}^+}{P_l}, \; \tilde{B}_m = \frac{B_m k_{b,m}^+}{P_l}, \; \tilde{b}_m = \frac{b_m k_{b,m}^+}{P_l}, \; \tilde{k}_{b,s}^- = \frac{P_l k_{b,s}^-}{P_p k_{b,s}^+},\\
&\tilde{k}_{b,m}^- = \frac{P_l k_{b,m}^-}{P_p k_{b,m}^+}, \; \tilde{D}_c = \frac{D_c}{L^2 P_l}, \; \tilde{D}_{\scriptscriptstyle E} = \frac{D_{\scriptscriptstyle E}}{L^2 P_l}, \; \tilde{D}_{b,s} = \frac{D_{b,s}}{L^2 P_l},\\
&\tilde{D}_{b,m} = \frac{D_{b,m}}{L^2 P_l}, \quad \gamma_{b,s} = \frac{k_{b,s}^+ P_p}{P_l^2}, \quad \gamma_{b,m} = \frac{k_{b,m}^+ P_p}{P_l^2}, \quad \kappa = \tfrac{P_l + P_c}{P_l}.
\end{aligned} \tag{3.10}$$

For instance, we scale the first equation of (3.2) by dividing it by P_p to get

$$\begin{aligned}
\frac{1}{P_p}\frac{\partial c}{\partial t} =& \frac{D_c}{L^2 P_p}\Delta c + \frac{E}{P_p}(P_l + P_c) - \frac{c}{P_p}(P_l + P_c) - \frac{c^2}{K_d^2 + c^2} - \left(\frac{k_{b,s}^+(B_s - b_s)}{P_p}c - \frac{k_{b,s}^- b_s}{P_p}\right)\\
&- \left(\frac{k_{b,m}^+(B_m - b_m)}{P_p}c - \frac{k_{b,m}^- b_m}{P_p}\right).
\end{aligned} \tag{3.11}$$

Simple manipulation of (3.11) using $\left(\frac{P_l}{P_l}\right)$ leads to

$$\begin{aligned}\frac{\partial c(\frac{P_l}{P_p})}{\partial t(P_l)} =& \frac{D_c}{L^2 P_l}\Delta c\frac{P_l}{P_p} + \frac{E}{P_p}(P_l + P_c)\frac{P_l}{P_l} - \frac{c}{P_p}(P_l + P_c)\frac{P_l}{P_l} - \frac{c^2}{K_d^2 + c^2}\\ &- \left(\left(\frac{k_{b,s}^+(B_s - b_s)}{P_l}\right)\left(\frac{cP_l}{P_p}\right) - \left(\frac{k_{b,s}^+ b_s}{P_l}\right)\left(\frac{k_{b,s}^- P_l}{k_{b,s}^+ P_p}\right)\right)\\ &- \left(\left(\frac{k_{b,m}^+(B_m - b_m)}{P_l}\right)\left(\frac{cP_l}{P_p}\right) - \left(\frac{k_{b,m}^+ b_m}{P_l}\right)\left(\frac{k_{b,m}^- P_l}{k_{b,m}^+ P_p}\right)\right)\end{aligned}$$

so that we obtain a dimensionless form of the first equation of (3.2) as

$$\frac{\partial \tilde{c}}{\partial \tilde{t}} = \tilde{D}_c\Delta\tilde{c} + \kappa(\tilde{E} - \tilde{c}) - \frac{\tilde{c}^2}{\tilde{K}_d^2 + \tilde{c}^2} - ((\tilde{B}_s - \tilde{b}_s)\tilde{c} - \tilde{b}_s\tilde{k}_{b,s}^-) - ((\tilde{B}_m - \tilde{b}_m)\tilde{c} - \tilde{b}_m\tilde{k}_{b,m}^-).$$

The second equation is scaled in an analogous way. We consider the third equation of (3.2) and proceed as follows,

$$\begin{aligned}\frac{P_l^2}{k_{b,m}^+}\frac{\partial\left(\frac{b_m k_{b,m}^+}{P_l}\right)}{\partial t(P_l)} &= \frac{D_{b,m}P_l}{L^2 k_{b,m}^+}\Delta\left(\frac{b_m k_{b,m}^+}{P_l}\right) + \frac{P_p k_{b,m}^+}{P_l}(B_m - b_m)\frac{cP_l}{P_p} - \frac{k_{b,m}^- P_l}{k_{b,m}^+}\frac{b_m k_{b,m}^+}{P_l}\\ \frac{P_l^2}{k_{b,m}^+}\frac{\partial\tilde{b}_m}{\partial\tilde{t}} &= \frac{D_{b,m}P_l^2}{L^2 k_{b,m}^+ P_l}\Delta\tilde{b}_m + P_p(\tilde{B}_m - \tilde{b}_m)\tilde{c} - \frac{k_{b,m}^- P_l}{k_{b,m}^+}\tilde{b}_m\\ \frac{\partial\tilde{b}_m}{\partial\tilde{t}} &= \tilde{D}_{b,m}\Delta\tilde{b}_m + \frac{P_p k_{b,m}^+}{P_l^2}(\tilde{B}_m - \tilde{b}_m)\tilde{c} - \frac{k_{b,m}^-\tilde{b}_m}{P_l}\\ &= \tilde{D}_{b,m}\Delta\tilde{b}_m + \frac{P_p k_{b,m}^+}{P_l^2}\left((\tilde{B}_m - \tilde{b}_m)\tilde{c} - \frac{k_{b,m}^- P_l}{P_p k_{b,m}^+}\tilde{b}_m\right)\\ &= \tilde{D}_{b,m}\Delta\tilde{b}_m + \gamma_{b,m}((\tilde{B}_m - \tilde{b}_m)\tilde{c} - \tilde{k}_{b,m}^-\tilde{b}_m).\end{aligned}$$

Similar computations apply to the fourth equation. The dimensionless form of the system (3.2) with omitted tildes in the new variables is then given by

$$\begin{aligned}\frac{\partial c}{\partial t} &= D_c\Delta c + \kappa(E - c) - \frac{c^2}{K_d^2 + c^2} - (B_s - b_s + B_m - b_m)\,c + k_{b,s}^- b_s + k_{b,m}^- b_m,\\ \frac{\partial E}{\partial t} &= D_{\scriptscriptstyle E}\Delta E - \gamma\left(\kappa(E - c) - \frac{c^2}{K_d^2 + c^2}\right),\\ \frac{\partial b_m}{\partial t} &= D_{b,m}\Delta b_m + \gamma_{b,m}\left((B_m - b_m)\,c - k_{b,m}^- b_m\right),\\ \frac{\partial b_s}{\partial t} &= D_{b,s}\Delta b_s + \gamma_{b,s}\left((B_s - b_s)\,c - k_{b,s}^- b_s\right).\end{aligned} \tag{3.12}$$

We consider for this version the properties (**P**) and (**M**). If we denote

$$\begin{aligned} f_1(c,E,b_m,b_s) &= \kappa(E-c) - \frac{c^2}{K_d^2+c^2} - (B_s - b_s + B_m - b_m)c + k_{b,s}^- b_s + k_{b,m}^- b_m, \\ f_2(c,E,b_m,b_s) &= -\gamma \left(\kappa(E-c) - \frac{c^2}{K_d^2+c^2} \right), \\ f_3(c,E,b_m,b_s) &= \gamma_{b,m}((B_m - b_m)c - k_{b,m}^- b_m), \\ f_4(c,E,b_m,b_s) &= \gamma_{b,s}((B_s - b_s)c - k_{b,s}^- b_s), \end{aligned} \tag{3.13}$$

then we have

$$\begin{aligned} f_1(0,E,b_m,b_s) &= \kappa E + k_{b,s}^- b_s + k_{b,m}^- b_m \geq 0, \\ f_2(c,0,b_m,b_s) &= \gamma \left[\kappa c + \frac{c^2}{K_d^2+c^2} \right] \geq 0, \\ f_3(c,E,0,b_s) &= \gamma_{b,m} B_m c \geq 0, \\ f_4(c,E,b_m,0) &= \gamma_{b,s} B_s c \geq 0. \end{aligned} \tag{3.14}$$

so that nonnegativity is satisfied. For the second property, we have

$$\gamma f_1(c,E,b_m,b_s) + f_2(c,E,b_m,b_s) + \frac{\gamma}{\gamma_{b,m}} f_3(c,E,b_m,b_s) + \frac{\gamma}{\gamma_{b,s}} f_4(c,E,b_m,b_s) = 0,$$

which satisfies (3.9) with $C = 0$, hence mass is controlled. One can easily verify that system (3.2) also satisfies the (**P**) and (**M**) condition. We will utilize these two important properties in the analysis of our model.

3.3 Existence of local strong solutions

In this section, we formulate a local existence result for system (3.12) using semigroup theory. As for systems of ODEs, this local strong solution is proved via a fixed-point argument. The difference here is that we need to work in infinite dimensional functional spaces. More precisely, one chooses an adequate ball $\mathcal{B}$ in $C(Q_T, \mathbb{R}^m)$ equipped with the $L^\infty(Q_T)$-norm and we consider the mapping $\hat{\mathbf{u}} \in \mathcal{B} \to \mathbf{u} = (u_1, \ldots, u_m) \in \mathcal{B}$, solution of

$$\partial_t \mathbf{u} - d_i \Delta \mathbf{u} = \mathbf{f}(\hat{\mathbf{u}}) \text{ } on \text{ } Q_T, \ \ \partial_n \mathbf{u} = \mathbf{0} \text{ } on \text{ } \Sigma_T, \ \ \mathbf{u}(0,\cdot) = \mathbf{u}_0.$$

By the local Lipschitz property of $\mathbf{f}$, this is a strict contraction if T is small enough. Whence the existence of a unique solution on $[t_0, T]$ and on a maximal interval $[t_0, T^*[$ follow. The solution obtained in this way is regular due to the strong regularizing properties of the heat operator, see e.g., Pierre [127].

Assumption 3.3.1 (see Pierre [126] and Rothe [138, p. 110])**.** *Let the nonlinearities* $\mathbf{f} : Q_T \times [0, \infty[^m \to \mathbb{R}^m$ *be measurable functions with* $\mathbf{f}(\cdot, \mathbf{0}) \in [L^1(Q_T)]^m$*. Suppose that for* $R > 0$*, there exists a function* $K : Q_T \times [0, \infty[\to [0, \infty[, \quad K(\cdot, R) \in L^\infty(Q_T)$*. Also for all* $\mathbf{r}, \hat{\mathbf{r}} \in [0, \infty[^m$ *with* $|\mathbf{r}|, |\hat{\mathbf{r}}| \le R$*,* $0 < \vartheta \le 1$ *and* $(t, x) \in Q_T$*, let*

$$|\mathbf{f}(x, \mathbf{r}) - \mathbf{f}(x, \hat{\mathbf{r}})| \le K(x, R)(|x - \hat{x}|^\vartheta + |\mathbf{r} - \hat{\mathbf{r}}|) \quad a.e. \quad for\ x, \hat{x} \in \Omega. \tag{3.15}$$

Further, we assume quasi-positivity **(P)** *i.e.,*

$$f_i(x, r_1, \ldots, r_{i-1}, 0, r_{i+1}, \ldots, r_m) \ge 0, \quad for\ all \quad \mathbf{r} \in [0, \infty[^m.$$

The step function defined in (3.3) introduces an x dependence and a discontinuity for f_1 and f_2 in (3.13). Therefore, in order for system (3.2) to satisfy the conditions of Assumption 3.15, we mollify these f_i using the standard mollifier described in Evans [62, C. 4]. The function

$$\eta(x) = \begin{cases} C \exp\left(\frac{1}{|x|^2 - 1}\right) & \text{if } |x| < 1 \\ 0 & \text{if } |x| \ge 1, \end{cases}$$

belongs to $C^\infty(\mathbb{R}^N)$ for any constant $C > 0$. The constant is selected so that $\int_{\mathbb{R}^N} \eta \, dx = 1$. For any $\epsilon > 0$ we define the function

$$\eta_\epsilon(x) = \frac{1}{\epsilon^N} \eta\left(\frac{x}{\epsilon}\right). \tag{3.16}$$

Then η_ϵ is a C^∞ function with integral equal to one and whose support is the closed ball $\bar{B}_\epsilon(0)$. We refer to (3.16) as the *standard mollifier.* Let

$$\Omega_\epsilon = \{x \in \Omega : \ \text{dist}\,(x, \partial\Omega) > \epsilon\}.$$

Since $\mathbf{f} : \Omega \to \mathbb{R}$ is locally integrable, we define the mollification

$$\mathbf{f}^\epsilon(x, \mathbf{u}) = \int_\Omega \eta_\epsilon(x - y) \mathbf{f}(y, \mathbf{u}) dy$$

for $x \in \Omega_\epsilon$ so that $B_\epsilon(x) \subset \Omega$. The function $\mathbf{f}^\epsilon$ is a smooth approximation of $\mathbf{f}$. Also, we have

$$\begin{aligned} \max_{x \in \Omega} |\mathbf{f}^\epsilon(x, \mathbf{u})| &= \left| \int_\Omega \eta_\epsilon(x - y) \mathbf{f}(y, \mathbf{u}) \, dy \right| \\ &\le \int_\Omega \eta_\epsilon(x - y) \, dy \cdot \|\mathbf{f}\|_\infty = \|\mathbf{f}\|_\infty \end{aligned}$$

so that

$$\|\mathbf{f}^\epsilon\|_\infty \le \|\mathbf{f}\|_\infty. \tag{3.17}$$

In addition, the following properties hold for standard mollifiers. A proof can be found in Evans [62, C. 4].

Lemma 3.3.2.

(i) $\mathbf{f}^\epsilon \in C^\infty(\Omega_\epsilon)$.

(ii) $\mathbf{f}^\epsilon \to \mathbf{f}$ *a.e. as* $\epsilon \to 0$.

(iii) If $1 \leq p < \infty$ *and* $\mathbf{f} \in L^p_{loc}(\Omega)$, *then* $\mathbf{f}^\epsilon \to \mathbf{f}$ *in* $L^p_{loc}(\Omega)$.

We will first construct solutions $\mathbf{u}^\epsilon$ corresponding to $\mathbf{f}^\epsilon$ and later use a limiting procedure to show that $\mathbf{u}^\epsilon \to \mathbf{u}$ pointwise almost everywhere as $\epsilon \to 0$.

Definition 3.3.3. *A* **strong solution** *to* (3.4) *on* $[t_0, T[$ *means that, for all* $k, l = 1, \ldots, N$ *and for all* $p \in [1, \infty[$, *at least the following conditions hold*

$$\begin{cases} \mathbf{u} \in C([t_0, T[, L^1(\Omega)^m) \cap L^\infty([t_0, T-\tau] \times \Omega)^m, \ \textit{for all } \tau \in]t_0, T[, \\ \partial_t \mathbf{u}, \partial_{x_k} \mathbf{u}, \partial_{x_k x_l} \mathbf{u} \in L^p(]\tau, T-\tau[\times \Omega)^m, \\ \textit{and the equations in } (3.4) \textit{ are satisfied a.e..} \end{cases} \tag{3.18}$$

Note that the regularity of $\mathbf{u}$ in Definition 3.3.3 implies that $\mathbf{u}, \partial_{x_k}\mathbf{u}$ have traces in $L^p_{loc}(\Sigma_T)^m$, see e.g., Ladyženskaja et al. [97]. Most of the time, due to more regularity of $\mathbf{f}$, the solutions will be regular enough so that derivatives may be understood in the classical sense, e.g., $\mathbf{u} \in C^2(]t_0, T[\times\bar{\Omega})$ if $\mathbf{f} \in C^2(]t_0, T[\times\bar{\Omega})$ itself, see e.g., Pierre [126].

We consider the reaction-diffusion system (3.4) where the following basic hypotheses are assumed to hold, for all $i = 1, \ldots, m$

(H1) the d_i are constants with $d_i > 0$.

(H2) the functions $\mathbf{f}$ have the property defined in (3.15).

(H3) the functions u_{i0} are measurable on Ω and there is an M_{i0} such that $0 \leq u_{i0}(x) \leq M_{i0}$ for all $x \in \Omega$.

Theorem 3.3.4. *Suppose that (H1)-(H3) are satisfied. Then* (3.4) *has a unique local strong solution* $(u_i)_{i=1,\ldots,m}$ *on* $[t_0, T^*[\times\Omega$, *where* $T^* > t_0$, $t_0 \in \mathbb{R}$. *Further, there are continuous functions* $G_i : [t_0, T^*[\to [0, \infty[$ *such that*

$$0 \leq u_i(t, x) \leq G_i(t) \quad \textit{for } (t, x) \in [t_0, T^*[\times \Omega. \tag{3.19}$$

Note that our specific system (3.2) is such a system with $m = 4$ This local existence result follows from the basic existence theory for abstract semilinear parabolic differential equations, see e.g., Henry [81, Sect. 3.3]. We extend the ideas of the proof in these results for scalar equations to systems of parabolic equations and prove Theorem 3.3.4 in Subsection 3.3.2.

In general, (H1)-(H3) are not sufficient to ensure that solutions to (3.4) exist for all $t \geq 0$. This chapter aims at giving sufficient conditions guaranteeing that $T^* = \infty$ in Theorem 3.3.4, i.e., we establish a result on the uniform boundedness of solutions on $[t_0, \infty[\times \Omega$ so that (3.19) holds with $T^* = \infty$. We realize this in Section 3.4, Theorem 3.4.1, using the invariant region approach.

The Duhamel formula provides a useful way to study semilinear evolution equations of the form

$$u_t = Au + f(u) \tag{3.20}$$

where the linear operator A generates a semigroup on a Banach space X and

$$f : \mathcal{D}(F) \subset X \to X$$

is a nonlinear function. For semilinear PDEs, $f(u)$ depends on u but none of its spatial derivatives and then (3.20) consists of a linear PDE perturbed by a zeroth-order nonlinear term. If $\{S(t)\}$ is the semigroup generated by A, we may replace (3.20) by an integral equation for $u : [0, T] \to X$

$$u(t) = S(t)u(0) + \int_0^t S(t-s) f(u(s))\, ds. \tag{3.21}$$

We then show that solutions of this integral equation exist. If these solutions have sufficient regularity, then they also satisfy (3.20).

In the standard Picard approach to ODEs, we would write (3.20) as

$$u(t) = u(0) + \int_0^t [Au(s) + f(u(s))]\, ds. \tag{3.22}$$

The advantage of(3.21) over (3.22) is that we have replaced the unbounded operator A by the bounded solution operators $\{S(t)\}$. Moreover, since $S(t-s)$ acts on $f(u(s))$ it is possible for the regularizing properties of the linear operators S to compensate for the destabilizing effects of the nonlinearity F, see Hunter [88, Sect. 5.4]. The family of bounded linear operators $\{S(t) : t \geq 0\}$ is called a semigroup because it satisfies

$$\begin{cases} (i) & S(0) = I, \\ (ii) & S(t)S(s) = S(t+s) \quad t, s \geq 0. \end{cases} \tag{3.23}$$

3.3.1 Elliptic boundary value problems and semigroups in $L^p(\Omega)$

Let Ω be a bounded domain with smooth boundary $\partial\Omega$ in $\mathbb{R}^N$ and let $A(x, D)$ be the symmetric second order differential operator given by

$$A(x, D)u = \sum_{k,l=1}^{N} \frac{\partial}{\partial x_k} \left(a_{k,l}(x) \frac{\partial u}{\partial x_l} \right) \tag{3.24}$$

with real uniformly continuous and bounded coefficients $a_{k,l}$. We assume that the coefficients $a_{k,l}(x) = a_{l,k}(x)$ satisfies the uniform ellipticity condition, i.e., there is a constant $C_0 > 0$ such that

$$\sum_{k,l=1}^{N} a_{k,l}(x)\xi_k\xi_l \geq C_0|\xi|^2, \quad x \in \bar{\Omega} \tag{3.25}$$

for all $\xi \in \mathbb{R}^N$.

With the second order symmetric differential operator $A(x, D)$ given by (3.24), we associate the operator A_p on $L^p(\Omega)$, $1 < p < \infty$ defined as follows, see e.g., Lunardi [102, Sect. 3.1]

$$\mathcal{D}(A_p) = \{u \in W^{2,p}(\Omega) : a_{k,l}(x)\frac{\partial u}{\partial n} = 0 \text{ on } \partial\Omega\} \tag{3.26}$$

and

$$A_p u = A(x, D)u \quad \text{for } \ u \in \mathcal{D}(A_p). \tag{3.27}$$

Here, $W^{2,p}(\Omega)$ is the Sobolev space of functions with generalized derivatives of second order in $L^p(\Omega)$. With the above definition (3.26) and (3.27), it follows that the domain $\mathcal{D}(A_p)$ of A_p is dense in $L^p(\Omega)$, see e.g., Agmon [2] or Amann [6]. Moreover, by Lunardi [102, Thm. 3.1.1] or Agmon [2], the operator A_p satisfies

$$\|u\|_{W^{2,p}(\Omega)} \leq C(\|u\|_{L^p(\Omega)} + \|A_p u\|_{L^p(\Omega)}) \tag{3.28}$$

where the constant C depends on A_p, Ω and p but not on u. It therefore follows from Rothe [138, Lemma I.1] that A_p is a closed operator in the Banach space $L^p(\Omega)$. From Lunardi [102, Sect. 3.1], the resolvent set $\rho(A_p)$ of the operator A_p contains a half-plane $\{\lambda \in \mathbb{C} : \operatorname{Re}\lambda \geq \lambda_0\}$ for some $\lambda_0 \in \mathbb{R}$, and there is a constant k such that

$$|\lambda|\|u\|_{L^p(\Omega)} \leq k\|(\lambda - A_p)u\|_{L^p(\Omega)}, \qquad u \in \mathcal{D}(A_p), \qquad \operatorname{Re}\lambda \geq \lambda_0. \tag{3.29}$$

A proof of the estimate (3.29) in a more generalized situation can be found in Lunardi [102, Thm. 3.1.3]. Therefore, the operator A_p is sectorial, see Appendix A for a definition of sectorial operators. Consequently, A_p considered as an unbounded linear operator in $L^p(\Omega)$ with domain $\mathcal{D}(A_p)$, is the infinitesimal generator of a strongly continuous analytic semigroup $\{S_p(t) = e^{tA_p} : t \geq 0\}$ on $L^p(\Omega)$ for $1 < p < \infty$, see e.g., Lunardi [102, p. 34]. The analytic semigroup $S_p(t)$ is a bounded linear operator on $L^p(\Omega)$ defined through the Dunford integral

$$e^{tA_p} = \frac{1}{2\pi i}\int_{\gamma} e^{t\lambda}(\lambda I - A_p)^{-1}\, d\lambda, \ \ t > 0, \tag{3.30}$$

where γ is a suitable curve with support in the resolvent set of A_p. Here, $\gamma \subset \mathbb{C}$ is chosen as any circle centred at the origin and radius $r > \|A_p\|$. The function $t \mapsto e^{tA_p}$ belongs to $C^\infty(]0,\infty[, L^p(\Omega))$, and it enjoys the semigroup property in (3.23), see e.g., Lunardi [102, Sect. 2.1]. The integral (3.30) converges for $t > 0$ in the uniform operator topology, see e.g., Pazy [123, Thm. 1.7.7]. Also, from Pazy [123, Thm. 2.6.13], the operator $S_p(t)$ satisfy the inequality

$$\|S_p(t+h) - S_p(t)\|_{L^p(\Omega)} \leq h\|A_p S_p(t)\|_{L^p(\Omega)} \tag{3.31}$$

which holds for analytic semigroups for every $t > 0$ and $h \geq 0$. It therefore follows that $S_p(t)$ is continuous in the uniform operator topology for $t > 0$. Since the imbedding $W^{2,p}(\Omega) \subset L^p(\Omega)$ is compact for all $p \in]1, \infty[$, A_p has a compact resolvent, see e.g., Amann [6, Sect. 7]. Hence it follows from Pazy's theorem [123, Thm. 2.3.3] that the semigroup $S_p(t)$ is compact on $L^p(\Omega)$ for $t > 0$ and $\lambda \in \rho(A_p)$. In summary, *A_p generates a compact strongly continuous analytic semigroup on $L^p(\Omega)$.*

Remark 3.3.5. From Rothe [138, Lemma I.1], the operators $S_\infty(t)$ can be defined as the restriction of $S_p(t)$ to the space $L^\infty(\Omega)$. These operators are well defined independent of p and are continuous from $L^\infty(\Omega)$ to $L^\infty(\Omega)$. Furthermore, they define a formal semigroup in $L^\infty(\Omega)$ which is not a strongly continuous semigroup. Similarly the operators $S_p(t)$ can be uniquely extended to continuous operators $S_1(t)$ from $L^1(\Omega)$ to $L^1(\Omega)$. The operators $S_1(t)$ form a strongly continuous semigroup in the space $L^1(\Omega)$.

3.3.2 Semigroup formulation for the system

For each $p \in]1, \infty[$ and for all $i = 1, \ldots, 4$, we define the operators $\mathbf{A}_p = (A_{1,p}, \ldots, A_{4,p})$ on the space $L^p(\Omega)$ by

$$\begin{cases} \mathbf{A}_p\mathbf{u} & = & d_i\Delta\mathbf{u} \quad \text{for } \mathbf{u} \in \mathcal{D}(\mathbf{A}_p), \quad \text{and} \\ \mathcal{D}(\mathbf{A}_p) & = & \{\mathbf{u} \in W^{2,p}(\Omega) : d_i\frac{\partial\mathbf{u}}{\partial n} = 0 \text{ on } \partial\Omega\} \end{cases} \tag{3.32}$$

where $W^{2,p}(\Omega)$ is the usual Sobolev space, see Adams [1] and the coefficients d_i satisfy (H1). It now follows from Subsection 3.3.1 that, under the assumption (H1), the operators $\mathbf{A}_p$ are the infinitesimal generators of compact analytic semigroups $\mathbf{S}_p = \{\mathbf{S}_p(t) : t \geq 0\}$ of bounded linear operators on $L^p(\Omega)$. Note that if $\mathbf{A}_p$ are the infinitesimal generators of analytic semigroups, then $\delta\mathbf{I} - \mathbf{A}_p$ are still infinitesimal generators of analytic semigroups for $\delta > 0$, see e.g., Pazy [123, p. 70]. Moreover, it follows that there is a constant $M_0 > 0$ such that

$$\|\mathbf{S}_p(t)\mathbf{u}\|_p \leq M_0 e^{-\delta t}\|\mathbf{u}\|_p \quad \text{for } t \geq 0, \ \mathbf{u} \in L^p(\Omega) \tag{3.33}$$

and

$$\|\mathbf{u}\|_p = \left[\int_\Omega |\mathbf{u}(x)|^p \, dx\right]^{1/p}.$$

In order to deal with the nonlinearities of the f_i in (3.2), we use fractional powers of the operators $\mathbf{A}_p$. From the well known representation formula of the resolvent operator, see e.g., Tanabe [151, p. 4]

$$(\lambda \mathbf{I} - \mathbf{A}_p)^{-1} = \int_0^\infty e^{-\lambda t}\mathbf{S}_p(t)\, dt,$$

for $\alpha > 0$ and $\lambda > \delta$ the fractional powers

$$(\lambda \mathbf{I} - \mathbf{A}_p)^{-\alpha} = \frac{1}{\Gamma(\alpha)} \int_0^\infty t^{\alpha-1} e^{-\lambda t}\mathbf{S}_p(t)\, dt$$

exist and are injective, bounded linear operators on $L^p(\Omega)$, see e.g., Pazy [123, p. 70]. For each $\alpha > 0$ define $\mathbf{B}_p^{-\alpha} = (\lambda \mathbf{I} - \mathbf{A}_p)^{-\alpha}$ and $\mathbf{B}_p^{\alpha} = (\mathbf{B}_p^{-\alpha})^{-1}$. We follow Pazy [123, Sect. 6.3] and note that $\mathbf{B}_p^\alpha$ are closed linear operators with domain $\mathcal{D}(\mathbf{B}_p^\alpha)$ dense in $L^p(\Omega)$. Recall that the closedness of $\mathbf{B}_p^\alpha$ implies that $\mathcal{D}(\mathbf{B}_p^\alpha)$ endowed with the graph norm of $\mathbf{B}_p^\alpha$, i.e., the norm $|||\mathbf{u}|||_\alpha = \|\mathbf{u}\|_p + \|\mathbf{B}_p^\alpha \mathbf{u}\|_p$, is a Banach space. Since $\mathbf{B}_p^\alpha$ is invertible, its graph norm $||| \cdot |||$ is equivalent to the norm $\|\mathbf{u}\|_\alpha = \|\mathbf{B}_p^\alpha \mathbf{u}\|_p$. Thus, $\mathcal{D}(\mathbf{B}_p^\alpha)$ equipped with the norm $\| \ \|_\alpha$ is a Banach space. From this definition it is clear that for $0 < \alpha < \beta \le 1$ we have $\mathcal{D}(\mathbf{B}_p^\alpha) \supset \mathcal{D}(\mathbf{B}_p^\beta)$ and that the imbedding of $\mathcal{D}(\mathbf{B}_p^\beta)$ in $\mathcal{D}(\mathbf{B}_p^\alpha)$ is continuous , see Pazy [123, Sect. 6.3]. Since the operators $\mathbf{A}_p$ have compact resolvents, the inclusion $\mathcal{D}(\mathbf{B}_p^\alpha) \supset \mathcal{D}(\mathbf{B}_p^\beta)$ is compact when $0 \le \alpha < \beta$. We use the convention $\mathcal{D}(\mathbf{B}_p^0) = L^p(\Omega)$, see Henry [81, Thm. 1.4.8]. Also, see Henry [81, p. 40], we have

$$\begin{cases} \text{if } \alpha > \frac{N}{2p} \text{ then } \mathcal{D}(\mathbf{B}_p^\alpha) \subset L^\infty(\Omega), \quad \text{and} \\ \|\mathbf{u}\|_\infty \le M_{\alpha,p}\|\mathbf{B}_p^\alpha \mathbf{u}\|_p \quad \text{for all } \mathbf{u} \in \mathcal{D}(\mathbf{B}_p^\alpha). \end{cases} \tag{3.34}$$

In addition, the following properties are satisfied by $\mathbf{S}_p$ and $\mathbf{B}_p^\alpha$. These follow from Pazy's theorem [123, Thm. 2.6.13] which we recall in Lemma 3.3.6 below.

Lemma 3.3.6. *Suppose that* $\mathbf{S}_p$ *and* $\mathbf{B}_p^\alpha$ *are as above. Then*

(i) $\mathbf{S}_p(t) : L^p(\Omega) \to \mathcal{D}(\mathbf{B}_p^\alpha)$ *for all* $t > 0$,

(ii) $\|\mathbf{B}_p^\alpha \mathbf{S}_p(t)\mathbf{u}\|_p \le C_{\alpha,p} t^{-\alpha} e^{-\delta t}\|\mathbf{u}\|_p$ *for* $t > 0$ *and* $\mathbf{u} \in L^p(\Omega)$,

(iii) $\mathbf{S}_p(t)\mathbf{B}_p^\alpha \mathbf{u} = \mathbf{B}_p^\alpha \mathbf{S}_p(t)\mathbf{u}$ *for* $t > 0$, $\mathbf{u} \in \mathcal{D}(\mathbf{B}_p^\alpha)$,

(iv) $\|\mathbf{S}_p(t)\mathbf{u} - \mathbf{u}\|_p \le C_{\alpha,p} t^\alpha \|\mathbf{B}_p^\alpha \mathbf{u}\|_p$ *for* $0 < \alpha \le 1$, $\mathbf{u} \in \mathcal{D}(\mathbf{B}_p^\alpha)$.

The construction of solutions of the system (3.4) begins with bounded mild solutions and then turns to strong solutions, see Appendix A for definition of a mild solution. The first step in the study of the initial-boundary value problem (3.4) is to consider the linear system i.e., (3.4) with $f_i = 0$ for all i. Since the linear system is decoupled, the semigroup operator $\mathbf{S}_p$ acts componentwise in the variation of constants formula (3.21). We therefore use the local existence results in Pazy [123] or Henry [81], and write (3.4) as an integral equation system via variation of constants. So for all $i = 1, \dots, 4$, we define $\mathbf{F} = (F_1, F_2, F_3, F_4)$ on $[0, \infty) \times L^\infty(\Omega)^4$ by

$$[\mathbf{F}(\mathbf{u}(t))](x) = \mathbf{f}(\mathbf{u}(t,x)); \quad \text{for } x \in \Omega, \ \ t > 0, \ \ \mathbf{u} \in L^\infty(\Omega) \subset L^p(\Omega). \tag{3.35}$$

By variation of constants, see Pazy [123, Sect. 6.1], it follows that if $\mathbf{u}$ is a solution in $L^p(\Omega)^4$ to the system

$$\mathbf{u}(t) = \mathbf{S}_p(t - t_0)\mathbf{u_0} + \int_{t_0}^{t} \mathbf{S}_p(t - s)\mathbf{F}(\mathbf{u}(s))\, ds, \tag{3.36}$$

then $\mathbf{u}(t,x) = [\mathbf{u}(t)](x)$ is the solution of (3.4). The choice of the spaces $\mathcal{D}(\mathbf{B}_p^\alpha) \subset L^p(\Omega)$ such that $\mathbf{F} : \mathcal{D}(\mathbf{B}_p^\alpha) \to L^p(\Omega)$ is locally Lipschitz continuous, and $\mathbf{S}_p(t) : L^p(\Omega) \to \mathcal{D}(\mathbf{B}_p^\alpha)$ for $t > 0$ allows the smoothing of the semigroup to compensate for a loss of regularity in the nonlinearity. The smoothing of the semigroup and the initial data in $\mathcal{D}(\mathbf{B}_p^\alpha)$, with $0 < \alpha < 1$ guarantee that the solution is actually in $\mathcal{D}(\mathbf{A}_p)$ at any later time, see Henry [81, Sect. 3.5].

Proof of Theorem 3.3.4.
We will give the proof of the theorem in four stages. First, we show that there is a contraction mapping for the mollified problem that leads to a mild solution for $\mathbf{u_0} \in \mathcal{D}(\mathbf{B}_p^\alpha)$. Next, we show that the solution to the mollified problem is regular by proving that $\mathbf{F}$ is Hölder continuous on $]t_0, T^*]$. Then we consider the case with initial data in $L^\infty(\Omega)$. Finally, we pass to the limit to obtain the solution for the discontinuous reaction terms with $\mathbf{u_0} \in L^\infty(\Omega)^m$.

We select $\alpha \in]0, 1[$ and $p > 1$ so that (3.34) holds and use the techniques in Pazy [123, Sect. 6.3] or Henry [81, Sect. 3.3] to show the existence of a unique local solution $\mathbf{u}$ to (3.36) for

$$\mathbf{u}_0 \in [\mathcal{D}(\mathbf{B}_p^\alpha)]^m.$$

Also, the $\mathbf{u}(t)$ have nonnegative values on Ω since the nonlinearity $\mathbf{f}$ is **quasi-positive** for all $t \geq 0$.

Contraction mapping $\mathcal{T}$ for the mollified problem
Since the $\mathbf{f}$ are continuous, for each $R > 0$ there is an $M(R) > 0$ such that

$$|\mathbf{f}(\xi)| \leq M(R) \quad \text{for} \quad \xi \in [0, R].$$

Hence,

$$\|\mathbf{F}(\mathbf{u})\|_\infty \leq M(R) \quad \text{whenever} \;\; t \in [t_0, T] \;\; \text{and} \;\; \mathbf{u}(t) \in L^\infty(\Omega) \;\; \text{with} \;\; \|\mathbf{u}(t)\|_\infty \leq R. \tag{3.37}$$

From the second and third property of $\mathbf{B}_p^\alpha$ and $\mathbf{S}_p$ in Lemma 3.3.6, it follows that

$$\|\mathbf{S}_p(t)\mathbf{B}_p^\alpha\|_p = \|\mathbf{B}_p^\alpha \mathbf{S}_p(t)\|_p \leq C_{\alpha,p} t^{-\alpha} \qquad \text{for} \quad t > 0. \tag{3.38}$$

We also have by Pazy [123, p. 71]

$$\|\mathbf{B}_p^{-\alpha}\|_p \leq C. \tag{3.39}$$

Let us fix t_0 and, $\mathbf{u}_0 \in [\mathcal{D}(\mathbf{B}_p^\alpha)]^m$ and choose $t_1 > t_0$, $\varepsilon_i > 0$ for $i = 1, \ldots, m$ such that the estimate (3.15) holds in the set $V = \{(t, \mathbf{u}) : t_0 \leq t \leq t_1, \; \|\mathbf{u} - \mathbf{u}_0\|_\infty \leq \varepsilon_i\}$. From (3.34), we have $[\mathcal{D}(\mathbf{B}_p^\alpha)]^m \subset [L^\infty(\Omega)]^m$. We choose T^* such that for $\varepsilon = \min_{1 \leq i \leq m} \varepsilon_i$

$$\|\mathbf{S}_p(t - t_0)\mathbf{B}_p^\alpha \mathbf{u}_0 - \mathbf{B}_p^\alpha \mathbf{u}_0\|_\infty \leq \frac{\varepsilon}{2} \quad \text{for} \quad t_0 \leq t \leq T^* \tag{3.40}$$

and using $K(x, \varepsilon)$ from (3.15), $M(\varepsilon)$ and $C_{\alpha,p}$ from above

$$0 < T^* - t_0 < \min\left\{ t_1 - t_0, \; \left[\frac{\varepsilon}{2}(1 - \alpha) C_{\alpha,p}^{-1} (M + \varepsilon K)^{-1}\right]^{\frac{1}{1-\alpha}} \right\}. \tag{3.41}$$

Let Y be the Banach space $C([t_0, T^*]; [\mathcal{D}(B_{i,p}^\alpha)]^m)$ provided with the supremum norm defined by

$$\|\mathbf{y}\|_Y = \sup_{t \in [t_0, T^*]} \{\|\mathbf{y}(t)\|_{L^p(\Omega)}, \quad t_0 \leq t \leq T^*\}, \quad \mathbf{y} \in Y.$$

From (3.36), set $\mathbf{u}(t) = \mathbf{B}_p^{-\alpha}\mathbf{y}(t)$ for $\mathbf{y} \in Y$ and define $\mathbf{z}(t) = \mathbf{B}_p^{-\alpha}\mathbf{y}(t)$. We then consider the equation

$$\mathbf{y}(t) = \mathbf{S}_p(t - t_0)\mathbf{B}_p^\alpha \mathbf{u}_0 + \int_{t_0}^t \mathbf{B}_p^\alpha \mathbf{S}_p(t - s)\mathbf{F}(\mathbf{z}(s))\, ds. \tag{3.42}$$

Note that if $\mathbf{y} : [t_0, T^*] \to \mathcal{D}(\mathbf{B}_p^\alpha)$ is continuous and satisfies (3.42) for $t \in [t_0, T^*]$, then $\mathbf{u}(t) = \mathbf{B}_p^{-\alpha}\mathbf{y}(t)$ is a solution to (3.36) on $[t_0, T^*]$. On Y, we define a mapping $\mathcal{T} : Y \to Y$ by

$$\mathcal{T}\mathbf{y}(t) = \mathbf{S}_p(t - t_0)\mathbf{B}_p^\alpha \mathbf{u}_0 + \int_{t_0}^t \mathbf{B}_p^\alpha \mathbf{S}_p(t - s)\mathbf{F}(\mathbf{z}(s))\, ds. \tag{3.43}$$

The integral in (3.43) is an absolutely converging Bochner integral in the $L^1(\Omega)$ space, see e.g., Segal and Kunze [144, p. 169]. Therefore, one can easily deduce that the right-hand side of (3.43) is a continuous function on $[t_0, T^*]$ and it is clear that $\mathcal{T} : Y \to Y$. Also, for every $\mathbf{y} \in Y$, $\mathcal{T}\mathbf{y}(t_0) = \mathbf{B}_p^\alpha \mathbf{u}_0$. Let U be the nonempty closed and bounded subset of Y defined by

$$U = \{\, \mathbf{y} : \mathbf{y} \in Y,\ \mathbf{y}(t_0) = B_{i,p}^\alpha \mathbf{u}_0,\ \|\mathbf{y}(t) - \mathbf{B}_p^\alpha \mathbf{u}_0\|_Y \le \varepsilon \,\}. \tag{3.44}$$

We show that $\mathcal{T}$ maps U into itself, and $\mathcal{T}$ is a strict contraction. For $\mathbf{y} \in U$, we have using (3.43), (3.40), (3.38), (3.15), (3.44), and (3.37)

$$\begin{aligned}
\|\mathcal{T}\mathbf{y}(t) - \mathbf{B}_p^\alpha \mathbf{u}_0\|_Y &\le \|\mathbf{S}_p(t-t_0)\mathbf{B}_p^\alpha \mathbf{u}_0 - \mathbf{B}_p^\alpha \mathbf{u}_0\|_Y \\
&\quad + \Big\| \int_{t_0}^{t} \mathbf{B}_p^\alpha \mathbf{S}_p(t-s)[\mathbf{F}(\mathbf{z}(s)) - \mathbf{F}(\mathbf{u}_0)]\, ds \Big\|_Y \\
&\quad + \Big\| \int_{t_0}^{t} \mathbf{B}_p^\alpha \mathbf{S}_p(t-s)\mathbf{F}(\mathbf{u}_0)\, ds \Big\|_Y \\
&\le \frac{\varepsilon}{2} + C_{\alpha,p}(M + \varepsilon K) \int_{t_0}^{t} (t-s)^{-\alpha}\, ds.
\end{aligned}$$

Now we make use of (3.41) to obtain

$$\begin{aligned}
\|\mathcal{T}\mathbf{y}(t) - \mathbf{B}_p^\alpha \mathbf{u}_0\|_Y &\le \frac{\varepsilon}{2} + C_{\alpha,p}(1-\alpha)^{-1}(M + \varepsilon K)(T^* - t_0)^{1-\alpha} \\
&\le \varepsilon.
\end{aligned}$$

Therefore $\mathcal{T} : U \to U$. Furthermore, if $\mathbf{y}, \tilde{\mathbf{y}} \in U$ then

$$\begin{aligned}
\|\mathcal{T}\mathbf{y}(t) - \mathcal{T}\tilde{\mathbf{y}}(t)\|_Y &\le \int_{t_0}^{t} \|\mathbf{B}_p^\alpha \mathbf{S}_p(t-s)\|_p \, \|\mathbf{F}(\mathbf{z}(s)) - \mathbf{F}(\tilde{\mathbf{z}}(s))\|_Y \, ds \\
&\le K C_{\alpha,p}(1-\alpha)^{-1}(T^* - t_0)^{1-\alpha} \|\mathbf{y} - \tilde{\mathbf{y}}\|_Y \\
&\le \frac{1}{2} \|\mathbf{y} - \tilde{\mathbf{y}}\|_Y
\end{aligned}$$

which implies that

$$\|\mathcal{T}\mathbf{y} - \mathcal{T}\tilde{\mathbf{y}}\|_Y \le \frac{1}{2}\|\mathbf{y} - \tilde{\mathbf{y}}\|_Y \qquad \text{for } \mathbf{y}, \tilde{\mathbf{y}} \in U. \tag{3.45}$$

From the well known contraction principle, the mapping $\mathcal{T}$ has a unique fixed point $\mathbf{y} \in U$. For $t_0 \le t \le T^*$, this fixed point satisfy the integral equation

$$\mathbf{y}(t) = \mathbf{S}_p(t-t_0)\mathbf{B}_p^\alpha \mathbf{u}_0 + \int_{t_0}^{t} \mathbf{B}_p^\alpha \mathbf{S}_p(t-s)\mathbf{F}(\mathbf{z}(s))\, ds. \tag{3.46}$$

These mild solutions to (3.36) satisfy $\mathbf{u} \in C([t_0, T^*[; [L^p(\Omega)]^m)$, see e.g., Pazy [123, Sect. 6.1]. We show that these mild solutions are more regular by proving that $t \to \mathbf{F}(\mathbf{z}(t))$ is locally Hölder continuous on $]t_0, T^*]$.

Hölder continuity of the solution to the mollified problem
From (3.15) and the continuity of $\mathbf{y}$ it follows that $t \to \mathbf{F}(\mathbf{z}(t))$ is continuous on $[t_0, T^*]$ and a fortiori bounded on this interval. Let

$$\|\mathbf{F}(\mathbf{z}(t))\|_p \leq L_i \qquad \text{for } \; t_0 \leq t \leq T^*. \tag{3.47}$$

We prove that $t \to \mathbf{F}(\mathbf{z}(t))$ is locally Hölder continuous on $]t_0, T^*]$ by first showing that the solution $\mathbf{y}$ of (3.46) is locally Hölder continuous on $]t_0, T^*]$. We note that for every β satisfying $0 < \beta < 1 - \alpha$ and every $0 < h < 1$ we have by the last property of Lemma 3.3.6

$$\begin{aligned}\|(\mathbf{S}_p(h) - I)\mathbf{B}_p^\alpha \mathbf{S}_p(t-s)\|_p &\leq C_\beta h^\beta \|\mathbf{B}_p^{(\alpha+\beta)}\mathbf{S}_p(t-s)\|_p \\ &\leq C h^\beta (t-s)^{-(\alpha+\beta)}.\end{aligned} \tag{3.48}$$

If $t_0 < t < t + h \leq T^*$, then

$$\begin{aligned}\mathbf{y}(t+h) - \mathbf{y}(t) &= \mathbf{S}_p(t+h-t_0)\mathbf{B}_p^\alpha \mathbf{u}_0 - \mathbf{S}_p(t-t_0)\mathbf{B}_p^\alpha \mathbf{u}_0 \\ &\quad + \int_{t_0}^{t+h} \mathbf{B}_p^\alpha \mathbf{S}_p(t+h-s)\mathbf{F}(\mathbf{z}(s))\,ds - \int_{t_0}^{t} \mathbf{B}_p^\alpha \mathbf{S}_p(t-s)\mathbf{F}(\mathbf{z}(s))\,ds \\ &= \mathbf{S}_p(h)\,\mathbf{S}_p(t-t_0)\mathbf{B}_p^\alpha \mathbf{u}_0 - \mathbf{S}_p(t-t_0)\mathbf{B}_p^\alpha \mathbf{u}_0 \\ &\quad + \int_{t}^{t+h} \mathbf{B}_p^\alpha \mathbf{S}_p(t+h-s)\mathbf{F}(\mathbf{z}(s))\,ds + \int_{t_0}^{t} \mathbf{B}_p^\alpha \mathbf{S}_p(t+h-s)\mathbf{F}(\mathbf{z}(s))\,ds \\ &\quad - \int_{t_0}^{t} \mathbf{B}_p^\alpha \mathbf{S}_p(t-s)\mathbf{F}(\mathbf{z}(s))\,ds,\end{aligned}$$

so that

$$\begin{aligned}\|\mathbf{y}(t+h) - \mathbf{y}(t)\|_p \leq\,& \|(\mathbf{S}_p(h) - I)\mathbf{B}_p^\alpha \mathbf{S}_p(t-t_0)\mathbf{u}_0\|_p \\ &+ \int_{t_0}^{t} \|(\mathbf{S}_p(h) - I)\mathbf{B}_p^\alpha \mathbf{S}_p(t-s)\mathbf{F}(\mathbf{z}(s))\|_p\,ds \\ &+ \int_{t}^{t+h} \|\mathbf{B}_p^\alpha \mathbf{S}_p(t+h-s)\mathbf{F}(\mathbf{z}(s))\|_p\,ds \\ =& I_1 + I_2 + I_3.\end{aligned} \tag{3.49}$$

Using (3.47) and (3.48), we estimate each of the terms of (3.49) as follows

$$I_1 \leq C(t-t_0)^{-(\alpha+\beta)} h^\beta \|\mathbf{u}_0\| \leq\ M_1 h^\beta \tag{3.50}$$

$$I_2 \leq CLh^\beta \int_{t_0}^{t} (t-s)^{-(\alpha+\beta)}\, ds \leq\ M_2 h^\beta \tag{3.51}$$

$$I_3 \leq LC_\alpha \int_{t}^{t+h} (t+h-s)^{-\alpha}\, ds =\ \frac{LC_\alpha}{1-\alpha} h^{1-\alpha} \leq\ M_3 h^\beta \tag{3.52}$$

where we have used $L = \max_{1\leq i\leq m} L_i$. Evaluating the integrals in (3.51) and (3.52) shows that M_2 and M_3 can be chosen to be independent of $t \in [t_0, T^*]$, but M_1 depends on t and blows up at $t \to t_0$. Combining (3.49) with estimates (3.50)-(3.52) and setting $h = (t-s)$, it follows that for every $t_0' > t_0$ there are constants C_i such that

$$\|\mathbf{y}(t) - \mathbf{y}(s)\|_p \leq\ C_i |t-s|^\beta \qquad \text{for } \ t_0 < t_0' \leq t, s \leq T^* \tag{3.53}$$

and therefore $\mathbf{y}$ is locally Hölder continuous on $]t_0, T^*]$. The local Hölder continuity of $t \to \mathbf{F}(\mathbf{z}(t))$ on $]t_0, T^*]$ now follows from

$$\begin{aligned} \|\mathbf{F}(\mathbf{z}(t)) - \mathbf{F}(\mathbf{z}(s))\| &\leq K\|\mathbf{y}(t) - \mathbf{y}(s)\|_p \\ &\leq C_1 |t-s|^\beta. \end{aligned} \tag{3.54}$$

Thus, the unique mild solutions to (3.36) satisfy $\mathbf{u} \in C([t_0, T^*[; [L^p(\Omega)]^m) \cap C^1([t_0, T^*[; [L^p(\Omega)]^m)$ and are therefore strong solutions to (3.4) according to Definition 3.3.3. See also Pazy [123, p. 109] for a definition of a strong solution.

$L^\infty(\Omega)$ initial data for the mollified problem

Each of the assertions in Theorem 3.3.4 follows whenever

$$\mathbf{u}_0 \in [\mathcal{D}(\mathbf{B}_p^\alpha)]^m.$$

Suppose now that $\mathbf{u}_0 \in [L^\infty(\Omega)]^m$ and let $\mathbf{u}_0^k$ be a sequence in $[\mathcal{D}(\mathbf{B}_p^\alpha)]^m$ such that $\mathbf{u}_0^k \geq 0$ and

$$\|\mathbf{u}_0^k - \mathbf{u}_0\|_p \to 0 \ \text{ as } \ k \to \infty.$$

Using (3.36) and the properties of $\mathbf{B}_p^\alpha$ stated in Lemma 3.3.6, it follows that

$$\begin{aligned} \|\mathbf{B}_p^\beta \mathbf{u}^k(t)\|_p \leq & C_\beta (t-t_0)^{-\beta} \|\mathbf{u}_0^k\|_p + \int_{t_0}^{t} C_\beta (t-s)^{-\beta} \|\mathbf{F}(\mathbf{u}^k(s))\|_p\, ds, \\ \leq & C_\beta (t-t_0)^{-\beta} \|\mathbf{u}_0^k\|_p + \int_{t_0}^{t} C_\beta (t-s)^{-\beta}\, ds \cdot \sup_{t\in[0,T^*)} \|\mathbf{F}(\mathbf{u}^k(t))\|_p, \\ \leq & C_\beta (t-t_0)^{-\beta} \|\mathbf{u}_0^k\|_p + C(t-t_0)^{-\beta} \left(\frac{t-t_0}{1-\beta}\right), \end{aligned}$$

for all $t \in [t_0, T_k^*[$ and for all $k \geq 1$. From these estimates one can deduce the existence of $\bar{C}_\beta$ such that

$$\|\mathbf{B}_p^\beta \mathbf{u}^k(t)\|_p \leq \bar{C}_\beta (t - t_0)^{-\beta} \quad \text{for all } t \in [t_0, t_1],\ k \geq 1 \text{ and } \alpha \leq \beta < 1. \tag{3.55}$$

Using (3.39), one can deduce a uniform bound on $\|\mathbf{u}^k(t)\|$. According to Lemmas 6 and 7 in Lightbourne and Martin [101], the family $\{\mathbf{u}^k(t) : k \geq 1\}$ is uniformly equicontinuous on $[t_0, t_1]$ and the family $\{\mathbf{B}_p^\beta \mathbf{u}^k(t) : k \geq 1\}$ is uniformly equicontinuous on $[t_0, t_1]$. Because of the compact embedding of $\mathcal{D}(\mathbf{B}_p^\alpha)$ in $\mathcal{D}(\mathbf{B}_p^\beta)$ and the compactness of $\mathbf{S}_p$, it follows by Arzela-Ascoli theorem that there exists a subsequence

$$\lim_{k \to \infty} \|\mathbf{u}^k(t) - \mathbf{u}(t)\|_p = 0 \quad \text{for } t \in [t_0, t_1], \tag{3.56}$$

and that $\mathbf{u}$ is a solution to (3.36) on $t \in [t_0, t_1]$ with $\mathbf{u}(t) \in [\mathcal{D}(\mathbf{B}_p^\alpha)]^m$ for $t_0 < t \leq t_1$. We remark that the solution in (3.56) corresponds to the mollified $\mathbf{f}$ which we denote by $\mathbf{u}^\epsilon$. Therefore using (3.36), we have

$$\begin{aligned}
\lim_{k \to 0} \mathbf{u}^k(t) &= \lim_{k \to 0} \left[\mathbf{S}_p(t - t_0)\mathbf{u}_0^k + \int_{t_0}^t \mathbf{S}_p(t - s)\mathbf{F}(\mathbf{u}^k(s))\, ds \right], \\
\mathbf{u}^\epsilon(t) &= \mathbf{S}_p(t - t_0)\mathbf{u}_0 + \int_{t_0}^t \lim_{k \to 0} \left[\mathbf{S}_p(t - s)\mathbf{F}(\mathbf{u}^k(s))\, ds \right], \\
&= \mathbf{S}_p(t - t_0)\mathbf{u}_0 + \int_{t_0}^t \mathbf{S}_p(t - s)\mathbf{F}^\epsilon(\mathbf{u}(s))\, ds. \qquad (3.57)
\end{aligned}$$

Solution for the discontinuous reaction terms

Due to the uniform convergence in (3.56), the limit function $\mathbf{u}^\epsilon(t)$ must satisfy the bound in (3.55). Also due to the uniform equicontinuity of $\mathbf{u}^\epsilon$, we have by Arzela-Ascoli theorem

$$\lim_{\epsilon \to 0} \|\mathbf{u}^\epsilon(t) - \mathbf{u}(t)\|_p = 0 \quad \text{for } t \in [t_0, t_1]. \tag{3.58}$$

Lemma A.0.17 from Appendix A with $\gamma = 1$ and (3.58) implies $\mathbf{F}^\epsilon(\mathbf{u}^\epsilon(s)) \to \mathbf{F}(\mathbf{u}(s))$ in $L^p(\Omega)$. Using the compactness of $\mathbf{S}_p$ and the properties of mollifiers stated in Lemma 3.3.2, we can pass to the limit using (3.36) and obtain

$$\begin{aligned}
\lim_{\epsilon \to 0} \mathbf{u}^\epsilon(t) &= \lim_{\epsilon \to 0} \left[\mathbf{S}_p(t - t_0)\mathbf{u}_0 + \int_{t_0}^t \mathbf{S}_p(t - s)\mathbf{F}^\epsilon(\mathbf{u}^\epsilon(s))\, ds \right], \\
\mathbf{u}(t) &= \mathbf{S}_p(t - t_0)\mathbf{u}_0 + \int_{t_0}^t \lim_{\epsilon \to 0} \left[\mathbf{S}_p(t - s)\mathbf{F}^\epsilon(\mathbf{u}^\epsilon(s))\, ds \right], \\
&= \mathbf{S}_p(t - t_0)\mathbf{u}_0 + \int_{t_0}^t \mathbf{S}_p(t - s)\mathbf{F}(\mathbf{u}(s))\, ds \quad a.e.\,. \qquad (3.59)
\end{aligned}$$

By replacing $[t_0, T^*[$ with $[t_1, T^*[$ and $\mathbf{u}_0$ with $\mathbf{u}(t_1)$ and using the results already established when $\mathbf{u}_0 \in [\mathcal{D}(\mathbf{B}_p^\alpha)]^m$, Theorem 3.3.4 follows. □

Remark 3.3.7. Since the $\mathbf{f}^\epsilon$ satisfy the condition of Assumption (F) in Pazy [123, p. 196], it follows that $t \to \mathbf{F}(\mathbf{z}(t))$ is locally Hölder continuous on $]t_0, T^*]$. In this case, the unique solution of (3.36) is a classical solution to (3.4) on $]t_0, T^*]$, see e.g., Rothe [138, p. 118].

3.4 Invariant regions and global existence

In this section we consider the cases under which invariant regions containing the solution can be constructed. The application of invariant regions to systems of reaction-diffusion equations can be found in Smoller [147]. Global existence results for system (3.4) where $\mathbf{f} : \mathbb{R}^m \times \mathbb{R}^m$ is locally Lipschitz and satisfy Lyapunov-type condition can be found in [109, 110, 67]. More recently, Pierre [126] has proved global existence for system (3.4) using L^p-estimates obtained by duality. The results in the two approaches above are for $m \times m$ systems with the so-called *triangular* structure, which means essentially that $f_1, f_1 + f_2, f_1 + f_2 + f_3, \dots$ are all bounded above by a linear function of the u_i.

As mentioned in Section 3.3, the assumptions (H1)-(H3) are generally not sufficient to ensure that solutions to (3.4) exist for all $t \geq 0$. Here, we give sufficient conditions guaranteeing that $T^* = \infty$ in Theorem 3.3.4. We achieve this by establishing a result on the uniform boundedness of solutions on $[0, \infty[\times \Omega$ using invariant sets.

Theorem 3.4.1. *Choose $\rho > 0$ arbitrarily large and define the following constants*

$$\tau := \rho + \frac{1}{\kappa}\left(\frac{\rho^2}{K_d^2 + \rho^2}\right), \qquad \eta_s := \frac{B_s \rho}{\rho + k_{b,s}^-}, \quad \text{and} \quad \eta_m := \frac{B_m \rho}{\rho + k_{b,m}^-}. \tag{3.60}$$

Then the region Σ defined by

$$\Sigma := \{(c, E, b_s, b_m) \in [0, \rho] \times [0, \tau] \times [0, \eta_s] \times [0, \eta_m]\} \tag{3.61}$$

is invariant with respect to (3.12). *This establishes uniform L^∞-bounds on the solutions on* $[0, \infty[\times \Omega$ *implying that $T^* = \infty$ in* (3.19).

Proof of Theorem 3.4.1.
From (3.12), consider the function $F(c, E, b_m, b_s) : \mathbb{R}^4 \to \mathbb{R}^4$ defined by

$$\mathbf{F}(c, E, b_m, b_s) = \begin{bmatrix} \kappa(E - c) - \frac{c^2}{K_d^2 + c^2} - (B_s - b_s + B_m - b_m)c + k_{b,s}^- b_s + k_{b,m}^- b_m \\ -\gamma(\kappa(E - c) - \frac{c^2}{K_d^2 + c^2}) \\ \gamma_{b,m}((B_m - b_m)c - k_{b,m}^- b_m) \\ \gamma_{b,s}((B_s - b_s)c - k_{b,s}^- b_s) \end{bmatrix}. \tag{3.62}$$

We use a variant of the technique postulated by Smoller [147, Theorems 14.7 and 14.11] to prove the following inequalities, which are sufficient to establish global existence and boundedness for (3.12) ,

$$\begin{aligned} F_1(0,E,b_m,b_s) &\geq 0; \qquad & F_1(\rho,E,b_m,b_s) &\leq 0,\\ F_2(c,0,b_m,b_s) &\geq 0; \qquad & F_2(c,\tau,b_m,b_s) &\leq 0,\\ F_3(c,E,0,b_s) &\geq 0; \qquad & F_3(c,E,\eta_m,b_s) &\leq 0,\\ F_4(c,E,b_m,0) &\geq 0; \qquad & F_4(c,E,b_m,\eta_s) &\leq 0. \end{aligned}$$

The inequalities on the left column follow from the quasi-positivity property proved already in (3.14). We now turn to the top boundaries of each of the variables defined in Σ. Using the first equation in (3.62) and the definitions of ρ, τ, η_m, and η_s given in (3.60), we have

$$\begin{aligned} F_1(\rho,E,b_m,b_s) =&\kappa E-\kappa\tau-[(B_s-b_s)\rho-k^-_{b,s}b_s+(B_m-b_m)\rho-k^-_{b,m}b_m],\\ \leq&\kappa(E-\tau)-[(B_s-\eta_s)\rho-k^-_{b,s}\eta_s+(B_m-\eta_m)\rho-k^-_{b,m}\eta_m],\\ =&\kappa(E-\tau)-\left(B_s-\frac{B_s\rho}{\rho+k^-_{b,s}}\right)\rho-k^-_{b,s}\left(\frac{B_s\rho}{\rho+k^-_{b,s}}\right)+\left(B_m-\frac{B_m\rho}{\rho+k^-_{b,m}}\right)\rho-k^-_{b,m}\left(\frac{B_m\rho}{\rho+k^-_{b,m}}\right),\\ =&\kappa(E-\tau)-B_s\left(\frac{k^-_{b,s}}{\rho+k^-_{b,s}}\right)\rho-\frac{k^-_{b,s}B_s\rho}{\rho+k^-_{b,s}}+B_m\left(\frac{k^-_{b,m}}{\rho+k^-_{b,m}}\right)\rho-\frac{k^-_{b,m}B_m\rho}{\rho+k^-_{b,m}},\\ =&\kappa(E-\tau)\leq 0 \quad \text{if we choose} \quad E\leq\tau. \end{aligned}$$

Similarly, for $c \leq \rho$, we have

$$\begin{aligned} F_2(c,\tau,b_m,b_s) =&-\gamma\left(\kappa\tau-\kappa c-\frac{c^2}{K_d^2+c^2}\right),\\ =&-\gamma\left(\kappa(\rho-c)+\frac{\rho^2}{K_d^2+\rho^2}-\frac{c^2}{K_d^2+c^2}\right),\\ &\leq 0. \end{aligned}$$

Next, we have

$$\begin{aligned} F_3(c,E,\eta_m,b_s) =&\gamma_{b,m}((B_m-\eta_m)c-k^-_{b,m}\eta_m),\\ =&\gamma_{b,m}\left((B_m-\frac{B_m\rho}{\rho+k^-_{b,m}})c-\frac{k^-_{b,m}B_m\rho}{\rho+k^-_{b,m}}\right),\\ =&\gamma_{b,m}\left(\frac{k^-_{b,m}B_m}{\rho+k^-_{b,m}}(c-\rho)\right),\\ &\leq 0 \quad \text{if} \quad c\leq\rho. \end{aligned}$$

Finally, if $c \leq \rho$, then

$$\begin{aligned}
F_4(c, E, b_m, \eta_s) =& \gamma_{b,s}((B_s - \eta_s)c - k_{b,s}^{-}\eta_s), \\
=& \gamma_{b,s}\left((B_s - \frac{B_s\rho}{\rho + k_{b,s}^{-}})c - \frac{k_{b,s}^{-}B_s\rho}{\rho + k_{b,s}^{-}}\right), \\
=& \gamma_{b,s}\left(\frac{k_{b,s}^{-}B_s}{\rho + k_{b,s}^{-}}(c - \rho)\right), \\
\leq& \, 0.
\end{aligned}$$

☐

This also proves that if we start with non-negative data, the solution remains non-negative for all time.

Chapter 4

Discretization

4.1 Aims and Outline

Now that we have established existence and uniqueness of global solutions to the model equations (3.2), we turn to the numerical approximation of solutions to the system. In this chapter we propose and describe numerical methods to approximate the solution to the model equations (3.2).

The layout of the remainder of this Chapter is as follows: We start with Section 4.2 introducing (very briefly) some background on numerical methods to approximate partial differential equations (PDEs). In Section 4.3 we give a brief historical perspective of the Discontinuous Galerkin (DG) methods. In Section 4.4 we present the semidiscrete DG schemes for the spatial discretization of elliptic problems. Here, we define our notations, function spaces, state our model problem together with the necessary assumptions that we make as well as assembly and implementation of matrices that result from DG discretizations. In Section 4.5, we provide the time discretization schemes that gives the fully discrete DG schemes employed in our numerical simulations. In Section 4.6 we briefly present the methods used for the solution of algebraic equations. Finally, in Section 4.7 we summarize the domain decomposition methods employed in our parallel implementations.

4.2 Background

In general there is to date no systematic way of constructing exact analytical solutions to nonlinear PDEs, which are usually of most relevance in modelling applications. To gain insight into the solutions of these problems, a *numerical* or *computational* approximation of the solution is therefore desired. The basic idea of constructing a numerical approximation to a continuous problem is to discretise the problem and then to solve the resulting discrete problem computationally.

	Complex geometries	High-order accuracy and *hp*-adaptivity	Explicit semi-discrete form	Conservation laws	Elliptical problems
FDM	×	✓	✓	✓	✓
FVM	✓	×	✓	✓	(✓)
FEM	✓	✓	×	(✓)	✓
DG	✓	✓	✓	✓	(✓)

Table 4.1: Summary of generic properties of the most widely used methods for discretizing PDEs. Table from Hesthaven and Warburton [82]

Many numerical methods have been proposed for the approximation of partial differential equations. An example is the spectral method, see Orszag and Patterson [121], where we represent the solution of a PDE with a Fourier series which we then approximate often using the fast Fourier transform. Other widely used numerical methods for the approximation of PDEs are finite difference methods, finite volume methods and finite element methods. In all of these methods, the approximate solution is calculated on a partioned (meshed) geometry. In a finite difference method we seek to approximate the solutions to a PDE by replacing the partial derivatives with finite difference (difference quotient) operators, see e.g., Morton and Mayers [111]. In a finite volume (FV) method we use the divergence theorem to express volume integral (of divergence) terms over elements (volumes) of the mesh as surface integrals (fluxes over the volume edges), see e.g., Versteeg and Malalasekera [157]. In a finite element method (FEM) we seek to approximate solutions to PDEs given in variational form, using a Galerkin procedure that consists of looking for approximate solutions in an appropriate finite dimensional space rather than the infinite dimensional space inhabited by the solution of the variational problem, Braess [33].

We will consider the Discontinuous Galerkin (DG) methods which combine features of the finite element and the finite volume framework. The DG method is based on a totally discontinuous finite element space and has many advantageous properties. Due to the missing continuity constraint of the basis functions, its use with non-conforming unstructured grids is staight forward and allows for easy adaptation in the polynomial order. For flow problems and problems with discontinuities, an important property of the DG discretization is its element-wise mass conservation. DG methods also have compact stencils and can be efficiently implemented in parallel. Their main drawback is higher computational costs with respect to stabilized FE or FV on a fixed mesh. An assessment of the general properties of some classical numerical methods compared to the DG method are given in Table 4.1. A ✓ represents success, while × indicates a short-coming in the method. Finally, a (✓) reflects that the method, with modifications, is capable of solving such problems but remains a less natural choice.

The problems we are considering are parabolic systems of PDEs which admit a variational form but may be posed on complex geometries. As is common in most numerical methods for time-dependent problems, we proceed by splitting up the spatial and temporal discretisation. We apply the DG method for the spatial approximation and a finite difference method for the temporal approximation.

4.3 A brief historical perspective of DG methods

DG methods can be viewed as finite element methods allowing for discontinuities in the discrete trial and test spaces. Localizing test functions to single mesh elements and introducing numerical fluxes at interfaces, they can also be viewed as finite volume methods in which the approximate solution is represented on each mesh element by a polynomial function and not only by a constant function. From a practical viewpoint, working with discontinuous discrete spaces leads to compact discretization stencils and, at the same time, offers a substantial amount of flexibility, making the approach appealing for multi-domain and multi-physics simulations where high accuracy is required, see e.g., Di Pietro and Ern [129, p. V]. Their compact formulation can be applied near boundaries without special treatment, which greatly increases the robustness and accuracy of any boundary condition implementation.

Although DG methods have existed in various forms for more than 30 years, they have experienced a vigorous development only over the last decade, as illustrated in Figure 4.1. The first DG method to approximate first-order PDEs has been introduced by Reed and Hill in 1973 [132] in the context of steady neutron transport, while the first analysis for steady first-order PDEs was performed by Lesaint and Raviart in 1974 [99, 100]. The error estimate was improved by Johnson and Pitkäranta in 1986 [90] who established an order of convergence in the L^2-norm of $(k + \frac{1}{2})$ if polynomials of degree k are used and the exact solution is smooth enough. Few years later, the method was further developed by Caussignac and Touzani [39, 38] to approximate the three-dimensional boundary-layer equations for incompressible steady fluid flows. At around the same time, DG methods were extended to time-dependent hyperbolic PDEs by Chavent and Cockburn [40] using the forward Euler scheme for time discretization together with limiters. The order of accuracy was improved by Cockburn and Shu [45, 46] using explicit Runge-Kutta schemes for time discretization, while a convergence proof to the entropy solution was obtained by Jaffré et al. [89]. Extensions are discussed in a series of papers by Cockburn, Shu, and coworkers, see e.g., [42, 44, 48].

For PDEs with diffusion, DG methods originated from the work of Nitsche on boundary-penalty methods in the early 1970s [117, 118] and the use of Interior Penalty (IP) techniques to weakly enforce continuity conditions imposed on the solution or its derivatives across interfaces, as in the work of Babuška [11], Babuška and Zlámal [12], Douglas and Dupont [91], Baker [13], Wheeler [160], and Arnold

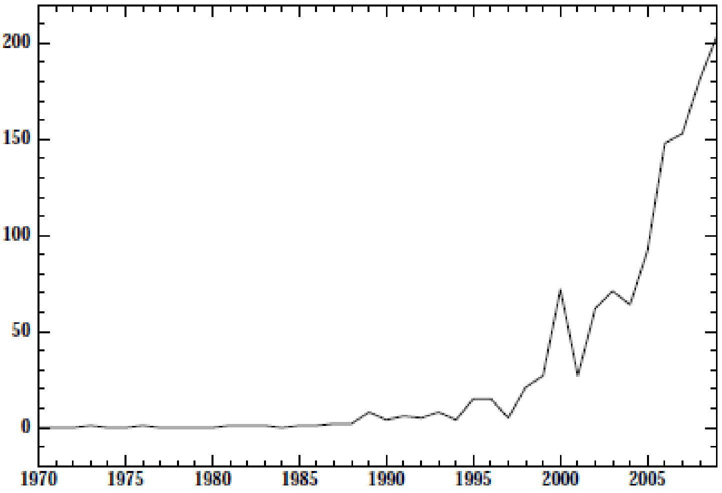

Figure 4.1: DG-related publications per year: Figure from Di Pietro and Ern [129, p. VI]

[8]. This latter work constitutes a milestone in the development of IP DG methods. In the late 1990s, following an approach more closely related to hyperbolic problems, DG methods were formulated using numerical fluxes by considering the mixed formulation of the diffusion term. Examples include the work of Bassi and Rebay [17] on the compressible Navier-Stokes equations and that of Cockburn and Shu [47] on convection-diffusion systems, leading to a new thrust in the development of DG methods. A unified analysis of DG methods for the Poisson problem can be found in the work of Arnold, Brezzi, Cockburn, and Marini [9], while a unified analysis encompassing both diffusive and first-order PDEs in the framework of Friedrichs' systems has been derived by Ern and Guermond [58, 59, 60]. Not mentioned in [9] are the recent compact discontinuous Galerkin(CDG) methods introduced in [124, 34]. In this thesis, we consider the interior penalty methods based on weighted averages (WIPG) recently introduced in [61, 129]. This method is more robust in handling heterogeneous diffusion, i.e., where the diffusion coefficients takes locally small values leading to reaction dominated regimes, which suits our model well.

4.4 Numerical methods

4.4.1 Mathematical notations and function spaces

The process of spatial discretization by the DG method is based on the discrete representation of a weak integral form of the partial differential equations to be solved. The formulation and subsequent discretization of such an integral form requires the definition of some function spaces and associated norms. Standard books on mathematical concepts such as, for instance, Adams [1], provide a detailed exposition of the mathematical concepts, which are the basis of DG discretization.

Consider a spatial domain $\Omega \subset \mathbb{R}^d$ with space dimension $d \geq 1$. The domain Ω is a bounded, connected, open subset of $\mathbb{R}^d$ with Lipschitz boundary $\partial\Omega$. We shall use the notation

$$f : \bar{\Omega} \to \mathbb{R}$$

to state that for each spatial point $\mathbf{x} \in \bar{\Omega}$, $f(\mathbf{x}) \in \mathbb{R}$. The set $\bar{\Omega}$ denotes the closure of Ω, that is $\bar{\Omega} = \Omega \cup \partial\Omega$.

Definition 4.4.1. A function $f : \bar{\Omega} \to \mathbb{R}$ is said to be of class $C^m(\Omega)$ if all of its derivatives on Ω up to order m exist and are continuous functions.

Definition 4.4.2. The support of a continuous function v defined on $\mathbb{R}^d$ is the closure of the set of points at which the function is not equal to zero. If it is bounded and included in the interior of the domain Ω, then v is said to have compact support in Ω.

We consider functions $v : \Omega \to \mathbb{R}$ that are Lebesgue measurable and we denote by $\int_\Omega v$ the Lebesgue integral of v over Ω. Let $1 \leq p \leq \infty$ be a real number. We set

$$\|v\|_{L^p(\Omega)} = \left(\int_\Omega |v|^p \right)^{1/p} \qquad 1 \leq p < \infty.$$

and

$$\begin{aligned} \|v\|_{L^\infty(\Omega)} &:= \text{sup ess}\,\{|v(x)| \text{ for a.e. } x \in \Omega\} \\ &= \inf\{M > 0 : |v(x)| \leq M \text{ for a.e. } x \in \Omega\}. \end{aligned}$$

We define the *Lebesgue space*

$$L^p(\Omega) := \{v \text{ Lebesgue measurable} : \|v\|_{L^p(\Omega)} < \infty\}.$$

Equipped with the norm $\|\cdot\|_{L^p(\Omega)}$, $L^p(\Omega)$ is a Banach space for all $1 \leq p \leq \infty$, see e.g., Evans [62, p. 249]. Moreover for all $1 \leq p < \infty$, the space $C_0^\infty(\Omega)$ spanned by infinitely differentiable functions with compact support in Ω is dense in $L^p(\Omega)$. In the particular case $p = 2$, $L^2(\Omega)$ is a real Hilbert space when equipped with the scalar product

$$(v, w)_{L^2(\Omega)} = \int_\Omega vw.$$

Definition 4.4.3. If $\alpha = (\alpha_1, \dots, \alpha_d) \in \mathbb{N}_0^d$ is a d-tuple of nonnegative integers α_j, we call α a *multi-index* and denote by x^α the monomial $x_1^{\alpha_1}, \dots, x_d^{\alpha_d}$. A multi-index has the *degree* $|\alpha| = \sum_{j=1}^d \alpha_j$. We define the distributional derivative $D^\alpha v$ by

$$D^\alpha v = \partial_{x1}^{\alpha_1} \dots \partial_{xd}^{\alpha_d} := \frac{\partial^{|\alpha|} v}{\partial^{\alpha_1} x_1 \dots \partial^{\alpha_d} x_d}.$$

Next we give a particular class of Sobolev spaces, those of square integrable functions and derivatives.

Definition 4.4.4. For any nonnegative integer m, we define the *Sobolev space* $H^m(\Omega)$ using multi-index notation

$$H^m(\Omega) = \{v \in L^2(\Omega) \,|\, D^\alpha v \in L^2(\Omega) \quad \text{for all} \;\; |\alpha| \leq m\}.$$

Therefore, $H^m(\Omega)$ consists of square integrable functions all of whose derivatives of order up to m are also square integrable. $H^m(\Omega)$ is equipped with norm and seminorm

$$\|v\|_{H^m(\Omega)} = \left(\int_\Omega \sum_{|\alpha| \leq m} |D^\alpha v|^2 \, dx \right)^{1/2}, \qquad |v|_{H^m(\Omega)} = \left(\int_\Omega \sum_{|\alpha| = m} |D^\alpha v|^2 \, dx \right)^{1/2}.$$

Note that $L^2(\Omega)$ is, in fact, a Sobolev space, $H^0(\Omega) = L^2(\Omega)$, while the Sobolev space for $m = 1$ is defined by

$$H^1(\Omega) = \{v \in L^2(\Omega) \,|\, \frac{\partial v}{\partial x_i} \in L^2(\Omega) \quad i = 1, \dots, d\}.$$

This space is equipped with the inner product

$$\langle v, w \rangle_{H^1(\Omega)} = \int_\Omega \left(vw + \sum_{i=1}^d \frac{\partial v}{\partial x_i} \frac{\partial w}{\partial x_i} \right) d\Omega,$$

and its induced norm is

$$\|v\|_{H^1(\Omega)} = \sqrt{\langle v, w \rangle_{H^1(\Omega)}}\,.$$

We also mention the subspace

$$H_0^1(\Omega) = \{v \in H^1(\Omega) \,|\, v = 0 \quad \text{on} \;\; \partial\Omega\},$$

the elements of which posses a square integrable first derivative over the domain and whose trace vanishes on its boundary $\partial\Omega$. Moreover, its inner product and norm coincide with those of $H^1(\Omega)$.

Boundary values of functions in the Sobolev space $W^{1,p}(\Omega)$ can be given a meaning (at least) in $L^p(\Omega)$. More precisely, see e.g., Brenner and Scott [35, Chap. 1], for all $1 \leq p \leq \infty$, there is a constant C such that

$$\|v\|_{L^p(\partial\Omega)} \leq C\|v\|_{L^p(\Omega)}^{1-1/p}\|v\|_{W^{1,p}(\Omega)}^{1/p} \qquad \text{for all} \quad v \in W^{1,p}(\Omega). \tag{4.1}$$

In particular, for $p = 2$, we obtain

$$\|v\|_{L^2(\partial\Omega)} \leq C\|v\|_{L^2(\Omega)}^{1/2}\|v\|_{H^1(\Omega)}^{1/2} \qquad \text{for all} \quad v \in H^1(\Omega). \tag{4.2}$$

The bounds (4.1) and (4.1) are called *continuous trace inequalities*, see Di Pietro and Ern [129, p. 7].

Definition 4.4.5. Let $\mathcal{T}_h$ be a mesh of the domain Ω. For any mesh element $T \in \mathcal{T}_h$, the Sobolev space $H^m(T)$ can be defined by replacing Ω by T. We then define *broken Sobolev spaces*

$$H^m(\mathcal{T}_h) := \left\{v \in L^2(\Omega) \,|\, \forall T \in \mathcal{T}_h, \quad v|_T \in H^m(T)\right\}$$

where $m \geq 0$ is an integer.

In the context of broken Sobolev spaces, the continuous trace inequality (4.1) can be used to infer that, for all $v \in W^{1,p}(\mathcal{T}_h)$ and all $T \in \mathcal{T}_h$,

$$\|v\|_{L^p(\partial T)} \leq C\|v\|_{L^p(T)}^{1-1/p}\|v\|_{W^{1,p}(T)}^{1/p}, \tag{4.3}$$

while for $p = 2$, we obtain, for all $v \in H^1(\mathcal{T}_h)$ and all $T \in \mathcal{T}_h$,

$$\|v\|_{L^2(\partial T)} \leq C\|v\|_{L^2(T)}^{1/2}\|v\|_{H^1(T)}^{1/2}. \tag{4.4}$$

Consequently, it is implicitly understood that expressions such as $\|v\|_{L^2(\partial T)}$ for a mesh face of a given element $T \in \mathcal{T}_h$ should be evaluated using the restriction of v to T. Continuous trace inequalities such as (4.3) or (4.4) are important in the context of DG methods to give a meaning to the traces of the exact solution or of its (normal) gradient on mesh faces, see [129, p. 14].

It is natural to define a broken gradient operator acting on the broken Sobolev space $W^{1,p}(\mathcal{T}_h)$. In particular, this operator also acts on broken polynomial spaces.

Definition 4.4.6. The *broken gradient* $\nabla_h : W^{1,p}(\mathcal{T}_h) \to [L^p(\Omega)]^d$ is defined such that, for all $v \in W^{1,p}(\mathcal{T}_h)$, and for all $T \in \mathcal{T}_h$,

$$(\nabla_h)|T := \nabla(v|T).$$

It is important to observe that the usual Sobolev spaces are subspaces of the broken Sobolev spaces, and that on the usual Sobolev spaces, the broken gradient coincides with the distributional gradient, see [129, p. 14].

4.4.2 The basic aspects of the DG method

In this subsection, we closely follow Di Pietro and Ern [129] and present the main ingredients to build finite-dimensional function spaces to approximate PDEs using DG methods. The construction of such spaces hinges on discretizing the domain Ω, over which the PDE is posed, using a mesh and choosing a local functional behavior (e.g., polynomial) within each mesh element. This leads to broken polynomial spaces. This necessitates the use of broken Sobolev spaces and a broken gradient operator.

The domain Ω is assumed to be a polyhedron in $\mathbb{R}^d$. The advantage of this assumption is that polyhedra can be exactly covered by a mesh consisting of polyhedral elements. PDEs posed over domains with curved boundary can also be approximated by DG methods using, e.g., isoparametric finite elements to build the mesh near curved boundaries as described, e.g., by Ciarlet [41, p. 224] and Brenner and Scott [35, p. 117]. The *outward normal* to the boundary $\partial\Omega$ which is defined a.e. on $\partial\Omega$ is denoted by $\mathbf{n}$.

The first basic aspect is to discretize the domain Ω using a mesh. Various types of meshes can be considered. While simplicial meshes are quite convenient in the context of continuous finite elements, DG methods more easily accommodate general meshes, see [129, p. 9].

Definition 4.4.7. (Di Pietro and Ern [129, p. 9]).
A general mesh $\mathcal{T}$ of the domain Ω is a finite collection of disjoint polyhedra $\mathcal{T} = \{T\}$ forming a partition of Ω,

$$\bar{\Omega} = \bigcup_{T \in \mathcal{T}} \bar{T}.$$

Each $T \in \mathcal{T}$ is called a *mesh element*. If h_T denotes the *diameter* of T, then we define the *meshsize* as the real number

$$h := \max_{T \in \mathcal{T}} h_T.$$

In the sequel, we use the notation $\mathcal{T}_h$ for a mesh $\mathcal{T}$ with meshsize h. The *outward normal* to T a.e. on ∂T is defined as $\mathbf{n}_T$, [129, p. 9].

Definition 4.4.8. (Di Pietro and Ern [129, p. 9]).
Let $\mathcal{T}_h$ be a mesh of the domain Ω. We say that a closed subset F of $\bar{\Omega}$ is a *mesh face* if F has positive $(d-1)$-dimensional Hausdorff measure and if either one of the two following conditions is satisfied:

(i) There are distinct mesh elements T_1 and T_2 such that $F = \partial T_1 \cap \partial T_2$; in such a case, F is called an *interface.*

(ii) There is a $T \in \mathcal{T}_h$ such that $F = \partial T \cap \partial \Omega$ in such a case, F is called a *boundary face.*

Interfaces are collected in the set $\mathcal{F}_h^i$ and boundary faces are collected in the set $\mathcal{F}_h^b$. Henceforth, we set

$$\mathcal{F}_h := \mathcal{F}_h^i \cup \mathcal{F}_h^b.$$

Moreover, for any mesh element $T \in \mathcal{T}_h$, the set

$$\mathcal{F}_T := \{F \in \mathcal{F}_h \mid F \subset \partial T\}$$

collects the mesh faces composing the boundary of T. The maximum number of mesh faces composing the boundary of mesh elements is denoted by

$$N_\partial := \max_{T \in \mathcal{T}_h} \operatorname{card}(\mathcal{F}_T). \tag{4.5}$$

Finally, for any mesh face $F \in \mathcal{F}_h$, we define the set

$$\mathcal{T}_F := \{T \in \mathcal{T}_h \mid F \subset \partial T\} \tag{4.6}$$

and observe that $\mathcal{T}_F$ consists of two mesh elements if $F \in \mathcal{F}_h^i$ and of one mesh element if $F \in \mathcal{F}_h^b$.

Definition 4.4.9. (Di Pietro and Ern [129, p. 10]).
Let v be a scalar-valued function defined on Ω and assume that v is smooth enough to admit on all $F \in \mathcal{F}_h^i$ a possibly two-valued trace. This means that, for all $T \in \mathcal{T}_h$, the restriction $v|_T$ of v to the open set T can be defined up to the boundary ∂T. Then, for all $F \in \mathcal{F}_h^i$ and a.e. $x \in F$, the *average* of v is defined as

$$\{\!\!\{v\}\!\!\}_F(x) := \frac{1}{2}\left(v|_{T_1}(x) + v|_{T_2}(x)\right),$$

and the *jump* of v as

$$[\![v]\!]_F(x) := v|_{T_1}(x) - v|_{T_2}(x).$$

For simplicity, we will omit the subscript F and the variable x and simply write $\{\!\{v\}\!\}$ and $[\![v]\!]$.

Definition 4.4.10. (Di Pietro and Ern [129, p. 11]).
For all $F \in \mathcal{F}_h$ and a.e. $x \in F$, the *face unit normal* $\mathbf{n}_F$ to F at x is defined as

(i) $\mathbf{n}_{T_1}$, the unit normal to F at x pointing from T_1 to T_2 if $F \in \mathcal{F}_h^i$ with $F = \partial T_1 \cap \partial T_2$; the orientation of $\mathbf{n}_F$ is arbitrary depending on the choice of T_1 and T_2, see Figure 4.2.

(ii) $\mathbf{n}$, the unit outward normal to Ω if $F \in \mathcal{F}_h^b$.

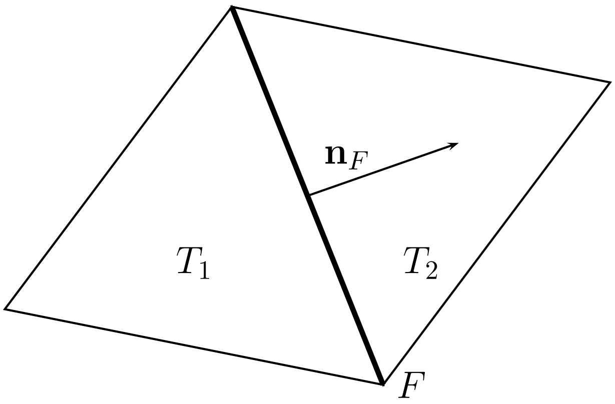

Figure 4.2: Notation for an interface. Figure from Di Pietro and Ern [129, p. 11].

Remark 4.4.11. Averages and jumps can also be defined for boundary faces. This is particularly useful when discretizing PDEs with diffusion. One possible definition is to set for a.e. $x \in F$ with $F \in \mathcal{F}_h^b$, $F = \partial T \cap \partial\Omega$, $\{\!\{v\}\!\}_F(x) = [\![v]\!]_F(x) := v|_T(x)$.

Having built a mesh of the domain Ω, the second step in the construction of discrete function spaces consists in choosing a certain functional behavior within each mesh element. The resulting spaces, consisting of piecewise polynomial functions, are termed *broken polynomial spaces.* Precisely, let $k \geq 0$ be an integer. We define the space of polynomials of d variables, of total degree at most k, as

$$\mathbb{P}_d^k := \left\{ p : \mathbb{R}^d \ni x \mapsto p(x) \in \mathbb{R} \,|\, \exists\, (\gamma_\alpha)_{\alpha \leq k} \text{ s.t. } p(x) = \sum_{|\alpha| \leq k} \gamma_\alpha x^\alpha \} \right\},$$

with the convention that, for $x = (x_1, \dots, x_d) \in \mathbb{R}^d$, $x^\alpha := \prod_{i=1}^d x_i^{\alpha_i}$. The dimension of the vector space $\mathbb{P}_d^k$ is

$$\dim(\mathbb{P}_d^k) = \binom{k+d}{k} = \frac{(k+d)!}{k!\, d!}. \tag{4.7}$$

We often consider the broken polynomial space

$$\mathbb{P}_d^k(\mathcal{T}_h) = \{v \in L^2(\Omega) : \text{for all} \quad T \in \mathcal{T}_h, \quad v|_T \in \mathbb{P}_d^k(T)\} \tag{4.8}$$

where $\mathbb{P}_d^k(T)$ is spanned by the restriction to T of polynomials in $\mathbb{P}_d^k$. It is clear that

$$\dim(\mathbb{P}_d^k(\mathcal{T}_h)) = \mathrm{card}((\mathcal{T}_h)) \times \dim(\mathbb{P}_d^k)$$

since the restriction of a function $v \in \mathbb{P}_d^k(\mathcal{T}_h)$ to each mesh element can be chosen independently of its restriction to other elements.

4.4.3 Model Problem

The aim of this subsection is to investigate the approximation of scalar PDEs with diffusion. As a first step, we consider the Poisson problem with homogeneous Dirichlet boundary condition

$$-\Delta u = f \quad \text{in } \Omega, \tag{4.9}$$
$$u = 0 \quad \text{on } \partial\Omega, \tag{4.10}$$

and source term $f \in L^2(\Omega)$. The weak formulation of (4.9) is classical:

$$\text{Find } u \in V \text{ s.t } a(u, v) = \int_\Omega fv \quad \text{for all } v \in V, \tag{4.11}$$

with energy space $V = H_0^1(\Omega) := \{v \in H^1(\Omega) : v|_{\partial\Omega} = 0\}$ and bilinear form

$$a(u, v) := \int_\Omega \nabla u \cdot \nabla v. \tag{4.12}$$

Recalling the Poincaré inequality, see e.g., Evans [62, p. 265] stating that there is a constant $C(\Omega)$ such that, for all $v \in H_0^1(\Omega)$,

$$\|v\|_{L^2(\Omega)} \leq C\|\nabla v\|_{[L^2(\Omega)]^d}, \tag{4.13}$$

we infer that the bilinear form a is coercive on V . Therefore, owing to the Lax-Milgram Lemma, the weak problem (4.11) is well-posed.

The PDE (4.9) can be rewritten in mixed form as a system of first-order PDEs:

$$\sigma + \nabla u = 0 \quad \text{in } \Omega, \tag{4.14}$$
$$\nabla \cdot \sigma = f \quad \text{in } \Omega, \tag{4.15}$$

In the context of the mixed formulation (4.14)-(4.15), the scalar-valued function u is termed the *potential* and the vector-valued function $\sigma := -\nabla u$ is termed the *diffusive flux.* The derivation of DG methods to approximate the model problems (4.9)-(4.10) on a given mesh $\mathcal{T}_h$ hinges on the fact that the jumps of the potential and of the normal component of the diffusive flux vanish across interfaces.

Since the potential u is in the energy space V, we infer that, for all $T \in \mathcal{T}_h$ and all $F \in \mathcal{F}_T$, letting $u_T := u|_T$, the trace $u_T|_F$ is in $L^2(F)$. Furthermore, the diffusive flux σ is in the space $H(\mathrm{div};\Omega)$, see e.g., Di Pietro and Ern [129, Sect. 1.2.6] for a discussion of traces on mesh faces of the normal component of functions in $H(\mathrm{div};\Omega)$. In particular, under the regularity assumption $u \in W^{2,1}(\Omega)$, there holds $\sigma \in [W^{1,1}(\Omega)]^d$ so that, for all $T \in \mathcal{T}_h$ and all $F \in \mathcal{F}_T$, letting $\sigma_T := \sigma|_T$ and $\sigma_{\partial T} := \sigma_T \cdot \mathbf{n}_T$ on ∂T, the trace $\sigma_{\partial T}|_F$ is in $L^1(F)$. This trace is in $L^2(F)$ under the stronger regularity assumption $u \in H^2(\Omega)$. Actually, the assumption $u \in H^{3/2+\epsilon}(\Omega)$, $\epsilon > 0$, is sufficient. We now examine the jumps of the potential and of the normal component of the diffusive flux in the Lemma below, a proof can be found in [129, p. 122].

Lemma 4.4.12. *Assume $u \in V \cap W^{2,1}(\Omega)$. Then, there holds*

$$[\![v]\!] = 0 \quad \text{for all} \quad F \in \mathcal{F}_h, \tag{4.16}$$

$$[\![v]\!] \cdot \mathbf{n}_F = 0 \quad \text{for all} \quad F \in \mathcal{F}_h^i. \tag{4.17}$$

We now use the DG method of Symmetric Interior Penalty (SIP) introduced by Arnold [8] to approximate the solution of the model problem (4.11) in the broken polynomial space $\mathbb{P}_d^k(\mathcal{T}_h)$ defined in (4.8). We set

$$V_h := \mathbb{P}_d^k(\mathcal{T}_h)$$

with polynomial degree $k \geq 1$ and $\mathcal{T}_h$ belonging to an admissible mesh sequence. For simplicity, we enforce a somewhat strong regularity assumption on the exact solution.

Assumption 4.4.13. *We assume that the exact solution u is such that*

$$u \in V_* := V \cap H^2(\Omega),$$

and set $V_{*h} := V_* + V_h$.

To derive a suitable discrete bilinear form that satisfies the consistency requirement and enjoys discrete coercivity, we follow Di Pietro and Ern [129, Sect. 4.2]. In this formulation, a consistent term is added in order to recover the symmetry of the continuous problem at the discrete level. We set for all $(v, w_h) \in V_{*h} \times V_h$,

$$a_h^{(0)}(v, w_h) := \int_\Omega \nabla_h v \cdot \nabla_h w_h = \sum_{T \in \mathcal{T}_h} \int_T \nabla v \cdot \nabla w_h.$$

To examine the consistency requirement, see [129, Sect. 1.3.3], we integrate by parts on each mesh element to obtain

$$a_h^{(0)}(v, w_h) = -\sum_{T\in\mathcal{T}_h}\int_T (\Delta v)w_h + \sum_{T\in\mathcal{T}_h}\int_{\partial T}(\nabla v\cdot \mathbf{n}_T)w_h.$$

The second term on the right-hand side can be reformulated as a sum over mesh faces in the form

$$\sum_{T\in\mathcal{T}_h}\int_{\partial T}(\nabla v\cdot \mathbf{n}_T)w_h = \sum_{F\in\mathcal{F}_h^i}\int_F [\![(\nabla_h v)w_h]\!]\cdot \mathbf{n}_F + \sum_{F\in\mathcal{F}_h^b}\int_F(\nabla v\cdot\mathbf{n}_F)w_h,$$

since for all $F\in\mathcal{F}_h^i$ with $F=\partial T_1\cap\partial T_2, \mathbf{n}_F=\mathbf{n}_{T_1}=-\mathbf{n}_{T_2}$. Moreover,

$$[\![(\nabla_h v)w_h]\!] = \{\!\{\nabla_h v\}\!\}[\![w_h]\!] + [\![\nabla_h v]\!]\{\!\{w_h\}\!\},$$

since letting $a_i=(\nabla v)|_{T_i},\ b_i=w_h|_{T_i},\ i\in\{1,2\}$, yields

$$\begin{aligned}[\![(\nabla_h v)w_h]\!] &= a_1b_1-a_2b_2\\ &= \frac{1}{2}(a_1+a_2)(b_1-b_2)+(a_1-a_2)\frac{1}{2}(b_1+b_2)\\ &= \{\!\{\nabla_h v\}\!\}[\![w_h]\!] + [\![\nabla_h v]\!]\{\!\{w_h\}\!\}.\end{aligned}$$

As a result, and accounting for boundary faces using (4.11), yields

$$\sum_{T\in\mathcal{T}_h}\int_{\partial T}(\nabla v\cdot\mathbf{n}_T)w_h = \sum_{F\in\mathcal{F}_h}\int_F\{\!\{\nabla_h v\}\!\}\cdot\mathbf{n}_F[\![w_h]\!] + \sum_{F\in\mathcal{F}_h^i}\int_F[\![\nabla_h v]\!]\cdot\mathbf{n}_F\{\!\{w_h\}\!\}.$$

Hence

$$a_h^{(0)}(v,w_h) = -\sum_{T\in\mathcal{T}_h}\int_T(\Delta v)w_h + \sum_{F\in\mathcal{F}_h}\int_F\{\!\{\nabla_h v\}\!\}\cdot\mathbf{n}_F[\![w_h]\!] + \sum_{F\in\mathcal{F}_h^i}\int_F[\![\nabla_h v]\!]\cdot\mathbf{n}_F\{\!\{w_h\}\!\}. \tag{4.18}$$

To check consistency, we set $u=v$ in (4.18). A consequence of (4.17) is that, for all $w_h\in V_h$,

$$a_h^{(0)}(v,w_h) = \int_\Omega f w_h + \sum_{F\in\mathcal{F}_h}\int_F(\nabla u\cdot\mathbf{n}_F)[\![w_h]\!].$$

In order to match the consistency requirement in [129, Sect. 1.3.3], we modify $a_h^{(0)}(v,w_h)$ as follows: For all $(v,w_h)\in V_{*h}\times V_h$,

$$a_h^{(1)}(v,w_h) := \int_\Omega \nabla_h v\cdot\nabla_h w_h - \sum_{F\in\mathcal{F}_h}\int_F\{\!\{\nabla_h v\}\!\}\cdot\mathbf{n}_F[\![w_h]\!].$$

It is clear that $a_h^{(1)}$ is consistent i.e., for all $w_h \in V_h$,

$$a_h^{(1)}(u, w_h) = \int_\Omega f w_h.$$

A desirable property of the discrete bilinear form is to preserve the original symmetry of the exact bilinear form. Indeed, symmetry can simplify the solution of the resulting linear system and furthermore, it is a natural ingredient to derive optimal L^2-norm error estimates, see [129, Sect. 4.2.4]. We therefore set, for all $(v, w_h) \in V_{*h} \times V_h$,

$$a_h^{\mathrm{cs}}(v, w_h) = \int_\Omega \nabla_h v \cdot \nabla_h w_h - \sum_{F \in \mathcal{F}_h} \int_F (\{\!\{\nabla_h v\}\!\} \cdot \mathbf{n}_F [\![w_h]\!] + [\![v]\!] \{\!\{\nabla_h w_h\}\!\} \cdot \mathbf{n}_F), \tag{4.19}$$

so that $a_h^{\mathrm{cs}}(v, w_h)$ is symmetric on $V_h \times V_h$. The bilinear form $a_h^{\mathrm{cs}}(v, w_h)$ remains consistent owing to (4.16), where the superscript denotes the consistency and symmetry achieved. Equivalently, from (4.18), we have the expression

$$a_h^{\mathrm{cs}}(v, w_h) = -\sum_{T \in \mathcal{T}_h} \int_T (\Delta v) w_h + \sum_{F \in \mathcal{F}_h^i} \int_F [\![\nabla_h v]\!] \cdot \mathbf{n}_F \{\!\{w_h\}\!\} - \sum_{F \in \mathcal{F}_h} \int_F [\![v]\!] \{\!\{\nabla_h w_h\}\!\} \cdot \mathbf{n}_F. \tag{4.20}$$

The last requirement to match is discrete coercivity on the broken polynomial space V_h with respect to a suitable norm. The difficulty with the discrete bilinear form $a_h^{\mathrm{cs}}(v, w_h)$ defined by (4.19) is that, for all $v_h \in V_h$,

$$a_h^{\mathrm{cs}}(v_h, v_h) = \|\nabla_h v_h\|^2_{[L^2(\Omega)]^d} - 2 \sum_{F \in \mathcal{F}_h} \int_F \{\!\{\nabla_h v_h\}\!\} \cdot \mathbf{n}_F [\![v_h]\!],$$

and the second term on the right-hand side has no a priori sign so that, without adding a further term, there is no hope for discrete coercivity. To achieve discrete coercivity, we add to $a_h^{\mathrm{cs}}(v, w_h)$ a term penalizing interface and boundary jumps, namely we set, for all $(v, w_h) \in V_{*h} \times V_h$

$$a_h^{\mathrm{sip}}(v, w_h) := a_h^{\mathrm{cs}}(v, w_h) + s_h(v, w_h), \tag{4.21}$$

with the stabilization bilinear form

$$s_h(v, w_h) := \sum_{F \in \mathcal{F}_h} \frac{\eta}{h_F} \int_F [\![v]\!][\![w_h]\!], \tag{4.22}$$

where $\eta > 0$ is a user-dependent parameter and h_F a local length scale associated with the mesh face $F \in \mathcal{F}_h$. Observe that, owing to (4.16), adding the bilinear form

s_h to a_h^{cs} does not alter the consistency and symmetry achieved so far. Moreover, Lemma 4.12 in [129, p. 129] shows that, provided the penalty parameter η is large enough, the discrete bilinear form a_h^{sip} enjoys discrete coercivity on V_h.

Combining (4.21) with (4.22) yields, for all $(v, w_h) \in V_{*h} \times V_h$

$$\begin{aligned} a_h^{\mathrm{sip}}(v, w_h) = &\int_\Omega \nabla_h v \cdot \nabla_h w_h - \sum_{F\in\mathcal{F}_h} \int_F (\{\!\{\nabla_h v\}\!\} \cdot \mathbf{n}_F [\![w_h]\!] + [\![v]\!]\{\!\{\nabla_h w_h\}\!\} \cdot \mathbf{n}_F) \\ &+ \sum_{F\in\mathcal{F}_h} \frac{\eta}{h_F} \int_F [\![v]\!][\![w_h]\!], \end{aligned} \tag{4.23}$$

or, equivalently using (4.20)

$$\begin{aligned} a_h^{\mathrm{sip}}(v, w_h) = &-\sum_{T\in\mathcal{T}_h} \int_T (\Delta v) w_h + \sum_{F\in\mathcal{F}_h^i} \int_F [\![\nabla_h v]\!] \cdot \mathbf{n}_F \{\!\{w_h\}\!\} - \sum_{F\in\mathcal{F}_h} \int_F [\![v]\!]\{\!\{\nabla_h w_h\}\!\} \cdot \mathbf{n}_F \\ &+ \sum_{F\in\mathcal{F}_h} \frac{\eta}{h_F} \int_F [\![v]\!][\![w_h]\!]. \end{aligned} \tag{4.24}$$

The second, third, and fourth terms on the right-hand side of (4.23) are respectively called *consistency, symmetry*, and *penalty* terms. The discrete problem now is: Find $u_h \in V_h$ such that for all $v_h \in V_h$

$$a_h^{\mathrm{sip}}(u_h, v_h) = \int_\Omega f v_h. \tag{4.25}$$

For implementation purposes, we illustrate the elementary stencil associated with the SIP bilinear form in Figure 4.3. For all $T \in \mathcal{T}_h$ the stencil of the volume contribution is just the element T, while the stencil associated with the consistency, symmetry, and penalty terms consists of T and its neighbors in the sense of faces. The discrete problem (4.25), which was derived in the context of homogeneous Dirichlet boundary conditions, needs to be slightly modified when dealing with other boundary conditions. The modifications are designed so as to maintain consistency when the exact solution satisfies other boundary conditions. For instance, when (weakly) enforcing the nonhomogeneous Dirichlet boundary condition $u = g$ on $\partial\Omega$ with $g \in H^{1/2}(\partial\Omega)$, the discrete problem becomes: Find $u_h \in V_h$ such that for all $v_h \in V_h$

$$a_h^{\mathrm{sip}}(u_h, v_h) = l_h^D(g; v_h)$$

with a_h^{sip} still defined by (4.23) and the new right-hand side

$$l_h^D(g; v_h) := \int_\Omega f v_h - \int_{\partial\Omega} g \nabla_h v_h \cdot \mathbf{n} + \sum_{F\in\mathcal{F}_h^b} \frac{\eta}{h_F} \int_F g v_h.$$

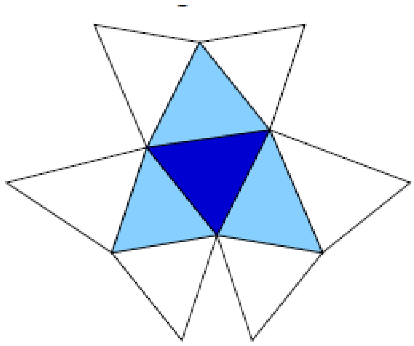

Figure 4.3: Example of stencil of an element $T \in \mathcal{T}_h$ when $\mathcal{T}_h$ is a matching triangular mesh; the mesh element T is highlighted in *dark blue*, and its three neighbors, which all belong to the stencil, are highlighted in *light blue*; the other triangles do not belong to the stencil

As a result, for the exact solution $u \in V_*$, $a_h^{\mathrm{sip}}(u, v_h) = l_h^D(g; v_h)$, for all $v_h \in V_h$. Furthermore, when (weakly) enforcing the Robin boundary condition $\gamma u + \nabla u \cdot \mathbf{n} = g$ on $\partial\Omega$ with $g \in L^2(\partial\Omega)$ and $\gamma \in L^\infty(\partial\Omega)$ such that γ is nonnegative a.e. on $\partial\Omega$, the discrete problem becomes: Find $u_h \in V_h$ such that for all $v_h \in V_h$

$$a_h^{\mathrm{R}}(u_h, v_h) = l_h^R(g; v_h)$$

where, for all $(v, w_h) \in V_{*h} \times V_h$,

$$\begin{aligned} a_h^{\mathrm{R}}(v, w_h) := & \int_\Omega \nabla_h v \cdot \nabla_h w_h - \sum_{F \in \mathcal{F}_h^i} \int_\Omega (\{\!\{\nabla_h v\}\!\} \cdot \mathbf{n}_F [\![w_h]\!] + [\![v]\!] \{\!\{\nabla_h w_h\}\!\} \cdot \mathbf{n}_F) \\ & + \sum_{F \in \mathcal{F}_h^i} \frac{\eta}{h_F} \int_F [\![v]\!][\![w_h]\!] + \sum_{F \in \mathcal{F}_h^b} \int_F \gamma v_h w_h, \end{aligned} \tag{4.26}$$

and

$$l_h^R(g; w_h) := \int_\Omega f w_h + \int_{\partial\Omega} g w_h.$$

As a result, for the exact solution $u \in V_*$, $a_h^{\mathrm{R}}(u, v_h) = l_h^R(g; v_h)$, for all $v_h \in V_h$. Moreover, we observe that, unlike in the Dirichlet case, the summations in the consistency and symmetry terms are restricted to interfaces. Finally, the case $\gamma \equiv 0$ corresponds to the Neumann problem. The SIP bilinear form unveiled in this section is coercive and bounded on V_h with respect to the suitable energy norm as depicted in [129, Ch. 4]. Moreover, the error estimate and convergence are optimal in the same norm with a convergence rate of order k if polynomials of degree k are used and the exact solution is smooth enough. Besides, if the exact solution $u \in H^{k+1}(\Omega)$, then we have the following convergence order in the L^2-norm

$$\|u - u_h\|_{L^2(\Omega)} \leq C_u h^{k+1},$$

where $C_u = C\|u\|_{H^{k+1}(\Omega)}$ and C is independent of h. For more details on the basic energy - error estimates, see Di Pietro and Ern [129, Ch. 4].

4.4.4 Choice of basis functions

The choice of basis functions can have a substantial impact on the performance and accuracy of a DG code. This is, in particular, the case when using polynomials with high degree. Various criteria can be adopted to select basis functions. Orthogonality and hierarchism are often considered in the context of modal basis functions, while ease of integral computation is often considered in the context of nodal basis functions.

For modal basis functions, a first possible criterion to select a high-degree polynomial basis is that it be orthogonal or nearly orthogonal with respect to an appropriate inner product. When the inner product corresponds to local matrices contributing to the global system, this ensures that their condition number does not increase too much as the polynomial degree k grows. Improving the condition number of local mass matrices is particularly relevant for high-order approximations. For instance, when using Lagrange polynomials of degree k associated with equispaced nodes in d space dimensions, the condition number of elemental mass matrices is known to grow as 4^{kd}, see Olsen and Douglas [120]. Also, the condition number of the global matrix has an important role in determining the numerical error in the solution, see, e.g., Quarteroni et al. [131].

A second important criterion which is often associated with orthogonality is that the basis be hierarchical, that is, the basis for a given polynomial degree k includes the bases for polynomial degrees less than k. This point is particularly relevant when one wishes to locally adapt, in space and/or in time, the polynomial degree according to some a posteriori regularity estimates, following the paradigm that, when the exact solution is locally smooth enough, increasing the polynomial degree generally pays off more in terms of error reduction than reducing the meshsize.

A different criterion for selecting basis functions is to make the computation of volume and face integrals as efficient as possible. While for linear problems with constant coefficients, exact volume and face integrations can be performed, quadratures are required in general. The principle of a quadrature is to approximate the integral of a generic function f over a domain Ω by a linear combination of the values of f at a set of nodes $\{\xi_n\}_{0\leq n\leq N}$ of Ω, i.e.,

$$\int_{\Omega} f(x) \simeq \sum_{n=0}^{N} \omega_n f(\xi_n).$$

The points $\{\xi_n\}_{0\leq n\leq N}$ are called the *quadrature nodes*, and the real numbers $\{\omega_n\}_{0\leq n\leq N}$ the *quadrature weights*. Thus, another reasonable criterion is to select basis functions whose values at a specific set of quadrature points can be easily computed. A simple example, whenever possible, is that of Lagrange polynomials associated with these quadrature nodes, see Di Pietro and Ern [129, A. 2].

In our implementation, we have adopted orthonormal basis functions since they are more suitable and computationally stable. We have proposed to use monomial basis and recover an orthonormal basis through the L^2-based Gram-Schmidt orthogonalization approach.

4.4.5 Symmetric Weighted Interior Penalty (SWIP)method

In this subsection, we describe the DG method of SWIP used for solving the nonlinear coupled partial differential equations (3.2) defined on the domain $\Omega \subseteq \mathbb{R}^2$, where Ω is a convex polygonal subset. The SWIP bilinear form was introduced by Dryja [54] for heterogeneous diffusion problems and analyzed in the more general context of diffusion-advection-reaction problems by Di Pietro et al. [128] and Ern et al. [61]. The main differences with respect to the more usual SIP bilinear form are the use of diffusion-dependent weighted averages to formulate the consistency and symmetry terms, and the presence of diffusion-dependent penalty parameter.

The state variables $c(\mathbf{x}, t)$, $E(\mathbf{x}, t)$, $b_m(\mathbf{x}, t)$, and $b_s(\mathbf{x}, t)$ in (3.2) are functions of space and time with values in $\Omega \times [0, T]$. For purposes of clear presentation, we describe the DG method for the reaction diffusion system (3.2) written in general form as follows

$$\left.\begin{array}{lcl} \mathbf{u}_t(\mathbf{x}, t) - \mathbf{D}\Delta\mathbf{u} - \mathbf{r}(\mathbf{u}) & = & \mathbf{0} \quad \text{in} \quad \Omega \times \ [0, T] \\ \mathbf{u}(\mathbf{x}, 0) & = & \mathbf{u}_0(\mathbf{x}) \quad \text{on} \quad \Omega \times (t = 0) \\ \mathbf{n} \cdot \nabla\mathbf{u}(\mathbf{x}, t) & = & 0 \quad \text{on} \quad \partial\Omega \times \ [0, T] \end{array}\right\} \tag{4.27}$$

where $\mathbf{u} \in \mathbb{R}^4$ is such that $u_1 = c,\ u_2 = E,\ u_3 = b_m,\ u_4 = b_s$ and $\mathbf{D} \in \mathbb{R}^4 \times \mathbb{R}^4$ is a diagonal positive definite matrix given by $D_{11} = D_c,\ D_{22} = D_E,\ D_{33} = D_{b,m},\ D_{44} = D_{b,s}$. The vector $\mathbf{r}(\mathbf{u}) \in \mathbb{R}^4$ includes the reaction in each of the four equations. In (4.27) we have $\Delta\mathbf{u} = [\Delta u_1, \Delta u_2, \Delta u_3, \Delta u_4]^T$. We use the weighted DG formulation in Di Pietro and Ern [129, Sec.4.5] to discretize (4.27) in space but keep the time variable continuous. In this formulation, we use diffusion-dependent weights to formulate the consistency and symmetry terms in the discrete bilinear form and penalize interface and boundary jumps using a diffusion-dependent parameter scaling as the *harmonic mean* of the diffusion coefficient. For any interface $F \in \mathcal{F}_h^i$ with $F = \partial T_1 \cap \partial T_2$, we assign two nonnegative real numbers $\omega_{T_1,F}$ and $\omega_{T_2,F}$ such that

$$\omega_{T_1,F} + \omega_{T_2,F} = 1.$$

Then, for any scalar-valued function v defined on Ω that is smooth enough to admit a possibly two-valued trace on all $F \in \mathcal{F}_h^i$, we define its *weighted average* on F such that, for a.e. $x \in F$,

$$\{\!\{v\}\!\}_{\omega,F}(x) := \omega_{T_1,F} v|_{T_1}(x) + \omega_{T_2,F} v|_{T_2}(x).$$

On boundary faces $F \in \mathcal{F}_h^b$ with $F = \partial T \cap \partial\Omega$, we set $\{\!\{v\}\!\}_{\omega,F}(x) := v|_T(x)$. When v is vector-valued, the weighted average operator acts componentwise on the function v. Whenever no confusion can arise, the subscript F and the variable x are omitted and we simply write $\{\!\{v\}\!\}_\omega$. The choice $\omega_{T_1,F} = \omega_{T_2,F} = \frac{1}{2}$ recovers the usual arithmetic average. We denote the volume of a face by $|F|$.

We remark that as for the SIP bilinear form presented in subsection 4.4.3, the SWIP is coercive and bounded on V_h with respect to the suitable energy norm as depicted in Ern et al. [61]. Moreover, the error estimate and convergence are robust in the same norm with a convergence rate of order k if polynomials of degree k are used and the exact solution is smooth enough. Besides, if the exact solution $u \in H^{k+1}(\mathcal{T}_h)$, then we have the following convergence order in the L^2-norm

$$\|u - u_h\|_{L^2(\Omega)} \leq C_\lambda h^{k+1} \|u\|_{H^{k+1}(\mathcal{T}_h)},$$

where C_λ is a positive constant depending on the eigenvalues of D but not on h. For more details on the energy - error estimates of the SWIP DG method, see [129, 61].

The DG approximation space of degree k associated with $\mathcal{T}_h$ is defined as in (4.8) where $\mathbb{P}_d^k = \{p : p = \sum_{|\alpha| \leq k} \gamma_\alpha x^\alpha\}$ are the polynomials of at most degree k which are discontinuous along the edges of the mesh. The semi-discrete scheme is: Find $u_i(t) \in V_h$ such that for all $t \geq 0$, all $v_i \in V_h$ and $i = 1, \ldots, 4$

$$\left(\frac{\partial u_i}{\partial t}, v_i\right)_\Omega + a_\theta(u_i(t), v_i) = 0, \tag{4.28}$$

where

$$\left.\begin{aligned} a_\theta(u_i(t), v_i) = \; & \int_\Omega D_{ii} \nabla u_i \cdot \nabla v_i - \int_\Omega r_i(\mathbf{u}) \cdot v_i - \sum_{F \in \mathcal{F}_h} \int_F \{\!\{D_{ii} \nabla u_i \cdot \mathbf{n}_F\}\!\}_{\omega_i} [\![v_i]\!] \\ & + \theta \sum_{F \in \mathcal{F}_h} \int_F \{\!\{D_{ii} \nabla v_i \cdot \mathbf{n}_F\}\!\}_{\omega_i} [\![u_i]\!] + \sum_{F \in \mathcal{F}_h} \gamma_{F,i} \int_F [\![u_i]\!] [\![v_i]\!] \end{aligned}\right\}. \tag{4.29}$$

In the sequel, we denote $\omega_{T_1,F}$ by ω^- and $\omega_{T_2,F}$ by ω^+. Different choices of θ, of the penalty parameter γ_F and of the weights $\omega^\pm$ lead to the following well known types of DG methods: A choice of

- $\theta = -1$, $\omega^\pm = 1/2$ and $\gamma_\mathrm{F} = \gamma_0$ sufficiently large, leads to the symmetric interior penalty Galerkin (IP or SIP) method [160, 8, 9, 134, 61, 129];
- $\theta = +1$, $\omega^\pm = 1/2$ and $\gamma_\mathrm{F} > 0$, leads to the non-symmetric interior penalty Galerkin (NIP) method [135, 9, 134];
- $\theta = +1$, $\omega^\pm = 1/2$ and $\gamma_\mathrm{F} = 0$, leads to the method of Baumann and Oden [119, 24, 135, 134];
- $\theta = 0$, $\omega^\pm = 1/2$ and $\gamma_\mathrm{F} = \gamma_0$ sufficiently large, leads to the incomplete interior penalty Galerkin (IIP) method [49, 134].

To account for the discontinuities and locally small diffusivity, we choose the weights as a function of the diffusion coefficients, see [61, 129], and compute them as follows

$$\omega^- = \frac{\delta^+_{\mathbf{Dn_F}}}{\delta^-_{\mathbf{Dn_F}} + \delta^+_{\mathbf{Dn_F}}}, \qquad \omega^+ = \frac{\delta^-_{\mathbf{Dn_F}}}{\delta^-_{\mathbf{Dn_F}} + \delta^+_{\mathbf{Dn_F}}}$$

with $\delta^\pm_{\mathbf{Dn_F}} = \mathbf{n_F^T D^\pm n_F}$ for $\mathrm{F} \in \mathcal{F}_\mathrm{h}$ and $\delta^-_{\mathbf{Dn_F}} = \mathbf{n_F^T D n_F}$ for $\mathrm{F} \in \partial\mathrm{T}^- \cap \partial\Omega$ leading to the weighted interior penalty Galerkin, WIP, family of [61, 129]. The choice of the interior penalty parameter γ_F is crucial to ensure as much independence from the problem and mesh parameters as possible. We define the penalty parameter as

$$\gamma_F = \begin{cases} \alpha \frac{2\delta^-_{\mathbf{Dn_F}}\delta^+_{\mathbf{Dn_F}}}{\delta^-_{\mathbf{Dn_F}} + \delta^+_{\mathbf{Dn_F}}} k(k+d-1) \frac{|F|}{\min(|\mathrm{T_1(F)}|, |\mathrm{T_2(F)}|)} & \forall F \in \mathcal{F}_h^i, \\ \alpha \delta^-_{\mathbf{Dn_F}} k(k+d-1) \frac{|F|}{|T_1(F)|}, & \forall F \in \mathcal{F}_h^b \end{cases}$$

with a user-defined parameter $\alpha > 0$. This choice is a combination of suggestions made in three different publications. The harmonic average of "normal" permeabilities was introduced and analyzed in [61], the dependence on the polynomial degree was analyzed in [57], and the mesh-dependence is taken from [84]. We use orthonormal monomial basis functions, where the basis functions of $\mathbb{P}_d^k(\mathcal{T}_h)$ have support contained only in one element

$$\mathbb{P}_d^k(\mathcal{T}_h) = \mathrm{span}\{\phi_i^T : 1 \le i \le N_{loc},\ T \in \mathcal{T}_h\},$$

$$\phi_i^T(\mathbf{x}) = \begin{cases} \phi_i \circ \mathcal{G}_T(\mathbf{x}) & \mathbf{x} \in T, \\ 0 & \mathbf{x} \notin T. \end{cases} \tag{4.30}$$

where N_{loc} are the basis functions in T and $\mathcal{G}_T$ is the map from the reference element to the real element. For piecewise linears, the polynomial on T is represented by $u(x, y, t) = a_T(t)+b_T(t)x+c_T(t)y$ so that $\phi_1(x, y) = 1$, $\phi_2(x, y) = x$, $\phi_3(x, y) = y$. In our implementation, all computations are done on the reference element then transformed to the physical element. For instance, the reference triangular element consists of a triangle $\hat{T}$ with vertices $\hat{A}_1(0, 0), \hat{A}_2(1, 0)$ and $\hat{A}_3(0, 1)$, see Figure 4.4. For a given physical element T, there is an affine map $\mathcal{G}_T$ from the reference element onto T. If T has vertices $A_i(x_i, y_i)$ for $i = 1, 2, 3$, then the map $\mathcal{G}_T$ is defined by, see Riviere [134, Sect. 2.5]

$$\mathcal{G}_T \begin{pmatrix} \hat{x} \\ \hat{y} \end{pmatrix} = \begin{pmatrix} x \\ y \end{pmatrix}, \quad x = \sum_{i=1}^{3} x_i \hat{\phi}(\hat{x}, \hat{y}), \quad y = \sum_{i=1}^{3} y_i \hat{\phi}(\hat{x}, \hat{y})$$

where

$$\begin{aligned} \hat{\phi}_1(\hat{x}, \hat{y}) &= 1 - \hat{x} - \hat{y}, \\ \hat{\phi}_2(\hat{x}, \hat{y}) &= \hat{x}, \\ \hat{\phi}_3(\hat{x}, \hat{y}) &= \hat{y}. \end{aligned}$$

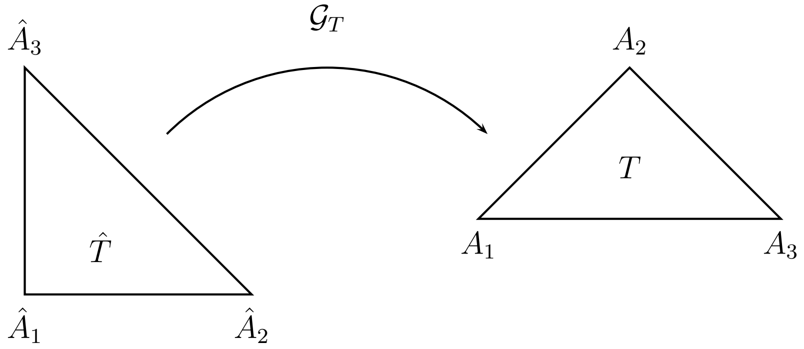

Figure 4.4: Reference triangular element $\hat{T}$ and physical element T

We can rewrite the mapping

$$\begin{pmatrix} x \\ y \end{pmatrix} = \mathcal{G}_T \begin{pmatrix} \hat{x} \\ \hat{y} \end{pmatrix} = \mathbf{B}_T \begin{pmatrix} \hat{x} \\ \hat{y} \end{pmatrix} + \mathbf{b}_T$$

where $\mathbf{B}_T$ is a 2×2 matrix and $\mathbf{b}_T$ is a vector. In the general case, we define $\mathbf{B}_T$ to be the Jacobian matrix of $\mathcal{G}_T$:

$$\mathbf{B}_T = \begin{pmatrix} \frac{\partial x}{\partial \hat{x}} & \frac{\partial x}{\partial \hat{y}} \\ \frac{\partial y}{\partial \hat{x}} & \frac{\partial y}{\partial \hat{y}} \end{pmatrix}.$$

It is sufficient to have the determinant of $\mathbf{B}_T$ nonvanishing in order to have an invertible map $\mathcal{G}_T$. This condition is satisfied if T is convex.

The semi-discrete form in (4.28) yields a system of Ordinary Differential Equations with the vector of unknowns $\mathbf{u}(t)$ given as

$$\left.\begin{array}{lcl} \mathbf{M}\frac{\partial \mathbf{u}}{\partial t} + \mathbf{A}\mathbf{u}(t) & = & 0, \\ \mathbf{u}(0) & = & \mathbf{u_0}. \end{array}\right\} \tag{4.31}$$

where $\mathbf{M}$ is the mass matrix and $\mathbf{A}$ is the stiffness matrix that comes from the bilinear form (4.29), or equivalently write

$$\mathbf{M}\dot{\mathbf{u}} = -\mathbf{A}\mathbf{u} \tag{4.32}$$

where we take the block diagonal matrices $\mathbf{M} = \mathrm{diag}(\mathcal{M}, \mathcal{M}, \mathcal{M}, \mathcal{M})$. The matrix $\mathbf{A}$ is a block matrix of the four equations which is symmetric for the case $\theta = -1$ in (4.29).

4.4.6 Matrix assembly

Matrix assembly for DG methods differs from that for conforming FE methods because

(i) the degrees of freedom associated with each mesh element are decoupled from those associated with the remaining elements,

(ii) terms involving integrals on interfaces are generally present.

We illustrate the first point by considering the mass matrix, and then illustrate the second point by considering the stiffness matrix resulting from the discrete bilinear form associated with a purely diffusive model problem. At the discrete level, we consider an approximation space V_h given by the broken polynomial space $\mathbb{P}_d^k(\mathcal{T}_h)$ defined by (4.8). We exploit the fact that the restriction of a function $v_h \in V_h$ to a given mesh element $T \in \mathcal{T}_h$ can be chosen independently of its restriction to other elements, whereby we restrict the support of basis functions to a single mesh element. This is generally a good idea, since it reduces communications between mesh elements and, therefore, yields the minimal stencil, see Figure 4.3. It is assumed that the global enumeration of the degrees of freedom is such that the local degrees of freedom are numbered contiguously for each mesh element. This leads to a basis for V_h of the form

$$\Phi := \{\{\phi_i^T\}_{i \in \mathcal{D}_T}\}_{T \in \mathcal{T}_h},$$

where the set $\mathcal{D}_T = \{1, \ldots, N_{loc}^T\}$ collects the local indices of the N_{loc}^T degrees of freedom for the mesh element T and where

$$\mathrm{supp}(\phi_i^T) = \bar{T}, \quad \forall T \in \mathcal{T}_h, \quad \forall i \in \mathcal{D}_T.$$

The dimension of V_h is therefore equal to $\sum_{T\in\mathcal{T}_h} N_{loc}^T$. The local number of degrees of freedom N_{loc}^T for our case where $V_h = \mathbb{P}_d^k(\mathcal{T}_h)$ is constant and equal to $\dim(\mathbb{P}_d^k) = \frac{(k+d)!}{k!d!}$. The global mass matrix is associated with the bilinear form

$$m(v_h, w_h) = \int_\Omega v_h w_h, \qquad \forall\, v_h,\ w_h \in V_h.$$

Exploiting the localization of basis functions to single mesh elements, the *global mass matrix* can be block-partitioned in the form

$$\mathbf{M} = \begin{bmatrix} \mathbf{M}_{T_1T_1} & 0 & \dots & 0 \\ 0 & \mathbf{M}_{T_2T_2} & \ddots & \vdots \\ \vdots & \ddots & \ddots & 0 \\ 0 & \dots & 0 & \mathbf{M}_{T_NT_N} \end{bmatrix},$$

where $N := \operatorname{card}(\mathcal{T}_h)$. The local mass matrix corresponding to a generic element $T \in \mathcal{T}_h$ is

$$\mathbf{M}_{TT} = \left[m(\phi_j^T, \phi_i^T)\right] \in \mathbb{R}^{N_{loc}^T, N_{loc}^T},$$

and this matrix is obviously symmetric positive definite, and thus is invertible. Focusing on the purely diffusive model problem (4.25) with the discrete bilinear form a_h^{sip} defined by (4.23), the *global stiffness matrix* can be block-partitioned in the form

$$\mathbf{A} = \begin{bmatrix} \mathbf{A}_{T_1T_1} & \mathbf{A}_{T_1T_2} & \dots & \mathbf{A}_{T_1T_N} \\ \mathbf{A}_{T_2T_1} & \mathbf{A}_{T_2T_2} & \ddots & \mathbf{A}_{T_2T_N} \\ \vdots & \vdots & \ddots & \vdots \\ \mathbf{A}_{T_NT_1} & \mathbf{A}_{T_NT_2} & \dots & \mathbf{A}_{T_NT_N} \end{bmatrix},$$

where, for all $T_k,\ T_l\ \in \mathcal{T}_h$,

$$\mathbf{A}_{T_kT_l} = \left[a_h^{\text{sip}}(\phi_j^{T_l}, \phi_i^{T_k})\right] \in \mathbb{R}^{N_{loc}^{T_k}, N_{loc}^{T_l}}.$$

In view of the elementary stencil associated with the SIP bilinear form, see Figure 4.3, the block $A_{T_kT_l}$ is nonzero only if $T_k = T_l$ (diagonal block) or if T_k and T_l share a common interface. We split the bilinear form a_h^{sip} into *volume*, *interface*, and *boundary face* contributions as follows: For all $v_h,\ w_h \in V_h$,

$$a_h^{\text{sip}}(v_h, w_h) = a_h^{\text{v}}(v_h, w_h) + a_h^{\text{if}}(v_h, w_h) + a_h^{\text{bf}}(v_h, w_h)$$

where

$$\begin{aligned} a_h^{\mathrm{v}}(v_h, w_h) &= \sum_{T\in\mathcal{T}_h} \int_T \nabla_h v_h \cdot \nabla_h w_h, \\ a_h^{\mathrm{if}}(v_h, w_h) &= \sum_{F\in\mathcal{F}_h^i} \int_F \left(\{\!\{\nabla_h v_h\}\!\} \cdot \mathbf{n}_F [\![w_h]\!] + [\![v_h]\!] \{\!\{\nabla_h w_h\}\!\} \cdot \mathbf{n}_F + \frac{\eta}{h_F}[\![v_h]\!][\![w_h]\!] \right), \\ a_h^{\mathrm{bf}}(v_h, w_h) &= \sum_{F\in\mathcal{F}_h^b} \int_F \left(\nabla_h v_h \cdot \mathbf{n} w_h + v_h \nabla_h w_h \cdot \mathbf{n} + \frac{\eta}{h_F} v_h w_h \right). \end{aligned}$$

Each summation yields a loop over the corresponding mesh entities to assemble local contributions into the global stiffness matrix. The local stiffness matrix stemming from the volume contribution of a generic mesh element $T \in \mathcal{T}_h$ is

$$\mathbf{A}^T = \left[a_h^{\mathrm{v}}(\phi_j^T, \phi_i^T)\right] \in \mathbb{R}^{N_{loc}^T, N_{loc}^T}.$$

and it contributes to the diagonal block $\mathbf{A}_{TT}$ of the global stiffness matrix $\mathbf{A}$. An interface $F \in \mathcal{F}_h^i$ contributes to four blocks of the global stiffness matrix $\mathbf{A}$, and the local stiffness matrix stemming from the interface contribution can be block-partitioned in the form

$$\mathbf{A}^F = \begin{bmatrix} \mathbf{A}_{T_1T_1}^F & \mathbf{A}_{T_1T_2}^F \\ \mathbf{A}_{T_2T_1}^F & \mathbf{A}_{T_2T_2}^F \end{bmatrix},$$

where $F = \partial T_1 \cap \partial T_2$,

$$\mathbf{A}_{T_mT_n}^F = \left[a_h^{\mathrm{if}}(\phi_j^{T_{n'}}, \phi_i^{T_{m'}})\right] \in \mathbb{R}^{N_{loc}^{T_{m'}}, N_{loc}^{T_{n'}}} \qquad \forall\, m, n \in \{1, 2\},$$

and $1', 2' \in \{1, \ldots, N\}$ are the indices of T_1, T_2 in the global enumeration of mesh elements. Finally, a boundary face $F \in \mathcal{F}_h^b$ contributes through the local stiffness matrix

$$\mathbf{A}^F = \left[a_h^{\mathrm{bf}}(\phi_j^T, \phi_i^T)\right] \in \mathbb{R}^{N_{loc}^T, N_{loc}^T}.$$

where $F = \partial T_1 \cap \partial\Omega$. The procedure for global matrix assembly is summarized in the following algorithm.

Algorithm 1

```
for $T \in \mathcal{T}_h$ do { Loop over elements}
    $\mathbf{A}_{TT} \leftarrow \mathbf{A}_{TT} + \mathbf{A}^T$
end for
for $F \in \mathcal{F}_h^i$ s.t. $F = \partial T_1 \cap \partial T_2$ do { Loop over interfaces}
```

```
  for $m = 1$ to $2$ do
    for $n = 1$ to $2$ do
      $\mathbf{A}_{T_{m'}T_{n'}} \leftarrow \mathbf{A}_{T_{m'}T_{n'}} + \mathbf{A}^{F}_{T_m T_n}$
    end for
  end for
end for
for $F \in \mathcal{F}_h^b$ s.t. $F = \partial T_1 \cap \partial\Omega$ do { Loop over boundary faces}
  $\mathbf{A}_{TT} \leftarrow \mathbf{A}_{TT} + \mathbf{A}^{T}$
end for
```

Since in the DG setting each unknown can be unambiguously associated to an element, its natural to order the components of $\mathbf{u}$ in such a way that all the unknowns associated to an element appear contiguously. Furthermore, it is computationally efficient to number all the unknowns corresponding to each of the m components of u consecutively within each element. This allows common operations required for the residual and Jacobian evaluation, such as interpolating the unknowns at the integration points, to be carried out while maximizing contiguous memory access. With this ordering, the block structure of matrix $\mathbf{A}$ has the size of each block given by the number of nodes within each element, and the total number of blocks is equal to the number of elements times m. In particular, $\mathbf{A}$ has a nontrivial block structure which is determined by the element connectivity. On the other hand, $\mathbf{M}$ is block diagonal as it involves no dependencies between elements or solution components. We note that all the nonzero entries in $\mathbf{M}$ are also nonzero entries in $\mathbf{A}$. For illustration purposes, Figure 4.5 shows the sparsity pattern of the $\mathbf{A}$ matrix for a sample mesh consisting of four triangular elements and $m = 1$.

4.5 Time discretization

The discretization in time of (4.31) can be accomplished in several possible ways. A classical and widespread practice to achieve a full discretization of (4.31) is to resort to a discretization of the time derivative by a finite difference scheme. Stiff initial value problems put special demands on the methods to be used for time discretization. First, for stability reasons one has, in order to avoid excessively small time steps, use *implicit* methods, i.e., methods requiring the solution of a system of equations at each time step. Secondly, one would like to use methods which automatically adapt the size of the time steps according to the smoothness of $\mathbf{u}_h$ and thus automatically take smaller time steps in a transient and larger steps when $\mathbf{u}_h$ becomes smoother.

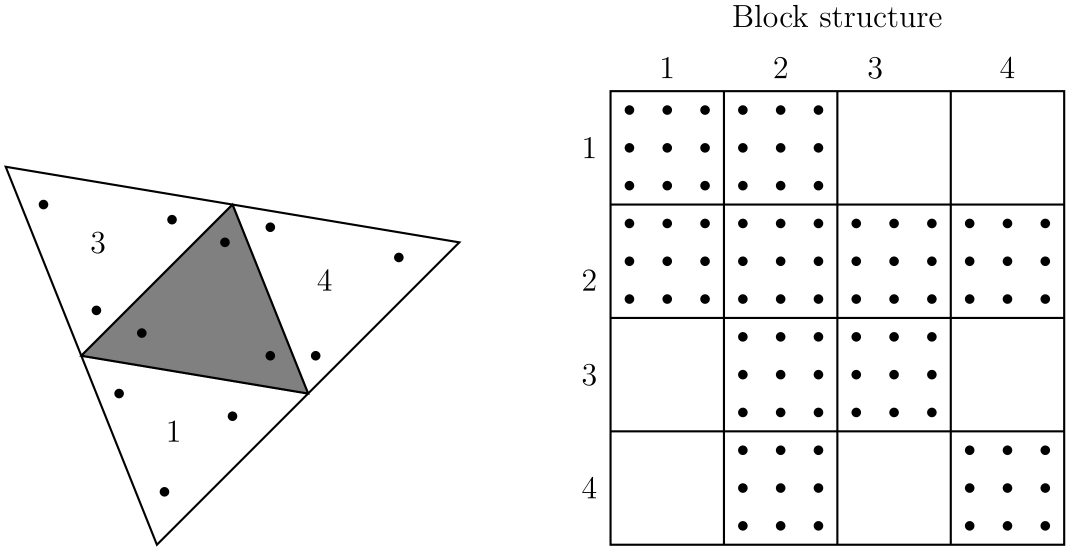

Figure 4.5: Sparsity structure of the stiffness matrix $\mathbf{A}$ for a triangle and its neighbors, with polynomial degree $k = 1$ and $m = 1$.

Since the matrix system in (4.31) is highly stiff, we have concentrated on implicit methods for solving these equations. We have implemented the linearly implicit Runge-Kutta methods of Rosenbrock type, see Lang [98], and a certain class of diagonally implicit Runge-Kutta (DIRK) methods, see Alexander [3], which are suitable for stiff systems. For the DIRK method, we used Newton iteration to solve the nonlinear equations. The Rosenbrock methods have several advantages. For instance, they completely avoid the solution of nonlinear equations and therefore no Newton iteration is required. Moreover, for computation of adaptive time steps, a simple embedding technique can be utilized to estimate the error arising from the time discretization. More detailed expositions of these methods together with Butcher tables can be found in [75, 98]. An automatic stepsize selection procedure ensures that the stepsize is as large as possible while guaranteeing the desired precision.

We considered the ODE system

$$\mathbf{M}\frac{\partial \mathbf{u}_h}{\partial t} = \mathbf{F}(\mathbf{u}_h(t)) \ ; \ \mathbf{u}(0) = \mathbf{u_0}. \tag{4.33}$$

where $\mathbf{F}(\mathbf{u}_h(t))$ is a continuous function from $[0, T] \times \mathbb{R}$ into $\mathbb{R}$ which is further Lipschitz continuous with respect to $\mathbf{u}_h$, uniformly in $t \in [0, T]$. Since the Rosenbrock methods were computationally more efficient for this system than the DIRK method, we briefly describle our time discretization based on these methods. The time $[0, T]$ is partitioned into discrete steps $0 = t^0, t^1, ..., t^n = T$, that are not necessarily equidistant. The time step has the notation $\tau^i = t^{i+1} - t^i$ and $\mathbf{u}_h^i$ is the numerical solution at time t^i. An s-stage *Rosenbrock* method of order p with embedding of order $\hat{p} \neq p$ has the form

$$(\frac{1}{\tau^i \gamma}\mathbf{M} - \mathbf{J})\mathbf{k}_j = \mathbf{F}\left(t^i + \tau^i \alpha_j, \mathbf{u}_h^i + \sum_{l=1}^{j-1} a_{jl}\mathbf{k}_l\right) - \mathbf{M}\sum_{l=1}^{j-1}\frac{c_{lj}}{\tau^i}\mathbf{k}_l, \quad j = 1, ...s, \tag{4.34}$$

$$\mathbf{u}_h^{i+1} = \mathbf{u}_h^i + \sum_{l=1}^{s} m_l \mathbf{k}_l, \tag{4.35}$$

$$\hat{\mathbf{u}}_h^{i+1} = \mathbf{u}_h^i + \sum_{l=1}^{s} \hat{m}_l \mathbf{k}_l. \tag{4.36}$$

The Jacobian matrix $\mathbf{J}$ is given as $\mathbf{J} = \partial \mathbf{F}/\partial \mathbf{u}_h$. For the construction of $\mathbf{J}$ we used exact derivatives of the vector $\mathbf{F}(t, \mathbf{u}_h)$. The coefficients $\gamma, \alpha_j, a_{jl}, c_{jl}, m_l$, and $\hat{m}_l$ for the method are chosen in such away that certain order conditions are fulfilled to obtain a sufficient consistency order and good stability properties. The coefficients in equation (4.35) are replaced by different coefficients $\hat{m}_l$ to construct a second solution of lower order $\hat{p}$ where $\hat{p} < p$, see [75, 98]. After the i-th integration step, the value $\epsilon^{i+1} = \|\mathbf{u}_h^{i+1} - \hat{\mathbf{u}}_h^{i+1}\|_{L^2}$ is taken as an estimator of the local temporal error. In the numerical integration of ordinary differential equations, automatic stepsize control is the most important means to make an integration method efficient. Here we used a standard rule to compute a new time step τ_{new} as follows, see e.g., [74, 145],

$$\bar{\tau} := \beta\left(\frac{TOL_t}{\epsilon^{i+1}}\right)^{\frac{1}{p}} \tau^i, \quad \tau_{new} = \begin{cases} \beta_{\max}\tau^i, & \bar{\tau} > \beta_{\max}\tau^i \\ \beta_{\min}\tau^i, & \bar{\tau} < \beta_{\min}\tau^i \\ \bar{\tau}, & \text{otherwise.} \end{cases} \tag{4.37}$$

The parameter $\beta > 0$ is a safety factor. The factors $\beta_{\min}$ and $\beta_{\max}$ restrict time step jumps. If $\epsilon < TOL_t$ where TOL_t is a desired tolerance prescribed by the user, we proceed to the next time step, otherwise the time step has to be reduced according to equation (4.37) and a new attempt is perfomed. The stepsize oscillates violently and much computation time is spent by recalculating the rejected steps and changing the stepsize. This is especially true in the case of stiff differential equations, see for more details Gustafsson et el. [73], Hairer and Wanner [75]. We observed this also in our computations especially with coarser grids.

For our simulations we used the ROWDA method, see [98], which is a 3(2) order method with 3 internal stages. The coefficients are given in Table 4.2. The implemented DIRK method is strongly S-stable and is of order 3 with 3 internal stages. The coefficients of the Butcher table are given in Table 4.3,

$\gamma = 0.435866521508459$	$\alpha_1 = 0.0$ $\alpha_2 = 0.7$ $\alpha_3 = 0.7$
$a_{11} = a_{22} = a_{32} = a_{33} = 0.0$ $a_{21} = 1.605996252195329$ $a_{31} = 1.605996252195329$	$c_{11} = 2.294280360279042$ $c_{21} = -0.8874044410657823$ $c_{22} = 2.294280360279042$ $c_{31} = -23.98747971635035$ $c_{32} = -5.263722371562130$ $c_{33} = 2.294280360279042$
$m_1 = 2.236727045296589$ $m_2 = 2.250067730969645$ $m_3 = -0.2092514044390320$	$\hat{m}_1 = 2.059356167645941$ $\hat{m}_2 = 0.1694014319346527$ $\hat{m}_3 = 0.0$

Table 4.2: Set of coefficients for the ROWDA3 method

$$
\begin{array}{c|ccc}
\alpha & \alpha & 0 & 0 \\
\tau_2 & \tau_2 - \alpha & \alpha & 0 \\
1 & b_1 & b_2 & \alpha \\
\hline
 & b_1 & b_2 & \alpha
\end{array}
$$

Table 4.3: Butcher table for the DIRK method

where α is the root of $x^3 - 3x^2 + \frac{3}{2}x - \frac{1}{6} = 0$ lying in $(\frac{1}{6}, \frac{1}{2})$, $\tau_2 = (1+\alpha)/2$, $b_1 = -(6\alpha^2 - 16\alpha + 1)/4$ and $b_2 = (6\alpha^2 - 20\alpha + 5)/4$. For more details on the DIRK method and the adaption strategy, see [3]. After the time discretization, we obtain an algebraic system of equations in each internal stage.

4.6 Solution of algebraic equations

In this section we concentrate on the solution of the algebraic equations arising within each time step of the fully implicit/fully coupled solution procedure. The nonlinear and linear solvers to be described in this section utilize a multigrid mesh structure to accelerate the solution process. This multigrid mesh structure is denoted by $E_0, \ldots E_J$. It is constructed from an initial mesh, which is generated by an initial grid generator, by regular subdivision of each element. In our computations, initial mesh and finer meshes have been generated based on the software package DUNE [21]. For refinement rules in sequential and parallel cases, see e.g., Bank et al. [14], Bastian [18] and Lang [98].

4.6.1 Inexact Newton method

Each time step of the fully implicit scheme leads to a large set of nonlinear algebraic equations

$$\mathbf{G}(\mathbf{u}_h) = \mathbf{0}, \tag{4.38}$$

to be solved. The vector $\mathbf{u}_h$ contains the unknowns. A classical algorithm for solving the system of nonlinear equations (4.38) is Newton's method:

$$\mathbf{u}_h^{k+1} = \mathbf{u}_h^k + s^k, \quad \text{where } J(\mathbf{u}_h^k)s^k = -\mathbf{G}(\mathbf{u}_h^k), \quad \mathbf{u}_h^0 \text{ given},$$

and the Jacobian J of $\mathbf{G}$ is the matrix with entries that can be computed either analytically or by numerical differentiation.

$$J(\mathbf{u}_h)_{ij} := \frac{\partial \mathbf{G}_i}{\partial \mathbf{u}_h}(\mathbf{u}_h).$$

The method is attractive because it converges rapidly from any sufficiently good initial guess $\mathbf{u}_h^0$. However, solving a system of linear equations (the Newton equations) at each stage can be expensive if the number of uknowns is large and may not be justified when $\mathbf{u}_h^k$ is far from a solution. Therefore, we consider the class of inexact Newton methods which solve the Newton equations only approximately and in some unspecified manner. These methods provide a trade-off between the accuracy with which the Newton equations are solved and the amount of work per iteration, see e.g., Kelly [95, Ch. 6].

Let k denote the iteration number and $\|\cdot\|_2$ be the Euclidean vector norm. We give the inexact Newton algorithm in Algorithm 2, see e.g., Bastian [19] and Braess [33].

Algorithm 2

```
input ⟵ $\mathbf{G}$, $\mathbf{u}_h$, $TOL_{nl}$
$k := 0$; $\mathbf{u}_h^0 := \mathbf{u}_h$
while ($\|\mathbf{G}(\mathbf{u}_h^k)\|_2 \geq TOL_{nl}\|\mathbf{G}(\mathbf{u}_h^0)\|_2$) do
choose $TOL_{nl} \in ]0,1]$
find $s^k$ such that
    $\|\mathbf{G}(\mathbf{u}_h^k) + J(\mathbf{u}_h^k)s^k\|_2 \leq TOL_{nl}\|\mathbf{G}(\mathbf{u}_h^k)\|_2$
choose $\lambda_k \in ]0,1]$
$\mathbf{u}_h^{k+1} = \mathbf{u}_h^k + \lambda^k s^k$
$k := k+1$
end while
```

Algorithm 2 solves the nonlinear system $\mathbf{G}(\mathbf{u}_h) = \mathbf{0}$ to accuracy TOL_{nl} starting from the initial guess $\mathbf{u}_h$. Since the Newton method converges only in a sufficiently close neighborhood of the solution, a damping strategy is needed to achieve global convergence. Step (7) in Algorithm 2 implements a simple line search strategy where the damping factor λ^k is chosen as the largest value in the set $\{1, \frac{1}{2}, \frac{1}{4} \ldots\}$ such that

$$\|\mathbf{G}(\mathbf{u}_h^k + \lambda^k s^k)\|_2 \leq (1 - \frac{1}{4}\lambda^k)\|\mathbf{G}(\mathbf{u}_h^k)\|_2. \tag{4.39}$$

More details of this strategy can also be found in Braess [33].

4.6.2 Solution of linear equations

We use *Krylov subspace methods* to solve the linear system

$$A\mathbf{u}_h = \mathbf{b}. \tag{4.40}$$

This linear system arises from the linearization of the non linear system using Newton's method or in each stage of a linearly implicit time stepping method. For large number of unknowns iterative methods are an appropriate choice. Starting with an initial guess $\mathbf{u}_h^0$ iterative methods for the resolution of system (4.40) produce a sequence of iterates $\mathbf{u}_h^1, \mathbf{u}_h^2, \ldots$ that converges to the exact solution $\mathbf{u}_h$. In general, Krylov methods must be preconditioned to perform well. This amounts to finding an approximate solver for $A\mathbf{u}_h = \mathbf{b}$ which is relatively inexpensive to apply. From an implementation perspective these methods do not require the explicit form of the system matrix $\mathbf{A}$ but only its effect on a given vector $\mathbf{p}$, that is, $A\mathbf{p}$. Similarly, the effect of a left preconditioner requires only the ability to approximately calculate $\mathbf{A}^{-1}\mathbf{p}$, see Persson and Peraire [125].

For instance, for a DG mesh consisting of ne elements, we think of the matrix $\mathbf{A}$ as consisting of ne-by-ne blocks. Further, we let $\mathbf{A}_{ij}$ denote the block with indices i, j. The goal is to compute a matrix $\tilde{\mathbf{A}}$ which approximates $\mathbf{A}$ and which allows for the computation of $\tilde{\mathbf{A}}^{-1}\mathbf{p}$ for an arbitrary vector $\mathbf{p}$ in an inexpensive manner.

Incomplete matrix factorizations are commonly used as general purpose preconditioners for Krylov solvers. A major drawback for DG discretizations is that the resulting linear system has a higher number of degrees of freedom when compared with the continuous methods. This leads to even larger and more ill-conditioned systems and makes the use of optimal solvers even more mandatory. The quest for such solvers is still ongoing as recent publications such as Blatt et al. [22] and references cited therein show.

In our computations, we used mainly two linear solvers, i.e., the conjugate gradient (CG) and the bi-conjugate gradient stabilized (BiCGSTAB) solvers with four preconditioners i.e. Algebraic Multigrid (AMG)[22], Jacobi, Symmetric Successive Over Relaxation(SSOR) and a preconditioner based on a coarse scale correction with post-smoothing based on a block incomplete LU factorization with zero fill-in of the Jacobian matrix (ILU0)[125]. Our numerical experiments revealed that the AMG method is an attractive option for DG preconditioning, because it offers a superior performance at a comparable cost to the other three methods.

The implementation of the linear solvers and preconditioners used in our work is available in the open source PDE framework DUNE, see Bastian et al. [21]. For more details on the several known Krylov subspace methods and preconditioners together with their algorithms, see e.g., Barrett et al. [16] and Saad [142].

4.7 Parallel implementation

Domain decomposition methods allow for the effective implementation of numerical techniques for partial differential equations on parallel architectures. Any such method is based on the assumption that the given computational domain, say Ω, is partitioned into subdomains $\Omega_i,\ i = 1, \ldots, \mathbf{p}$, that may or may not overlap. Next, the original problem can be reformulated upon each subdomain Ω_i yielding a family of subproblems of reduced size which are to be coupled to each others through the values of the unknown solution at subdomain interfaces. The interface coupling can be relaxed at the expense of introducing an iterative process among subdomains, yielding at each step independent sub problems upon subdomains. This domain decomposition may enter at the continuous level, where different physical models may be used in different regions. Or it may be introduced at the discretization level, where it may be convenient to employ different approximation methods in different regions. Or it may be introduced in the solution of the algebraic systems arising from the approximation of the partial differential equation. The parallel programming model in DUNE [21] is based on the third aspect of the domain decomposition approach.

The essence of parallel numerical simulation is to distribute the computational load evenly on all processors. This is the task of the domain decomposition algorithms. Our parallel numerical implementation of the discretization routines are based on the software package DUNE [21], especially the DUNE-PDELab discretization module, see Bastian et al. [23]. The external parallel UG grid [20] interface has been used for parallel grid constructions, which supports overlapping and non-overlapping grids. In the UG grid manager, the recursive coordinate bisection algorithms, a divide and conquer scheme, is used for domain decomposition. In each step of this algorithm the dual graph vertices are sorted according to their coordinate values and then the vertices are bisected into two equal sets using the mean value. The sets are then further divided by the recursive application of the same splitting algorithm until the number of sets equals the number of processors.

In this thesis, we have used overlapping domain decomposition methods to realize our parallel implementations. In this overlapping subdivision variant, each subdomain Ω_i is extended by an overlap of one layer of ghost elements of the parallel UG grid [20] at the processor boundaries. The mesh decomposition to different processors of the various spatial grids that we have used in our numerical simulations will be given in Chapter 5.

The BiCGSTAB [156] method with AMG preconditioning is used as the linear solver. To run in parallel, the BiCGSTAB solver has to be able to compute parallel matrix vector products and scalar products. For parallel preconditioners to the BiCGSTAB solvers, we use Schwarz additive methods. In these schemes, the local subproblem on each processor is solved where the values of the last iteration are used as Dirichlet constraints at the process boundary. In an overlapping decomposition, corrections are computed for the overlap at more than one process. The sum of the corrections multiplied with a relaxation coefficient is applied, see Bastian et al. [23].

Chapter 5

Numerical results

5.1 Introduction

In this chapter, we present a series of numerical experiments to validate the theoretical results of Chapter 3 and also highlight the practical performance of the DG discretization (4.29) for the numerical approximation of the equations (3.2). We start in Section 5.2 by checking the stability, accuracy and convergence of the DG method for a scalar linear and nonlinear reaction-diffusion equation with an exact solution. In Section 5.3, we test the performance of our code on the classical 2×2 Schnakenberg model whose numerical results are well known. An overview of how we generate the highly unstructured simplicial grids used for the spatial resolution of the computational domain is then given in Section 5.4. In Section 5.5, we present the numerical results based on the deterministic opening and closing of one channel in one cluster arrangement. By considering different grid levels, we also depict the numerical convergence of solutions here. In addition, some DG and FEM solutions are highlighted, as well as parallel efficiency results for the deterministic multi-cluster simulations. Finally, in Section 5.6, we exhibit numerical results for the hybrid stochastic and deterministic model both sequentially and in parallel.

For the model under study, we performed our simulations on a square geometry, $[0, 36000$ nano meters$(nm)] \times [0, 36000\ nm]$, as computational domain with refinement using triangular elements. This domain size represents an ER membrane. The parameters that have been used in the numerical simulation are shown in Table B.1. The initial solutions for concentrations and buffers are considered to be constants over the computational domain. Precisely, in our computations, we have used 0.002 micro moles per liter(μM), 705 μM, 0.326721 μM and 0.07992 μM for cytosolic Ca^{2+}, ER Ca^{2+}, mobile buffer and stationary buffer initial concentrations respectively. The sequential numerical simulations were performed on a 2.80 GHz, 95 GB RAM Linux PC with 12 cores, g++ -4.5.1 compiler and the SVN version of the program package DUNE, see Bastian et al. [21], which is an open source to the public written in C++.

5.2 Numerical tests on a scalar problem

In this section, we present results on tests for the stability, accuracy and efficiency of the DG spatial discretization in Section 4.4.5 and the DIRK time discretization for a linear and nonlinear parabolic PDE with exact solutions. These examples were taken from Zho [162], where fully implicit time schemes were used together with a spatial DG formulation that utilizes numerical fluxes.

To save space, we present only results for the SWIP method and omit the presentation of the results for the NWIP and IWIP methods, which follow a similar stability and accuracy pattern in our tests. First, we consider the two-dimensional linear problem.

$$\left\{\begin{array}{lcl} u_t - u_{xx} - u_{yy} & = & -u + 2\pi^2 e^{-t}\cos(\pi x)\cos(\pi y), \ (x,y) \in]0,1[^2 \\ u(x,y,0) & = & \cos(\pi x)\cos(\pi y), \end{array}\right. \tag{5.1}$$

with the no-flux boundary conditions. The exact solution is $u(x,y,t) = e^{-t}\cos(\pi x)\cos(\pi y)$. We use rectangular meshes. We start with 4 elements given by partitioning the square equally. We continue with uniform refinement i.e., cutting each square into four smaller similar ones. The simulation is performed upto time $T = 8.0$ *s* at which the L^2 error and CPU time are measured and listed in Tables 5.1 - 5.6. We use a local polynomial approximation of degree k upto $k = 3$. The time step is decreased successively as $\Delta t = 4h, 2h, h$ and $h/2$ for Q_1 elements. Since the grid for Q_2 elements is finer than Q_1 elements, we choose the time steps in the form $\Delta t = h, h/2, h/4$ and $h/8$. For the cubic polynomials , we choose the time steps as $\Delta t = h/8$ and $h/16$. Evidently, we observe that h^{k+1} order of accuracy is achieved, even with larger time steps for Q_1 elements. Subsequently, in Figure 5.1, we give plots of L^2-error as a function of h and *CPU time* respectively. As is expected, we observe in Figure 5.1 that the error is larger for large time steps but reduces as the number of cells and CPU time increases respectively. A similar trend can be seen in Figure 5.2 and Table 5.6. Besides, from Tables 5.1 - 5.6, one can deduce that it is computationally more efficient to use higher order polynomials on coarser grids and still obtain accurate results.

Next we consider the two-dimensional nonlinear problem

$$\left\{\begin{array}{lcl} u_t - u_{xx} - u_{yy} & = & -u^2 + e^{-2t}\cos(\pi x)^2\cos(\pi y)^2 \\ & & +(2\pi^2 - 1)e^{-t}\cos(\pi x)\cos(\pi y), \ (x,y) \in]0,1[^2, \\ u(x,y,0) & = & \cos(\pi x)\cos(\pi y), \end{array}\right. \tag{5.2}$$

with the no-flux boundary conditions. The exact solution is $u(x,y,t) = e^{-t}\cos(\pi x)\cos(\pi y)$. We use rectangular meshes. As for the case of the linear problem, we also start with

No of cells	$\Delta t = 4h$			$\Delta t = 2h$		
	CPU(s)	L^2 error	Order	CPU(s)	L^2 error	Order
4	0.003	3.920E-05	-	0.004	3.284E-05	-
16	0.016	1.155E-05	1.76	0.026	9.965E-06	1.72
64	0.111	3.065E-06	1.91	0.221	2.640E-06	1.92
256	0.983	7.798E-07	1.97	1.929	6.671E-07	1.98
1024	9.12	1.928E-07	2.02	18.171	1.657E-07	2.00
4096	92.855	4.650E-08	2.05	173.395	4.096E-08	2.02

Table 5.1: Simulation results with Q_1 elements.

No of cells	$\Delta t = h$			$\Delta t = 2/h$		
	CPU(s)	L^2 error	Order	CPU(s)	L^2 error	Order
4	0.011	3.168E-05	-	0.013	3.139E-05	-
16	0.053	9.582E-06	1.73	0.103	9.483E-06	1.73
64	0.42	2.532E-06	1.92	0.834	2.507E-06	1.92
256	3.638	6.409E-07	1.98	7.126	6.355E-07	1.98
1024	33.403	1.603E-07	2.00	61.384	1.594E-07	2.00
4096	322.093	4.001E-08	2.00	572.121	3.986E-08	2.00
16384	4311.769	9.985E-09	2.22	6920.282	9.965E-09	2.00
65536	52014.115	2.494E-09	2.00			

Table 5.2: Simulation results with Q_1 elements continued.

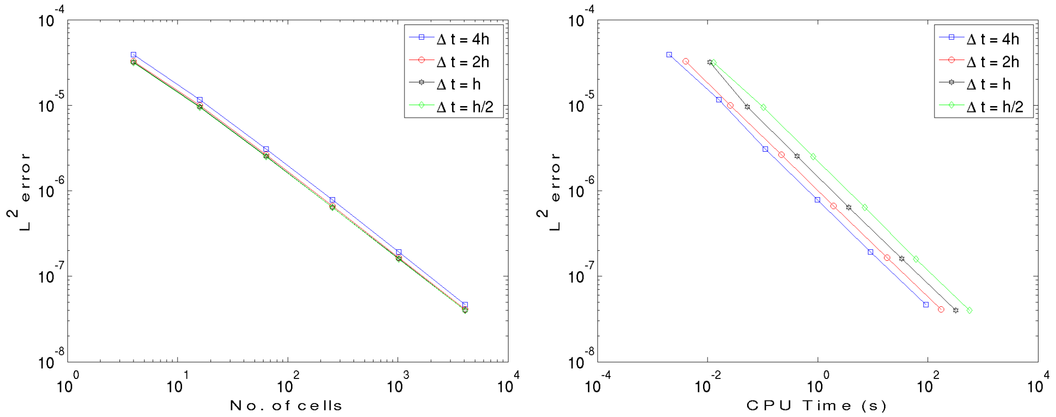

(a) (b)

Figure 5.1: L^2-error as a function of h and *CPU time* respectively for the four categories of time steps considered using Q_1 elements.

No of cells	$\Delta t = 4h$			$\Delta t = 2h$		
	CPU(s)	L^2 error	Order	CPU(s)	L^2 error	Order
4	0.006	1.324E-05	-	0.01	5.199E-06	-
16	0.042	2.737E-06	2.27	0.08	8.561E-07	2.60
64	0.383	6.662E-07	2.04	0.753	1.799E-07	2.25
256	3.528	1.672E-07	1.99	6.936	3.934E-08	2.19
1024	37.32	3.848E-08	2.12	71.154	7.738E-09	2.35
4096	579.924	7.672E-09	2.33	1061.254	1.323E-09	2.55

Table 5.3: Simulation results with Q_2 elements.

No of cells	$\Delta t = h$			$\Delta t = h/2$		
	CPU(s)	L^2 error	Order	CPU(s)	L^2 error	Order
4	0.018	4.160E-06	-	0.035	4.012E-06	-
16	0.161	5.253E-07	2.98	0.318	4.867E-07	3.04
64	1.476	7.226E-08	2.86	2.778	6.012E-08	3.02
256	13.073	1.078E-08	2.74	25.21	7.523E-09	3.00
1024	133.032	1.616E-09	2.74	239.9	9.445E-10	2.99
4096	1856.99	2.313E-10	2.80	3289.49	1.185E-10	2.99

Table 5.4: Simulation results with Q_2 elements continued.

No of cells	$\Delta t = h/4$			$\Delta t = h/8$		
	CPU(s)	L^2 error	Order	CPU(s)	L^2 error	Order
4	0.069	3.982E-06	-	0.141	3.976E-06	-
16	0.61	4.821E-07	3.05	1.221	4.814E-07	3.05
64	5.317	5.932E-08	3.02	10.318	5.925E-08	3.02
256	47.259	7.381E-09	3.00	88.5	7.373E-09	3.00
1024	436.048	9.213E-10	3.00	800.696	9.206E-10	3.00
4096	5181.499	1.151E-10	3.00	9027.933	1.150E-10	3.00

Table 5.5: Simulation results with Q_2 elements continued.

No of cells	$\Delta t = h/8$			$\Delta t = h/16$		
	CPU(s)	L^2 error	Order	CPU(s)	L^2 error	Order
4	0.32	4.189E-07	-	0.621	4.185E-07	-
16	3.057	2.888E-08	3.86	5.761	2.883E-08	3.86
64	26.799	1.866E-09	3.95	53.2	1.855E-09	3.96
256	242.048	1.201E-10	3.96	473.159	1.168E-10	3.99
1024	2518.815	8.193E-12	3.87	4545.861	7.327E-12	3.99
4096	23756.062	6.602E-13	3.63	40915.044	4.612E-13	3.99

Table 5.6: Simulation results with Q_3 elements.

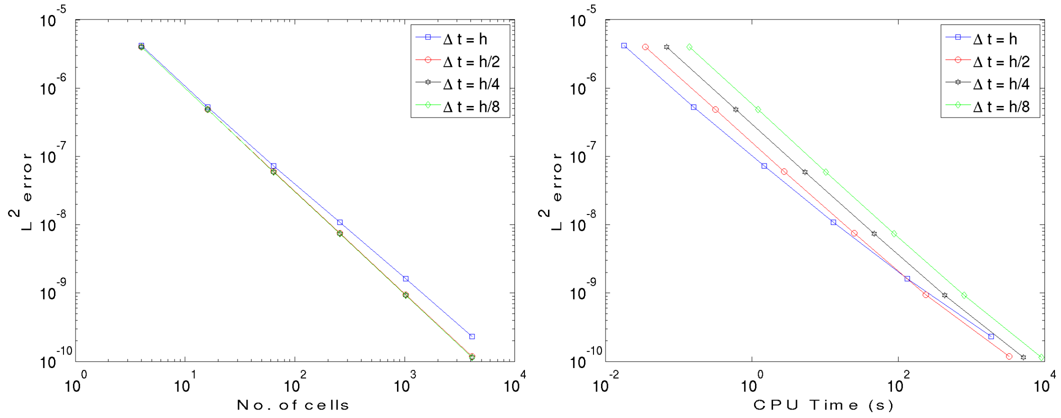

(a) (b)

Figure 5.2: L^2-error as a function of h and *CPU time* respectively for the four categories of time steps considered using Q_2 elements.

No of cells	Q_1 elements			Q_2 elements		
	CPU(s)	L^2 error	Order	CPU(s)	L^2 error	Order
4	0.014997	4.849E-02	-	0.044993	4.588E-03	-
16	0.098984	1.580E-02	1.62	0.366944	5.345E-04	3.10
64	0.839872	4.278E-03	1.88	3.164518	6.517E-05	3.04
256	6.957943	1.092E-03	1.97	26.927907	8.092E-06	3.00
1024	58.614089	2.745E-04	1.99	226.9405	1.010E-06	3.00
4096	478.420269	6.873E-05	2.00	2144.53698	1.262E-07	3.00

Table 5.7: Simulation results with Q_1 and Q_2 elements for the nonlinear example at $T = 1.0\ s$.

4 elements given by partitioning the square equally. We continue with uniform refinement i.e., cutting each square into four smaller similar ones.

The simulation is conducted upto time $T = 1.0\ s$ at which the L^2 error and CPU time are measured and listed in Tables 5.7 as well as 5.8. The time step is taken to be $\Delta t = 0.1h$. We use a local polynomial approximation of order k upto $k = 3$. Clearly, we observe that h^{k+1} order of accuracy is achieved. Similarly, we present the variation of L^2 error with CPU time in Figure 5.3. For instance, one can observe from Figure 5.3 that after $0.5\,s$ the error for Q_3 elements is much better than that for Q_1 elements. Moreover, the same error obtained with Q_3 elements after $0.5\,s$ can be realized with Q_1 elements after a computational time of over $100\,s$.

No of cells	CPU(s)	L^2 error	Order
4	0.112982	4.602E-04	-
16	1.084835	3.175E-05	3.86
64	9.828505	2.046E-06	3.96
256	82.375477	1.297E-07	3.98
1024	749.510057	8.33E-09	3.96
4096	6301.15608	5.7E-10	3.87

Table 5.8: Simulation results with Q_3 elements for the nonlinear example at $T = 1.0\ s$.

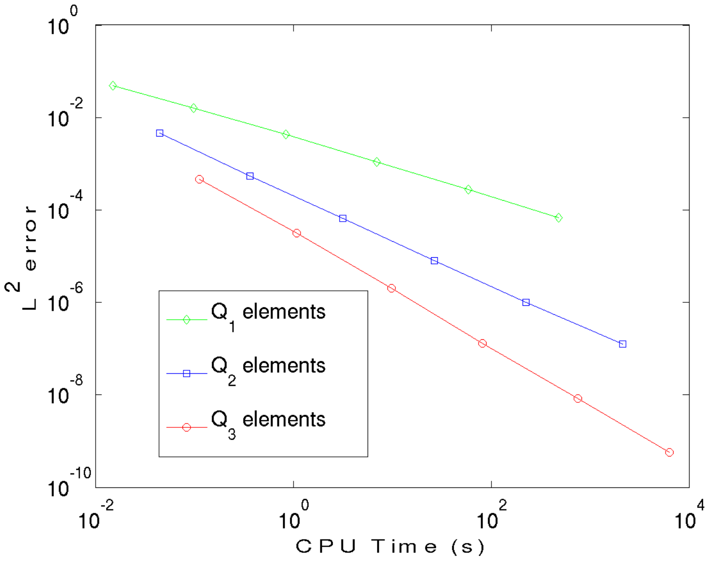

Figure 5.3: Plot of L^2 error with CPU time for Q_1, Q_2 and Q_3 elements. Simulation time $T = 1.0\ s$.

5.3 Numerical tests on a 2×2 system

In this section, we present numerical results for a 2×2 reaction-diffusion system that was used to test our DG code for systems of parabolic equations. We considered the Schnakenberg system whose numerical results are well known, see e.g., Zhu [162]. It is a classical example for the testing of numerical methods for reaction-diffusion equations, see e.g., [87, 104, 103, 141]. This system, see Schnakenberg [143], has been used to model the spatial distribution of a morphogen, e.g., the distribution of calcium in the hairs of the whorl in *Acetabularia*, see [71]. The Schnakenberg system has the form

$$\begin{aligned} \partial_t C_a - D_1 \Delta C_a - \kappa(a - C_a + C_a^2 C_i) &= 0 \text{ in } \Omega, \\ \partial_t C_i - D_2 \Delta C_i - \kappa(b - C_a^2 C_i) &= 0 \text{ in } \Omega, \end{aligned}$$

where C_a and C_i denote the concentration of activator and inhibitor respectively, D_1 and D_2 are diffusion coefficients, κ, a and b are rate constants of the biochemical reactions. We follow the set up in Zho [162] and take the initial and boundary conditions as follows

$$\begin{aligned} C_a(x, y, 0) &= a + b + 10^{-3} \exp^{-100((x-\frac{1}{3})^2 + (y-\frac{1}{2})^2)}, \\ C_i(x, y, 0) &= \frac{b}{(a+b)^2}, \\ \nabla C_a \cdot \mathbf{n} &= \nabla C_i \cdot \mathbf{n} = 0 \text{ on } \partial\Omega. \end{aligned}$$

The parameter values are $\kappa = 100,\ a = 0.1305,\ b = 0.7697,\ D_1 = 0.05,\ D_2 = 1$ and we do our computations on the unit square domain $\Omega =]0, 1[^2$.

First, we study the performance and convergence order in time for the SWIP method using Q_1 elements. The time stepper here is the ROWDA method, see Lang [98], which is of order 3 with 3 internal stages. We list in Table 5.9 the CPU time, L^2 error and order of accuracy for this simulation. In this case, we fix the grid resolution with 1024 elements and 1089 nodes. The error at Δt is measured as a difference between the solutions $C_{a,\Delta t}$ and $C_{a,2\Delta t}$ for time step $2\Delta t$ at $T = 1\,s$, i.e.,

$$E_{\Delta t} = \|C_{a,\Delta t} - C_{a,2\Delta t}\|_{L^2(\Omega)}.$$

The DG method of SWIP clearly shows a third order accuracy in time as expected. Next, we give the time evolution plots of concentrations of activator C_a and inhibitor C_i in Figures 5.4 and 5.5 respectively. These sumulation results of the Schnakenberg model compare very well to the known results, see e.g., Zho [162]. We were therefore convinced that our DG code could accurately handle the calcium model.

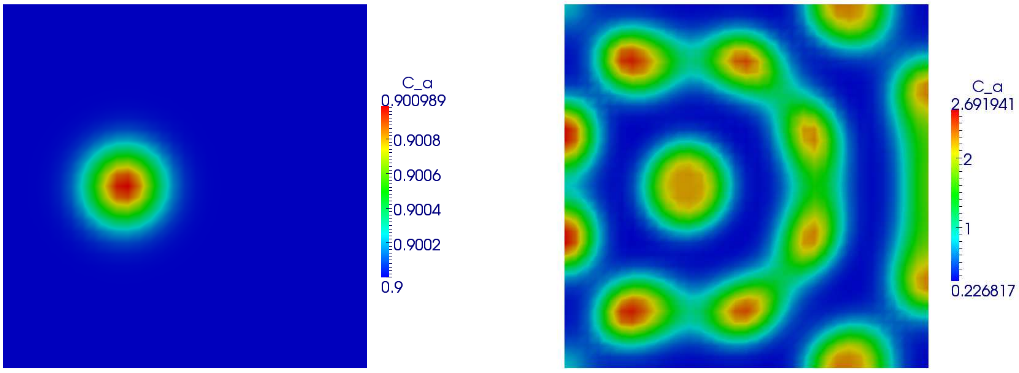

(a) t=0.0 s (b) t=0.5 s

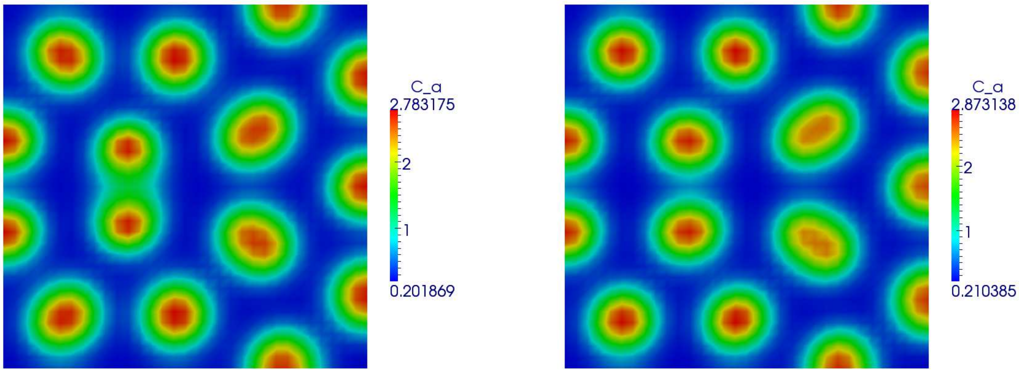

(c) t=1.0 s (d) t=2.0 s

Figure 5.4: Numerical solution of the Schnakenberg model. Contour plots of time evolution of the concentration of the activator C_a. Number of cells = 1024, dof = 4096.

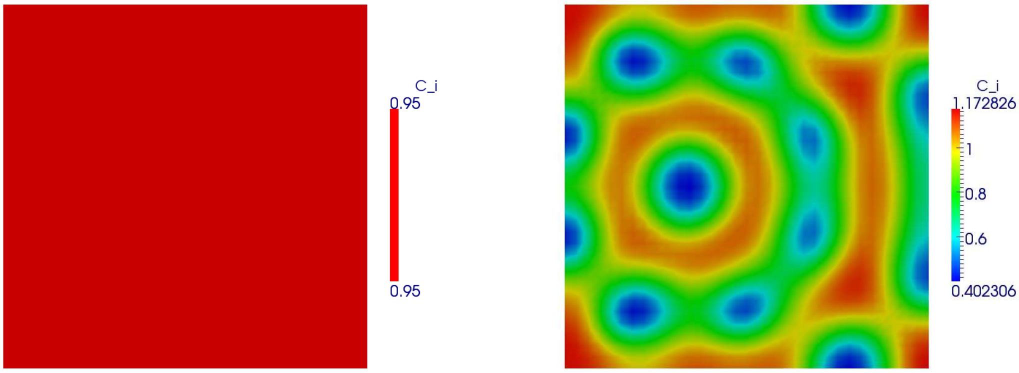

(a) t=0.0 s

(b) t=0.5 s

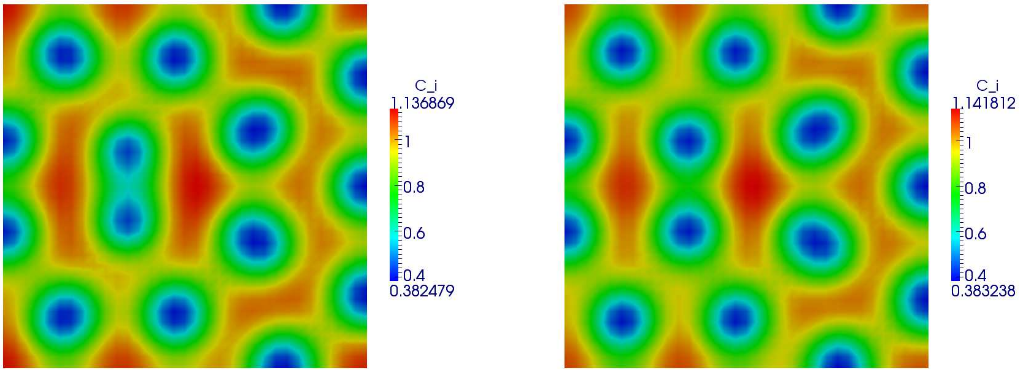

(c) t=1.0 s

(d) t=2.0 s

Figure 5.5: Numerical solution of the Schnakenberg model. Contour plots of time evolution of the concentration of the inhibitor C_i. Number of cells = 1024, dof = 4096.

Δt	CPU (s)	L^2 error	Order
4e-03	26.68	1.75596e-04	-
2e-03	49.54368	1.9412e-05	3.18
1e-03	96.24448	2.22149e-06	3.13
5e-04	183.5008	2.70146e-07	3.03
2.5e-04	364.43136	3.0107e-08	3.13
1.25e-04	698.10432	4.3349e-09	2.80

Table 5.9: CPU time, L^2 error and order of accuracy for the SWIP applied to the Schnakenberg model using the ROWDA method at $T = 1.0\,s$.

5.4 Generation of initial unstructured grids

In this section, an overview of the spatial resolution of the computational domain is explained. Due to the channel opening/closing, the spatially localized source terms are present and a fine/coarse spatial resolution around the channel is mandatory. The fine spatial resolution of the total computational domain puts high demand on the memory as well as computational time for the problem under consideration. To resolve this issue, we use highly unstructured simplicial grids in our computations. In fact, we put more nodal points within the pore of channels and take a sufficiently coarse mesh remote from the channels. Moreover, a spatially exponential decay function is used to generate the fine meshes within the channel area.

In [114, 115], multiple channels in a cluster were generated by simply increasing the radius of each channel. In this work, we have implemented a novel criterion for generating multi clusters and multi channels in the 2D grid. In our simulations we assumed that the radius of the channel pore is 12 *nm* so that we generate a grid length which is smaller than 2 *nm* within the area of the pore and we increase the grid length up to several tens of *nm* far from the channel area. We refine the grid until the smallest edge is less than a nano meter at the channel location by increasing the number of refinement levels. In this way, we ensure the fine resolution mesh around the channel pore. For a single cluster single channel simulations, the complete mesh and its zoom within the cluster is shown in Figure 5.6. The grid information for the various levels of refinement for this set up is given in Table 5.11. Similarly, the adaptive mesh for a single cluster and 64 clusters set up is shown in Figures 5.7(a) and 5.7(b) respectively, where each cluster consists of 25 channels. The program was developed to generate the adaptive grid for the placement of clusters on the computational domain.

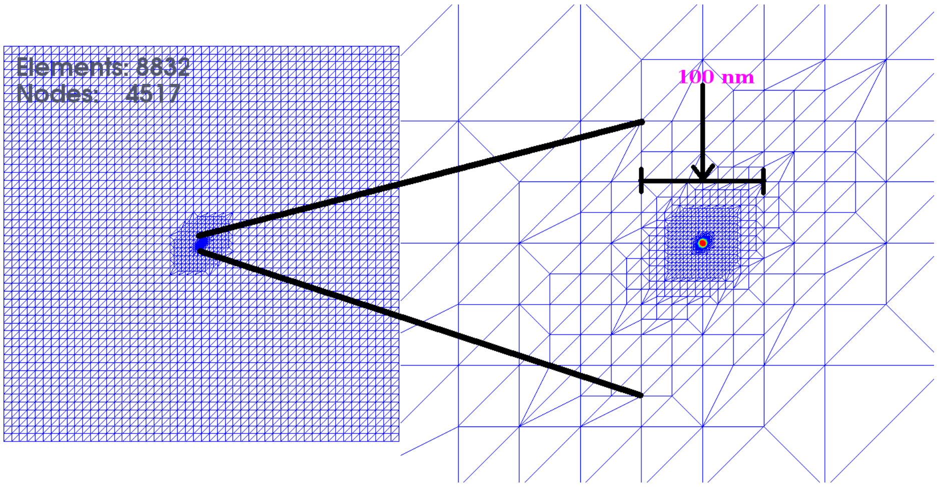
Elements: 8832
Nodes: 4517
100 nm

Figure 5.6: the spatial grid for one cluster, one channel and its zoom.

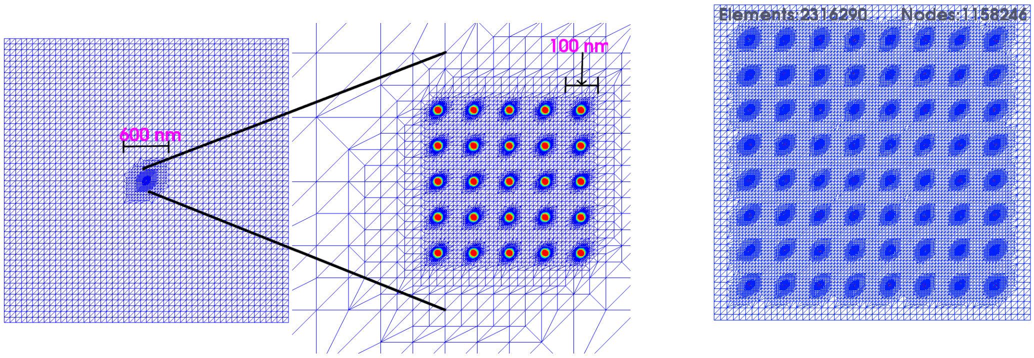
600 nm
100 nm
Elements:2316290
Nodes:1158246

(a) (b)

Figure 5.7: **a:** the spatial grid for one cluster and 25 channels and its zoom, **b:** the spatial grid for 64 clusters and 25 channels in each cluster.

5.5 Numerical tests for the deterministic model

5.5.1 Opening and closing results

In this subsection, we present the numerical results based on the deterministic opening and closing of one channel in one cluster arrangement. First, we compare the performance of the DIRK and ROWDA time integrators for a single channel in one cluster where the channel is opened for 0.5 seconds and the temporal tolerance is fixed at 10^{-06}. We check for computational efficiency and convergence of the cytosolic calcium to the steady state solution. Our results for this investigation are shown in Figures 5.8 (a) and (b). The simulation times for ROWDA and DIRK methods are 1746.88 s and 4780.48 s respectively for a level 9 grid with P_1 elements. Results including higher order elements are shown in Figure 5.8 (b). It is clearly seen that the convergence of the solution is almost the same for both P_1, P_2, and P_3 elements. In addition, the results validate the claim by Falcke [64], that when a channel opens, Ca^{2+} concentration increases in the cytosol and decrease in the ER until a stationary state is reached when free Ca^{2+} has spread far enough so that removal of Ca^{2+} from the cytosol back into the ER balances the flux through the channel. Clearly, we can see from Figure 5.8 that this stationary state is attained in approximately 0.03 s. Moreover, we see that the ROWDA method is computationally more efficient than the DIRK method. Based on this result, we adopted the ROWDA method for our subsequent computations particularly for the calcium model.

Secondly, we consider the fundamental problem with DG methods concerning their high computational and storage cost. This is partly because they require more degrees of freedom than other methods, but mainly due to the wide nodal stencils which result in very large ill-conditioned Jacobian matrices in implicit solvers, see e.g., Persson and Peraire [125]. We investigated this challenge with mainly two linear solvers, i.e., the conjugate gradient (CG) and the bi-conjugate gradient stabilized (BiCGSTAB) solvers with four preconditioners, i.e. Algebraic Multigrid (AMG)[22], Jacobi, Symmetric Successive Over Relaxation(SSOR) and a preconditioner based on a coarse scale correction with post-smoothing based on a block incomplete LU factorization with zero fill-in of the Jacobian matrix (ILU0)[125]. The performance of different combinations in terms of computational time for a temporal tolerance of 10^{-03} are shown in Table 5.10. As can be seen from the table, the AMG preconditioner performed better for this system with a gain of 33% for the CG and BiCGSTAB solvers using the SWIPG method as compared to the ILU0. For the NWIPG and IWIPG methods, the combination of BiCGSTAB solver and AMG resulted in a gain of 35% and 29% respectively as compared to the ILU0. Moreover, as is expected, the CG solver worked for the SWIPG method where the matrix in (4.29) is symmetric, but did not work for the NWIPG and IWIPG methods. Note that the CG method is one of the best known iterative technique for solving sparse

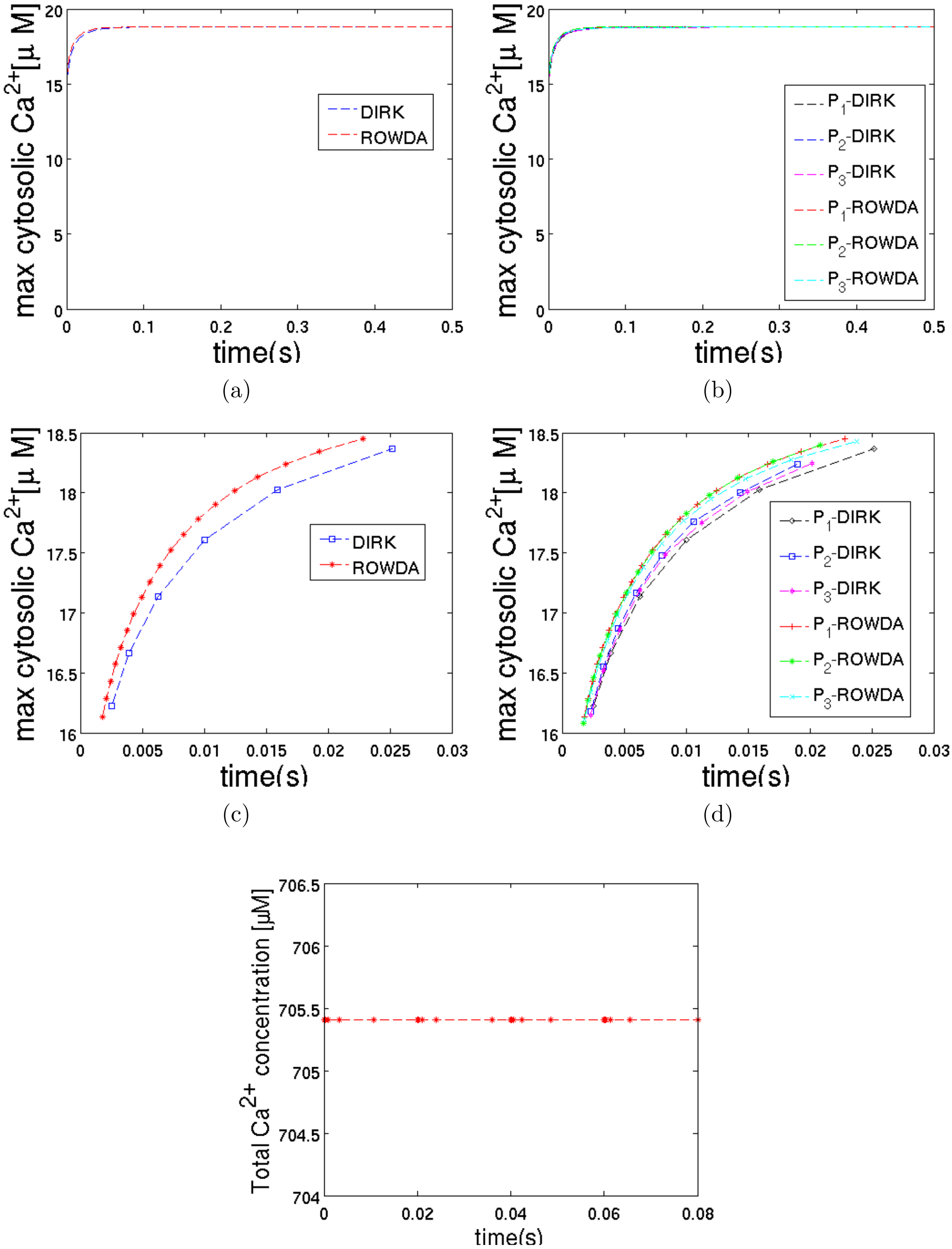

(a) (b)

(c) (d)

(e)

Figure 5.8: Comparison of the DIRK and ROWDA methods for a single channel opened for 0.5 s for the level 9 grid. (a): maximum cytosolic Ca^{2+} with P_1 elements, (b): maximum cytosolic Ca^{2+} with P_1, P_2 and P_3 elements, (c) and (d): zoom of (a) and (b) respectively, (e): total concentration.

symmetric positive definite linear systems, see e.g. Saad [142, Sect. 6.7]. An attempt to try it for the NWIPG and IWIPG methods failed.

Linear Solver	Preconditioner	CPU Time (s)		
		SWIPG	NWIPG	IWIPG
CG Solver	AMG	2790.08	-	-
	ILU0	4164.33	-	-
	SSOR	12799.4	-	-
	Jacobi	7209.5	-	-
BiCGSTAB Solver	AMG	425.96	406.66	631.44
	ILU0	635.761	625.63	889.64
	SSOR	1341.55	1359.32	1925.54
	Jacobi	2215.07	1419.74	1925.93

Table 5.10: Comparison of linear solvers and preconditioners in terms of CPU time for the DG methods SWIPG, NWIPG and IWIPG.

Next, we present numerical results to analyze the numerical convergence of solutions for the DG method SWIP where $P_1, P_2,$ and P$_3$ elements are used at varied grid levels. In this regard, we present simulation results based on the different spatial grid resolutions. The spatial grids were generated adaptively by placing more points within and at the neighborhood of a channel as discussed in Section 5.4. We perform tests based on different refinement levels from level 7 to level 12. Information on the levels of grids used is summarised in Table 5.11. The channel is opened and closed twice after 0.02 seconds respectively. The maximum cytosolic Ca^{2+} for P_1 elements is shown in Figure 5.9(a). Clearly, the numerical convergence of accurate solution is attained from grid level 9 onwards. A comparison with P_2 and P_3 elements is shown in 5.9(b). From Figure 5.8(e), we see that mass is conserved. We attribute this to the high level of accuracy of the DG method coupled with local mass conservation which we used in order to not loose concentration. Equally important are the average values of cytosolic Ca^{2+} and ER Ca^{2+} shown in Figures 5.10 (a) and (b). The average of the solution is computed using the following formula

$$\bar{u} = \frac{1}{|\Omega|} \int_{\Omega} u(x)\, dx,$$

where $u(x)$ is the numerical solution over the domain. We see that the average value of cytosolic Ca^{2+} does not fall below the initial cytosolic Ca^{2+} concentration when the channel is closed, which agrees well with experiments, see e.g., Falcke [64]. Similarly, we present the average values of mobile and stationary buffer concentrations in Figure 5.11 (a) and (b) respectively.

In addition, in Figure 5.12, we give the spatial profile of free cytosolic Ca^{2+}

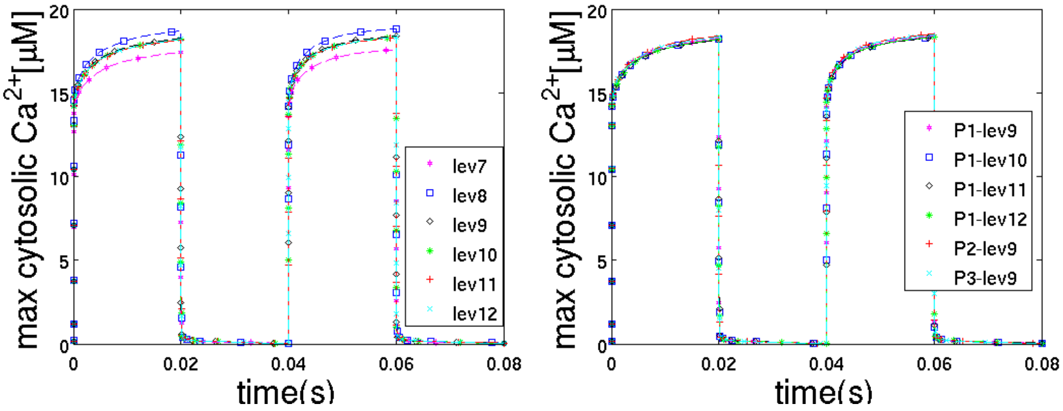

(a) (b)

Figure 5.9: The maximum value of cytosolic Ca^{2+} with P_1 elements in (a) and higher order elements included in (b) when a channel open and closes twice.

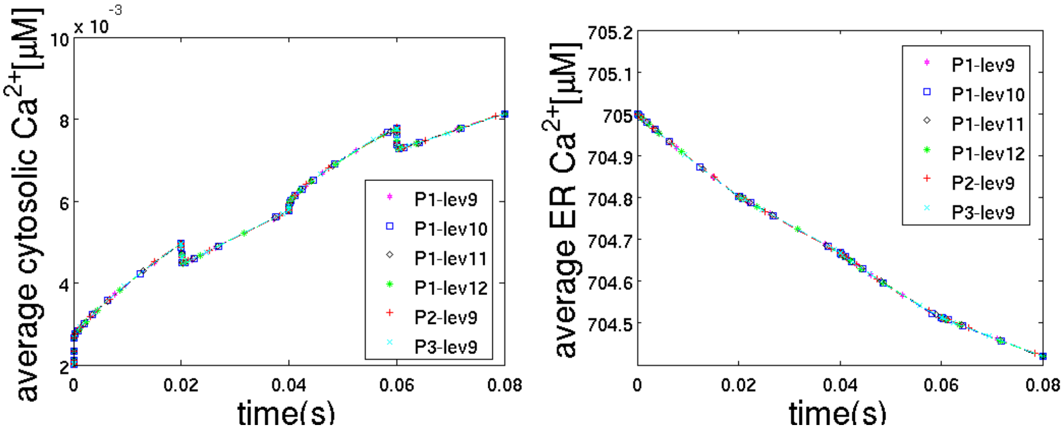

(a) (b)

Figure 5.10: The average values of cytosolic and ER Ca^{2+} concentration in (a) and (b) respectively for opening and closing of one channel till $t = 0.08$ s.

Level	No. of Elements	No. of Nodes	Smallest edge (μm)	Dof
7	7,760	3,981	5.625E-03	93,120
8	8,052	4,127	2.8125E-03	96,624
9	8,832	4,517	1.40625E-03	105,984
10	10,988	5,595	7.03125E-04	131,856
11	17,888	9,045	3.51562E-04	214,656
12	42,612	21,407	1.75781E-04	511,344

Table 5.11: Grid information for the various grids used in the one cluster one channel simulation

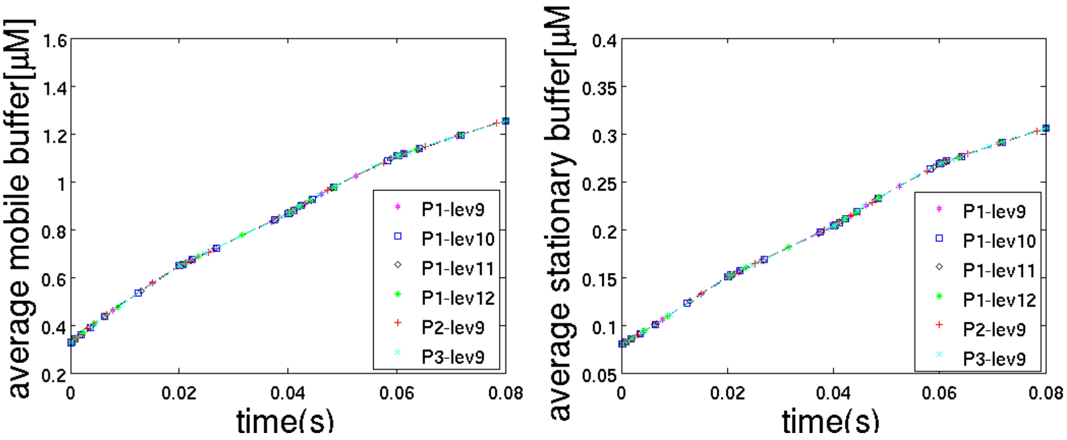

(a) (b)

Figure 5.11: The average values of mobile and stationary buffer concentration in (a) and (b) respectively for opening and closing of one channel till $t = 0.08\ s$.

around the channel area at different time levels of deterministic channel transition. Similar contour plots are also given in Figure 5.13.

Finally, we study the convergence order in time for the SWIP method for a single channel opened till $T = 10^{-4}\, s$. We list in Table 5.12 the L^2 error and order of accuracy for this simulation. In this case, the spatial resolution is fixed at grid level 9 with 8,832 elements and 4,517 nodes. The error at Δt is measured as a difference between the solutions $c_{\Delta t}$ and $c_{2\Delta t}$ for time step $2\Delta t$ at $T = 10^{-4}\, s$, i.e.,

$$E_{\Delta t} = \|c_{\Delta t} - c_{2\Delta t}\|_{L^2(\Omega)}.$$

The DG method of SWIP clearly shows a third order accuracy in time as expected.

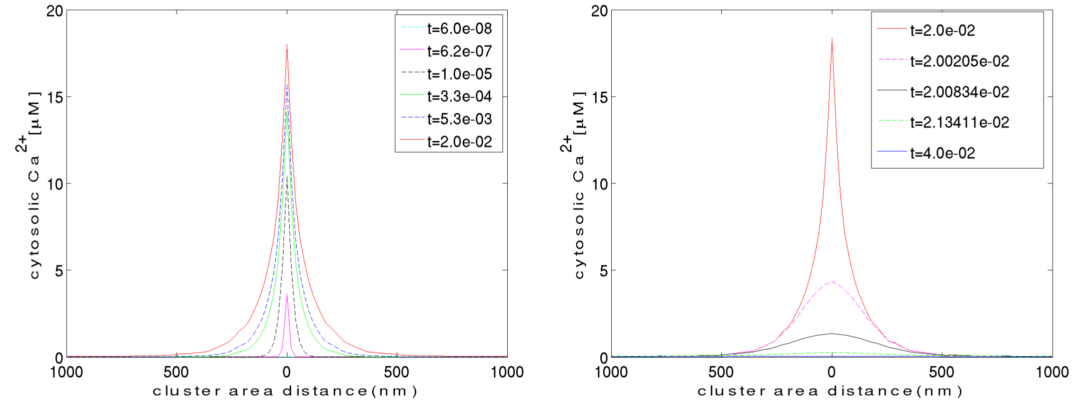

(a) (b)

Figure 5.12: Plot of the spatial profile of free cytosolic Ca^{2+} at different time levels of a channel opening and closing in (a) and (b) respectively.

Δt	L^2 error	Order
1e-07	2.44092e-08	-
5e-08	3.14432e-09	2.96
2.5e-08	2.68131e-10	3.55
1.25e-08	4.0478e-11	2.73

Table 5.12: L^2 error and order of accuracy for the SWIP for a single channel opened till 10^{-4} s.

5.5.2 DG vs FEM solutions

One fundamental property that naturally comes with DG methods is the conservation of mass on each mesh element, see e.g., Riviére [134, p. 41]. Besides, since DG methods allow elementwise formulations, they are well known to capture all discontinuities in the computational domain. Because of this property, we expect the DG method to accurately handle channel transitions in the channel area where the Ca^{2+} flux is discontinuous when channels open. We performed some numerical tests with both the DG method and FEM for deterministic channel transitions. The first test involved performing simulations on the same meshes for the two methods. In this scenario, we also use the same parameters as well as temporal and linear solver tolerances which have been fixed at 5×10^{-03} and 2×10^{-05} respectively. For the FEM computations, we first check for the numerical convergence of accurate solution in a similar manner as for the DG case, see Figure 5.9(a). The maximum cytosolic Ca^{2+} using P_1 elements is shown in Figure 5.14, which depicts a similar pattern as for the DG case.

For meaningful comparison of the two methods, we performed simulations on

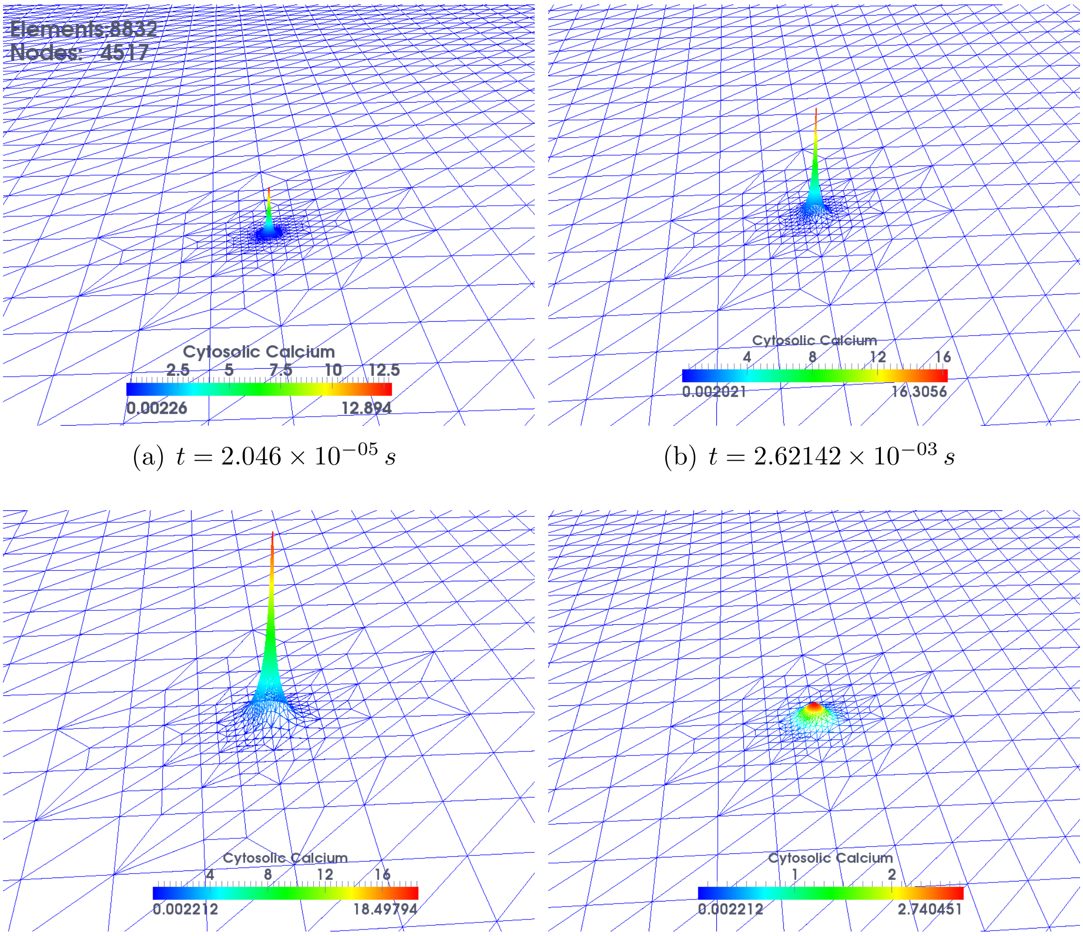

(a) $t = 2.046 \times 10^{-05}\,s$

(b) $t = 2.62142 \times 10^{-03}\,s$

(c) $t = 2.0 \times 10^{-02}\,s$

(d) $t = 2.00415 \times 10^{-02}\,s$

Figure 5.13: Cytosolic Ca^{2+} concentration for opening of a channel for $0.04\,s$ at times $2.04 \times 10^{-05}, 2.62 \times 10^{-03}, 2.0 \times 10^{-02}\,s$ respectively and at time $2.00415 \times 10^{-02}\,s$ when the channel is closed. Here, mesh level 9 which consists of 8,832 elements and 4,517 nodes has been used.

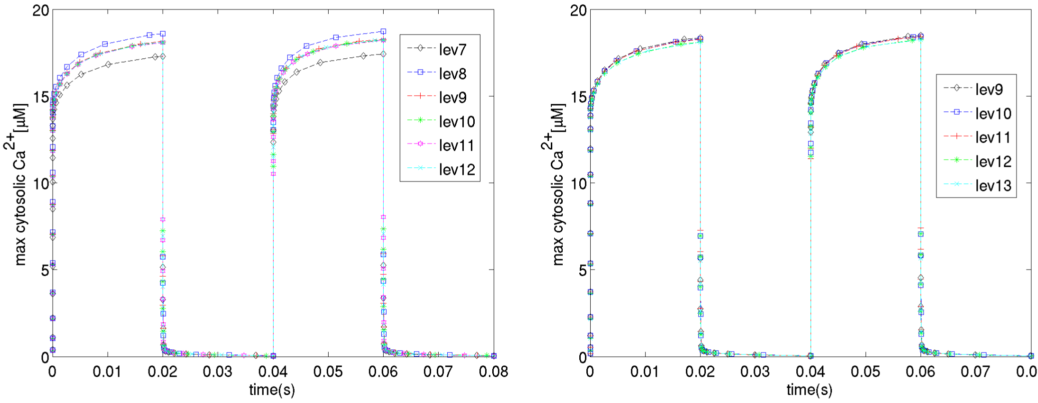

(a) (b)

Figure 5.14: The maximum value of cytosolic Ca^{2+} with P_1 elements for the FEM when a channel open and close twice till $t = 0.08\ s$.

different grid levels, where we took a more coarser grid for DG as compared to FEM in the cluster region. We therefore considered a mesh level 9 for DG and level 12 for FEM. As shown in Table 5.11, the level 9 mesh consists of 8,832 elements and 4,517 nodes where the smallest edge size is $1.40625\,nm$. The 12th level mesh consists of 46,612 elements, 21,407 nodes and in this case the smallest edge size is $0.175781\,nm$. The level 9 grid yields 105,984 dof with DG method, while the level 12 grid results in 85,628 dof with FEM for all the four components. We display the maximum cytosolic Ca^{2+} using P_1 elements in Figure 5.15(a). In this simulation, the CPU time for the DG method is $635.761\,s$ while that for the FEM is $635.007\,s$. One observes that the maximum solution for the DG is higher than that for FEM. We attribute this gain to the high level of accuracy of the DG method coupled with the local mass conservation which we used in order to not loose concentration.

The next numerical test considered for the two methods was to take an initial coarse mesh of 25 × 25 for the DG case and 50 × 50 mesh for the FEM case. We then employed the same adaptive strategy in Section 5.4 to refine the grids. Here, we fix the DG mesh at level 10 and the FEM mesh at level 11. This choice gave a favourable comparison in terms of dof. We present results for the the maximum cytosolic Ca^{2+} using P_1 elements in Figure 5.15(b). We mention here that for both cases, convergence of accurate numerical solutions were achieved at level 8 grid. In this case, the DG grid consists of 4,104 elements, 2,103 vertices, 49,248 dof and the CPU time is $296.517\ s$. Similarly the FEM grid contains 16,608 elements, 8,405 vertices, 33,620 dof, and the CPU time is $114.887\ s$. From these tests, one deduces that high accuracy and computational efficiency can be achieved with DG methods on coarser meshes as compared to FEM.

The last investigation considered for the two methods was to compare the so-

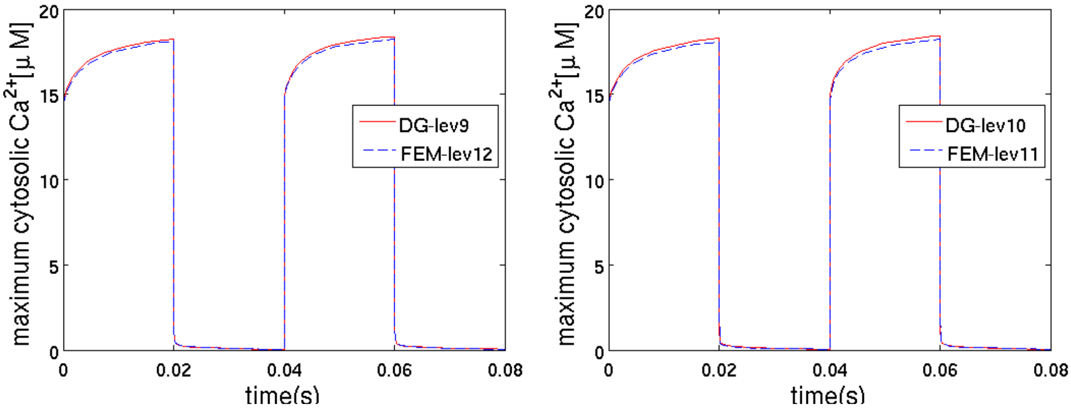

(a) (b)

Figure 5.15: The maximum value of cytosolic Ca^{2+} with P_1 elements for DG method and FEM when a channel open and close twice. In (b), DG coarse grid is 25×25 while FEM coarse grid is 50×50.

lutions at the cluster region. For this test, we give a plot of the spatial profile of free cytosolic Ca^{2+} for one channel opened for $0.02\,s$ in Figure 5.16. Even though both solutions look similar, a plot of the difference between them shows that the DG solution is higher within the channel radius.

5.5.3 Parallel efficiency test

Here, we briefly demonstrate the parallel implementation to solve the deterministic system for a multi-cluster and mult-channel arrangement. The essence of parallel numerical simulation is to distribute the computational load evenly on all processors based on the domain decomposition algorithms. We developed our code based on the software package DUNE [21], especially the DUNE-PDELab discretization module. The parallel linear solvers depend on the DUNE-ISTL module. The BiCGSTAB [156] method with ILU0 preconditioning is used as the linear solver. Moreover, the external parallel UG grid [20] interface is used for parallel grid constructions, which supports overlapping grids with an allowance of one layer of ghost elements at the processor boundaries.

In this subsection, the strong scaling properties of the DG method is presented for polynomial degree one. The simulations are done based on the 64 cluster setup where each cluster consists of 25 channels. The computational mesh consists of 1,102,734 elements and 551,468 nodes which yields 13,232,808 degrees of freedom for polynomial degree one in the simulation. In this benchmark, the parallel efficiency is demonstrated for opening of all channels in all clusters for 5 time steps where

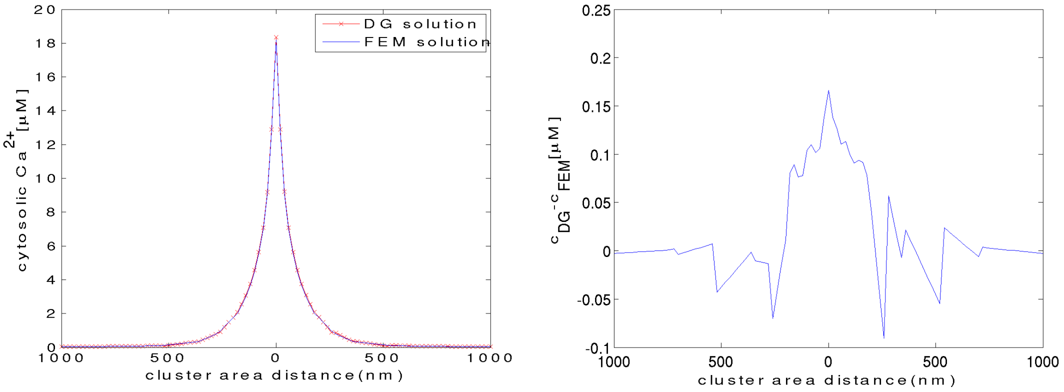

(a) (b)

Figure 5.16: (a) Plot of the spatial profile around the cluster area, of free cytosolic Ca^{2+} for the DG method and FEM for an open channel at $t = 0.02\,s$, (b) Plot of the difference between the two solutions in (a).

the time step size is fixed at $\tau = 10^{-6}$. The benchmarks were performed using a 80 core linux cluster (HP ProLiant DL980G7), 8x 10 Core Intel Xeon E7 4870 CPU (overall 80 cores), clocked at 2.40 GHz and has 1 TB RAM at RICAM, Linz, Austria. Here, the strong scalability tests are performed up to 64 cores. The computational execution times were recorded for the opening of all channels which is the most expensive, in terms of solver time during the channel transition. *Parallel efficiency* was computed as

$$e = \frac{1}{N}\frac{T_1}{T_N}$$

where T_1 is the total CPU time of a reference simulation on one core. Furthermore, N and T_N are number of cores and total CPU time on N cores respectively.

The domain decomposition of the 64 cluster mesh on 64 cores is shown in Figure 5.17. The parallel efficiency results are illustrated in Table. 5.13. Here the first column represents the number of cores (N) used in the simulations. In the second column, the average left hand side matrix assembly time (MAT) over all time steps is shown. For the polynomial degree one, the assembling of the matrix is scaled up to 87% on 64 cores compared with assembling of matrix on one core. The third column denotes the average linear solver iterations (AIT) over all internal stages and all time steps. We can observe that the linear solver takes more iterations over increasing the number of cores, which is typical for the ILU0 preconditioner in overlapping decomposition of domain simulations. The next two columns show the average total computational time (ATS) of the linear solver to perform an internal stage of the ROWDA method and average computational time for one iteration of linear solver (ATIT) respectively. Finally, the next two columns represents the total simulation

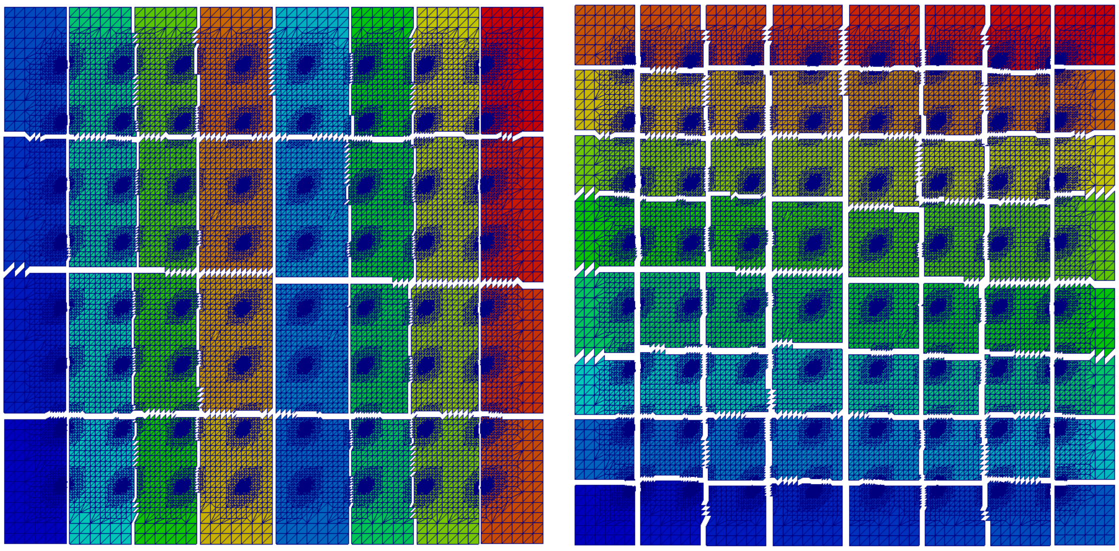

(a) on 32 cores (b) on 64 cores

Figure 5.17: The mesh decomposition on different processors. Different colours show parts of the mesh assigned to different processors for multi-cluster arrangement.

time (TT) for the computation of 5 time steps and the parallel scalability of the TT respectively. Up to 64 cores adequate overall parallel efficiency of $E = 0.66$ could be achieved. We observed that by increasing N beyond 64 cores E dropped significantly for the overall computational time. We noticed that with increasing N, the relation between local computational work performed on inner nodes as well as the ghost nodes which are needed for one layer of overalapping grid of the computational domain and the data communication which are proportional to the size of shared domain interfaces, deteriorates, thus impeding any further efficient scaling.

In Figure 5.18, we display surface plots for simulations done on one core based

N	MAT(s)	AIT	ATS (s)	ATIT(s)	TT (s)	E
1	101.01	18	190.52	9.20	4576.53	-
2	53.12	19	98.60	5.03	2338.98	0.97
4	27.78	19	52.43	2.91	1278.76	0.91
8	14.02	20	27.49	1.65	654.08	0.87
16	7.12	21	14.37	0.92	339.30	0.84
32	3.61	21	7.70	0.61	210.07	0.78
64	1.81	23	4.55	0.38	107.83	0.66

Table 5.13: Comparison of parallel efficiency using different numbers of processors for solving the deterministic equations for multi-cluster set up.

on the 64 cluster set up, where each cluster consists of 25 channels. In this case all the channels are opened for $t = 0.02\,s$.

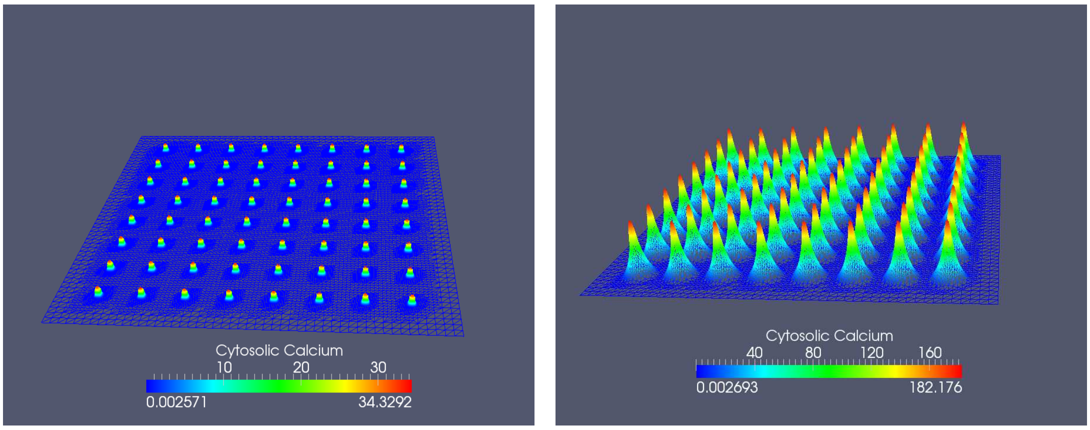

Figure 5.18: The contour plot for the cytosolic Ca^{2+} concentration for opening of all the 25 channels in each cluster of 64 cluster arrangement at times $t = 8.19 \times 10^{-05}\,s$ and $t = 2.0 \times 10^{-02}\,s$ respectively.

5.6 Numerical results for the hybrid model

In the previous sections, we presented numerical results where channel transition is treated as a deterministic process. In this section, we present simulation results for the hybrid stochastic and deterministic model. We first give results for one cluster that consists of 25 channels. Thereafter we present simulation results for 36 clusters with each cluster containing 25 channels. In our computations, we use the ROWDA method to solve the deterministic equations while the Gillespie algorithm is used to solve the stochastic part. Both are adaptive with regard to time stepping. The Gillespie method is adaptive in the sense that its time step follows the evolution of transition probabilities. In this hybrid model, we have used the hybrid algorithm presented in Nagaiah et al. [115], which we recall in Appendix B.

5.6.1 Numerical results with one cluster set up

In this subsection, the hybrid numerical results are shown based on the one cluster set up which consists of 25 channels. For this simulation we use the grid level 9 which contains 41,268 elements, 20,735 nodes and the degrees of freedom are 495,216 with P_1 elements. The simulations are done for $T = 4.5\ s$ of real simulation time. The CPU time for this simulation is about 48 days, 3 hours on a single core machine.

When a channel opens/closes, the concentration changes occur rapidly. In Figure 5.19(a), the maximum cytosolic Ca^{2+} concentration is initially constant when all channels are closed but quickly increases after approximately 0.6 s when channels begin to open. The concentration thereafter changes according to the random opening and closing of channels. In our computations, we begin with an initial time step of 10^{-08} s which increases till 10^{-03} s depending on the state of the channels. During this rapid change, the adaptive time step control plays a vital role to maintain the accuracy of the solution. The corresponding average cytosolic and ER Ca^{2+} concentrations, the average mobile and stationary buffer concentrations and the number of open channels are shown in Figures 5.19(b)-(f). For this simulation, we also present a contour plot of the cytosolic Ca^{2+} wave and the open channels in Figures 5.20 (a) and (b) respectively.

We can observe that the opening of channels occurs in a burst-like and stochastic manner. Notably, release of Ca^{2+} couples the gating dynamics of channels and stimulates the opening of almost all channels in the cluster. The recognizable release of Ca^{2+} lasts for several seconds and the dynamics is split into a first short spike and a long release tail. This finding shares its characteristics with long release events in cells, such as those observed during Ca^{2+} waves, see e.g., Falcke [64].

5.6.2 Numerical results for multi cluster set up

The numerical results of stochastic opening and closing of channels in an arrangement with many clusters are presented in this subsection. The main aim of the multi cluster set up is to study the bursting of calcium channels across the whole cell. We consider 36 clusters where each cluster consists of 25 channels. The fine mesh at level 8 used for the simulations comprise of 798,240 elements and 399,221 nodes, which result in 9,578,880 degrees of freedom with P_1 elements. We perform the simulation in parallel on 36 processors using the overlapping domain decomposition method illustrated in Section 4.7. As in Section 5.5.3, we also use the parallel UG grid interface [20], for the grid generation and domain decomposition.

To solve the linear system, we employ the parallel solver version of BiCGSTAB and ILU0 preconditioner designed for overlapping domain decompositions, which is available in DUNE [21]. Here, the simulations are done for $T = 1.0$ s of real simulation time. Initially, we assume that all channels are closed prior to the start of the simulation. The computations were performed using a 64 core linux cluster (Server HP DL585R07 CTC), clocked at 2.593 GHz and has 378 GB RAM at the Institute for Analysis and Numerics, Otto von Guericke University, Magdeburg, Germany.

A typical simulation execution is shown in Figure 5.21, which depicts the maximum and average value of cytosolic Ca^{2+} concentrations over the simulation time. In addition, Figure 5.22 shows the average values of ER Ca^{2+} concentration, mo-

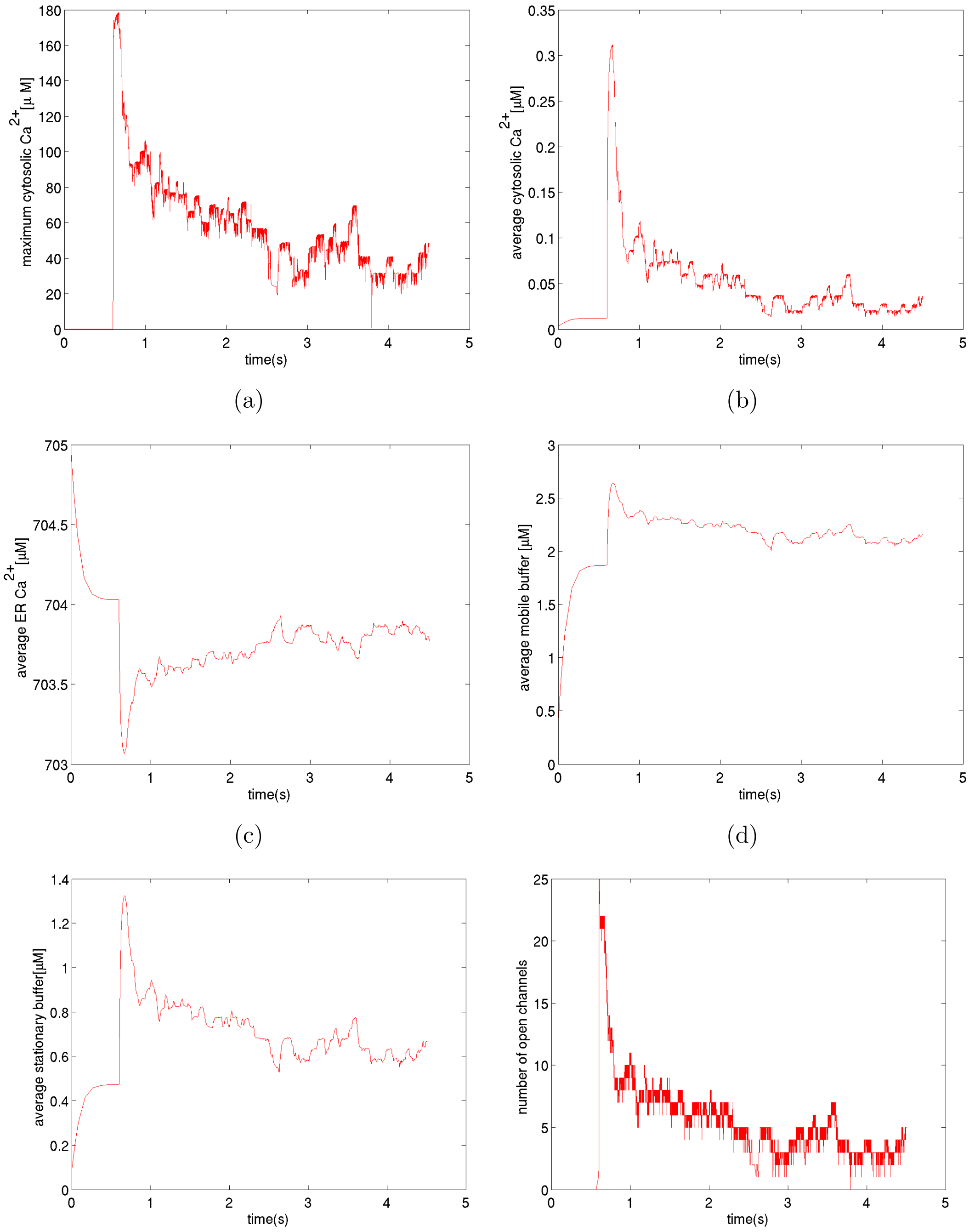

(a) (b)

(c) (d)

(e) (f)

Figure 5.19: The maximum and average values of cytosolic Ca^{2+} in (a) and (b), the average values of ER Ca^{2+}, mobile and stationary buffers in (c), (d), (e) and the number of open channels in (f) respectively for one cluster with 25 channels opening and closing stochastically till $T = 4.5$ s.

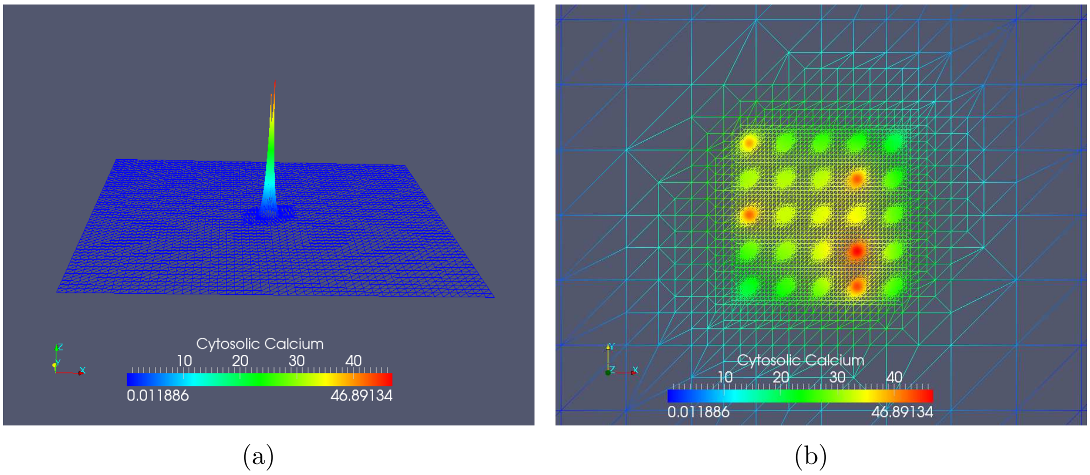

Figure 5.20: The contour plot for the cytosolic Ca^{2+} and a zoom for channels state in (a) and (b) respectively for stochastic opening and closing of channels at $t = 4.5\ s$.

bile buffer concentration, stationary buffer concentration, number of open clusters and number of open channels over the simulation time. During the hybrid stochastic simulations, the initial opening of a channel in the domain occurs at time $t = 0.0644401\, s$, see Figure 5.23(a). The maximum cytosolic calcium concentration then rises rapidly to 165(μM), see Figure 5.23(b). On the other hand, the average calcium concentration increases slowly based on how fast the calcium diffuses and the number of open channels on the domain. The released calcium diffuses to neighboring clusters slowly and it subsequently opens the channels in all the clusters on the domain, see the rest of the figures in Figure 5.23. The wave appears at time $t = 0.284055\, s$ when all the 36 clusters are open. The wave stagnates till time $t = 0.808044\, s$, then begins to terminate in some of the clusters, see Figure 5.22(d). We expect the wave to terminate completely after a few seconds when many channels in the clusters have closed.

The observed behavior corroborates the calcium-induced calcium release (CICR) mechanism described in Section 2.4. This recognizable aspect very much resembles the synchronized openings of channels in many clusters in oscillating cells. We remark that the Ca^{2+} concentration during release is large only in small domains around open channels. Therefore overall levels of Ca^{2+} in the cell remain small, see Figure 5.21(a), but they are sufficient to elicit the synchronized release in terms of cluster-to-cluster coupling, see e.g., Nagaiah [113].

The domain decomposition of the 36 cluster mesh on 28 and 64 cores is shown in Figure 5.24. The parallel efficiency results here are typically the same as the deterministic case described in subsection 5.5.3 and is given in Table 5.14.

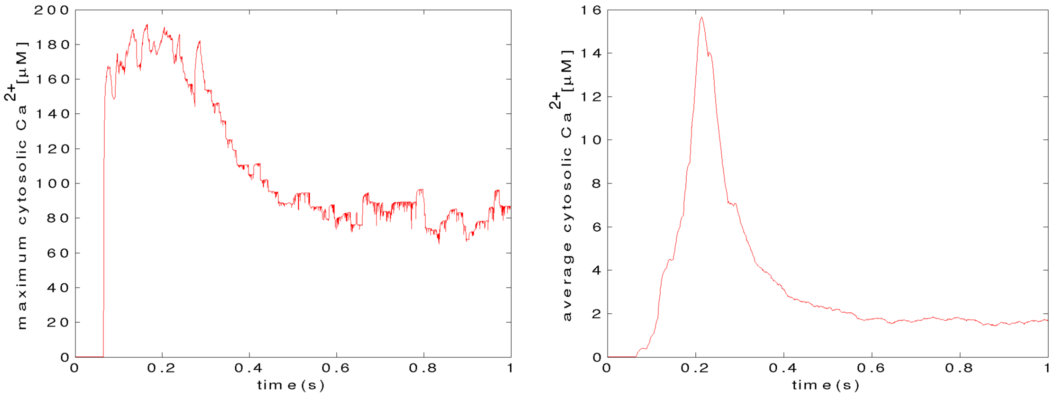

Figure 5.21: A plot of the maximum and average value of cytosolic Ca^{2+} concentrations over the simulation time for the multi-cluster setup for $T = 1.0s$.

N	MAT(s)	AI	ATS (s)	ATIT(s)	TT (s)	E
1	78.76	16	116.23	7.51	2682.27	-
2	41.08	17	61.17	3.97	1426.70	0.94
4	20.94	17	31.58	2.01	732.86	0.91
8	10.56	17	16.70	1.05	389.86	0.86
16	5.39	18	8.75	0.55	201.98	0.83
32	2.76	18	4.77	0.30	110.29	0.76
64	1.42	20	2.67	0.17	62.55	0.67

Table 5.14: Parallel efficiency for 36 cluster setup

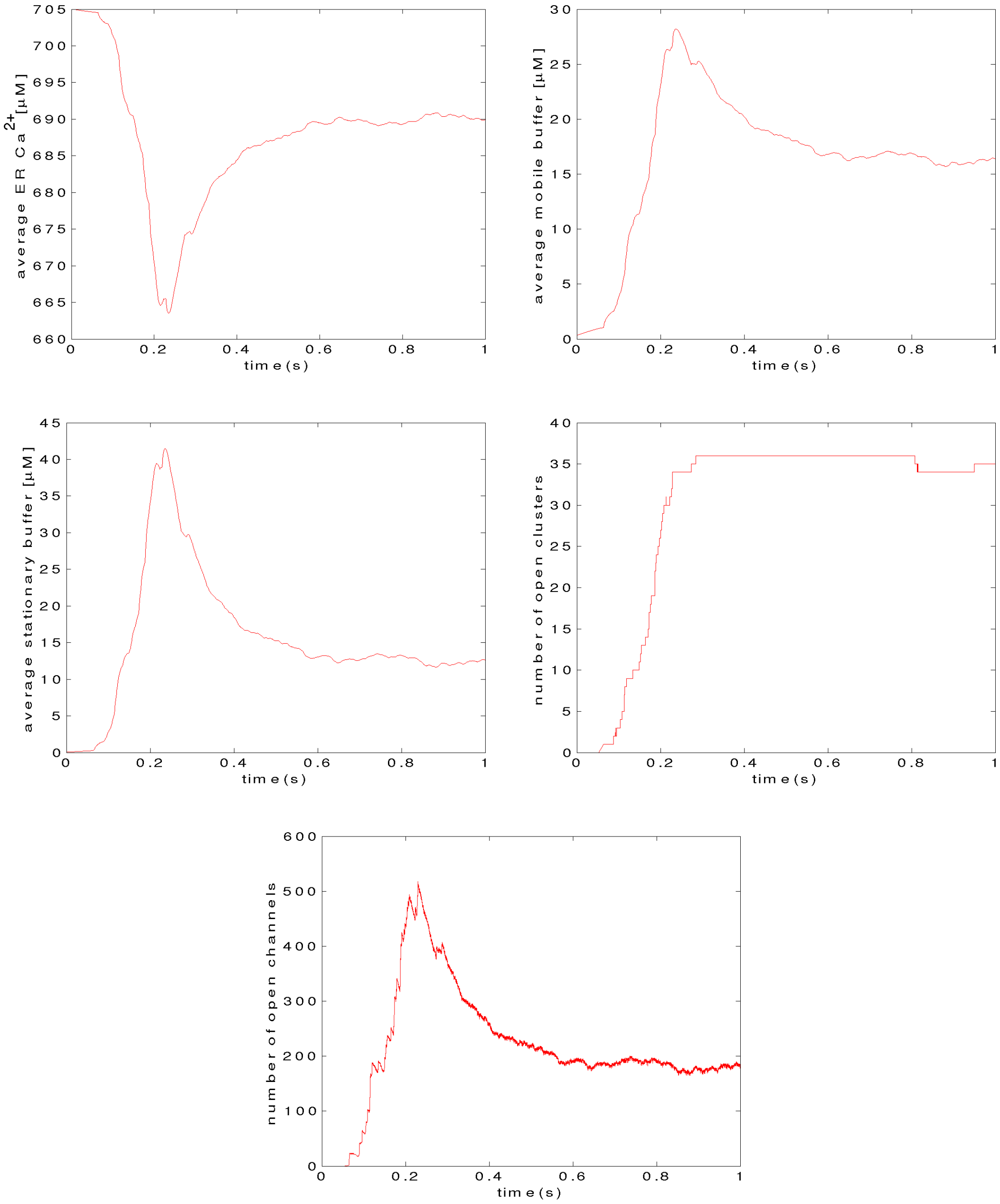

Figure 5.22: A plot of the average values of ER Ca^{2+} concentration, mobile buffer concentration, stationary buffer concentration, number of open clusters and number of open channels for the 36 cluster arrangement versus the simulation time.

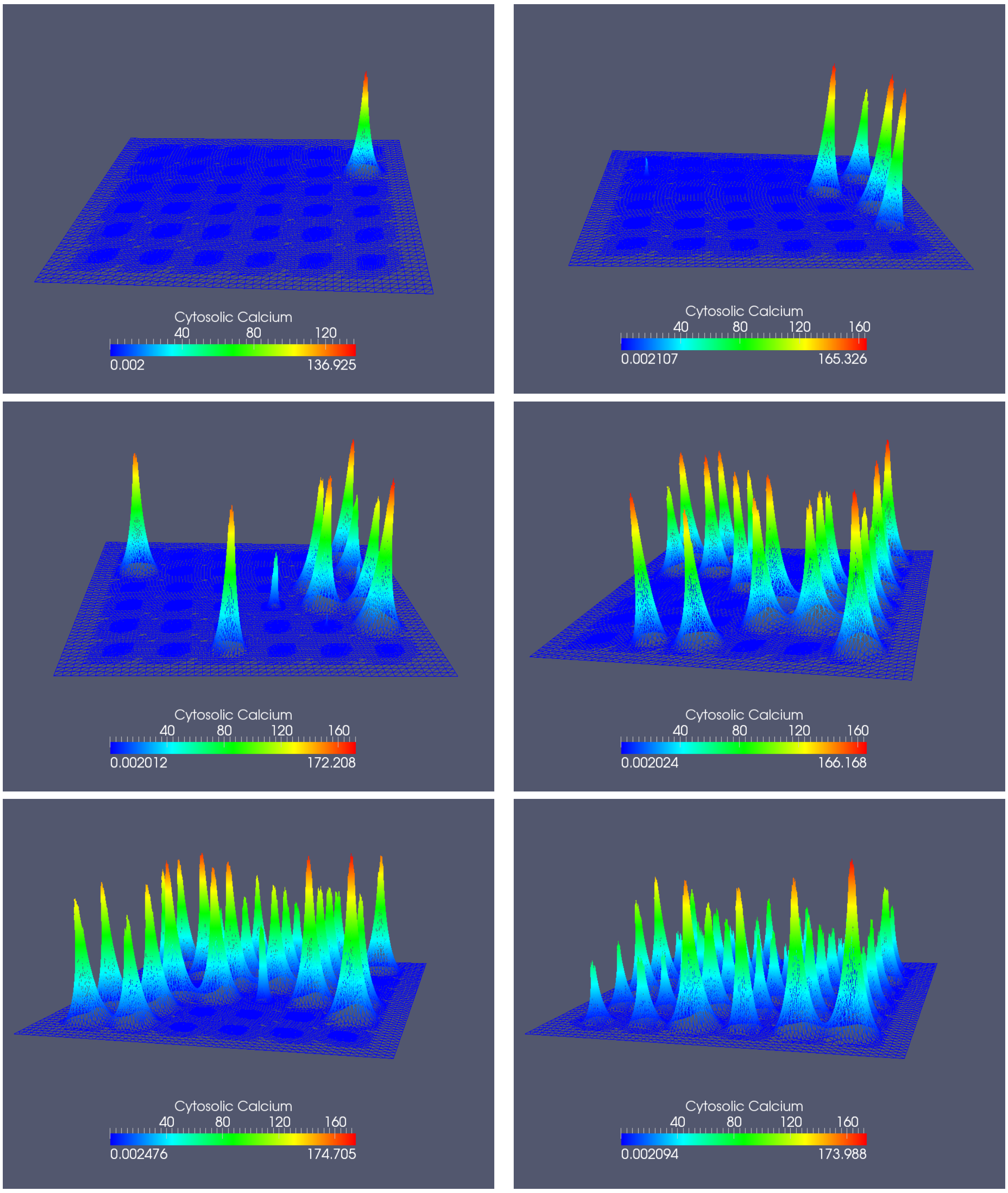

Figure 5.23: The contour plots showing cytosolic Ca^{2+} concentration for the stochastic channel transition at times $t = 0.0671946$, $t = 0.110721$, $t = 0.141145$, $t = 0.186711$, $t = 0.188291$, and $t = 0.277905\,s$ (from top left to bottom right).

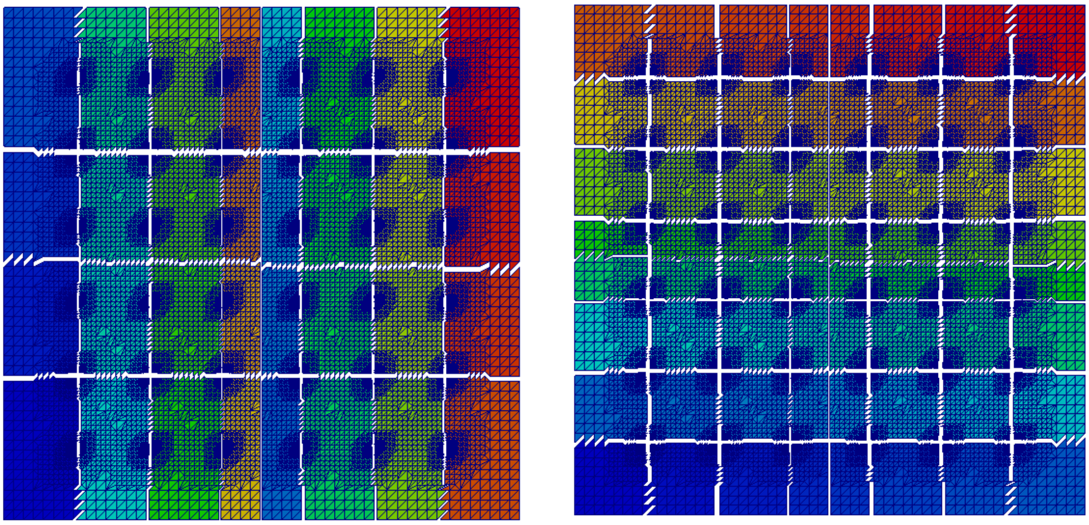

(a) on 28 cores

(b) on 64 cores

Figure 5.24: The mesh decomposition on different processors. Different colours show parts of the mesh assigned to different processors for the 36 cluster arrangement.

Chapter 6

Summary and future work

This thesis has been devoted to the analysis and numerical simulation of a highly coupled semilinear reaction-diffusion system that characterize intracellular calcium dynamics. The main results of this work can be broadly split into two parts. Firstly, we have proved global existence of strong solutions for system (3.2) using the semigroups theory. This system models the diffusion, binding and membrane transport of calcium ions within a cell. The system exhibit the (**P**)+(**M**) structure, where the positivity of the solutions is preserved for all time and the total mass of the components is uniformly controlled for all time.

Secondly, we have obtained high resolution numerical solutions in space and time for system (3.2). This has involved using the DG method of weighted interior penalties and mainly the linearly implicit Runge-Kutta methods of Rosenbrock type for the time integration. The numerical results have been demonstrated for several higher order spatial DG methods. We have adopted a hybrid method that couples the solution of the deterministic and stochastic part of the model simultaneously, see Alphonsi et al. [4]. By generating adaptive grids a priori and automatically adapting the time steps to the proper scales during the transition of channel states, the evolution of calcium ions and buffer concentrations have been resolved properly.

We recall that the first implementation of the model in Falcke [64] using the numerical method of continuous Galerkin discretization was published in [112, 140, 114, 115]. Here, adaptivity in space and time was used to simulate the stochastic and deteministic equations for the model (3.2). The spatial grid used in these simulations realized multichannels in a cluster by simply increasing the radius of each channel. The model in question describes concentrations and therefore necessitates an accurate numerical method that conserves concentration locally and in the entire domain. The work in [112, 140, 114, 115] suffers from this accuracy setback and is not easily scalable in the parallel approach when a larger problem of this model needs to be efficiently simulated.

In this treatise, we have presented the first DG implementation for the model in Falcke [64]. In contrast to the earlier implementations of this model, we have used a novel criterion for generating multiclusters and multichannels within the channel area. The implemented interior penalty DG method with weights accounts for discontinuities and small values of the diffusion coefficients. Comparatively, we have obtained more accurate results. But they were achieved at a relatively high computational cost. Our results from the parallel version of the simulation have vindicated the efficient parallelizability of DG methods resulting in the achievement of 66% parallel efficiency on 64 cores. We have compared two different time stepping schemes, i.e., the diagonally implicit Runge-Kutta (DIRK) and the linearly implicit Runge-Kutta (ROWDA) schemes, and our observations showed that the ROWDA method is computationally more efficient for this model.

The work of this thesis has made a genuine contribution to the modelling and simulation of intracellular calcium dynamics. Nevertheless, there are several extensions to the thesis that ought to be investigated and would be of potential significance to the biophysical study of calcium dynamics. We outline these possible directions for future studies as follows:

Firstly, our existence results have been based on the assumption that all the channels are open initially and remain open, see Equation (3.3). However, in reality, the process of opening and closing of channels is a stochastic process. Existence of both strong and weak solutions for this model where channels transition is a fully stochastic process remains an open problem to be analysed.

Secondly, we also remark that reaction-diffusion models with applications in biology, ecology, environment and population dynamics is now a buoyant area of research. The two natural properties (**P**)+(**M**) hold in most of these models, and hence bounded classical solutions may be sought. However, “incomplete blow up” may occur, and it may be necessary to give up looking for bounded classical solutions and rather consider weak solutions, see Pierre [126] for results in this direction. Nevertheless, the question of uniqueness to the weak solutions is still an open problem.

Lastly, we mention that there is currently more active research in the quest for optimal solvers for the linear systems resulting from DG discretizations. Employing such solvers will guarantee that the high computational costs encountered in accurately simulating this model is considerably reduced. At the moment, the types of solvers more promising for DG discretizations are multigrid and domain decomposition methods, see Blatt et al. [22]. The use of AMG solvers in this model has resulted in approximately 33% gain in computational cost which is quite significant. This work establishes a framework for future simulations in a 3D geometry based on meshes derived from scanned data of real cells.

Appendix A

Standard definitions and theorems

In this appendix, we state some standard important theorems that have been used in Chapter 3. We begin by recalling theorems about generation of analytic semigroups by second order strongly elliptic operators. Generally, the realization of elliptic operators with good coefficients and good boundary conditions are sectorial in the most common functional spaces.

Definition A.0.1. (A. Lunardi, [102, Appendix A]).
Let $A : D(A) \subset X \to X$ be a linear operator. The **resolvent set** $\rho(A)$ *and the* **spectrum** $\sigma(A)$ *of A are defined by*

$$\rho(A) = \{\lambda \in \mathbb{C} : \exists\ (\lambda I - A)^{-1} \in L(X)\}, \quad \sigma(A) = \mathbb{C} \setminus \rho(A). \tag{A.1}$$

Here, $L(X)$ denote the Banach space of linear bounded operators. The complex numbers $\lambda \in \rho(A)$ such that $(\lambda I - A)$ is not one to one are called **eigenvalues**. *The set $\sigma_p(A)$ consisting of all eigenvalues of A is called* **point spectrum**.
If $\lambda \in \rho(A)$, the **resolvent operator** *or simply* **resolvent** $R(\lambda, A)$ *is defined by*

$$R(\lambda, A) = (\lambda I - A)^{-1}. \tag{A.2}$$

Definition A.0.2. (A. Lunardi, [102, Chapter 2]).
A linear operator $A : D(A) \subset X \to X$ is **sectorial** *if there are constants $\omega \in \mathbb{R}$, $\theta \in]\pi/2, \pi[$, $M > 0$ such that*

$$\left\{ \begin{array}{ll} (i) & \rho(A) \supset S_{\theta,\omega} = \{\lambda \in \mathbb{C} : \lambda \neq \omega, |\arg(\lambda - \omega)| < \theta\}, \\ (ii) & \|R(\lambda, A)\|_{L(X)} \leq \frac{M}{|\lambda - \omega|}, \ \text{for all } \lambda \in S_{\theta,\omega}. \end{array} \right. \tag{A.3}$$

Note that every sectorial operator is closed, because its resolvent set is not empty.

We consider general second order elliptic operators in an open set $\Omega \subset \mathbb{R}^N$. Ω is either the whole $\mathbb{R}^N$ or a bounded open set with C^2 boundary $\partial\Omega$. Let $n(x)$ denote the outer unit vector normal to $\partial\Omega$ at x. Let $\mathcal{A}$ be the differential operator

$$(\mathcal{A})(x) = \sum_{i,j=1}^{N} a_{ij}(x)D_{ij}(x) + \sum_{i=1}^{N} b_i(x)D_i(x) + c(x)u(x) \tag{A.4}$$

with real, bounded and continuous coefficients a_{ij}, b_j, c on $\bar{\Omega}$. We require that for every $x \in \bar{\Omega}$, the matrix $[a_{ij}(x)]_{i,j=1,\dots,N}$ is symmetric and and strictly positive definite, i.e.,

$$\sum_{i,j=1}^{N} a_{ij}(x)\xi_i\xi_j \geq \nu|\xi|^2, \quad x \in \bar{\Omega}, \quad \xi \in \mathbb{R}^N, \tag{A.5}$$

For some $\nu > 0$. Moreover, if $\Omega = \mathbb{R}^N$, we require that the leading coefficients a_{ij} are uniformly continuous. Then the following results hold.

Theorem A.0.3. (S. Agmon, [2]). *Fix* $p \in]1, \infty[$.

(i) Let $A_p : W^{2,p}(\mathbb{R}^N) \to L^p(\mathbb{R}^N)$ *be defined by* $A_p u = \mathcal{A}u$. *The operator* A_p *is sectorial in* $L^p(\mathbb{R}^N)$ *and* $D(A_p)$ *is dense in* $L^p(\mathbb{R}^N)$.

(ii) Let Ω *and* $\mathcal{A}$ *be as above, and let* A_p *be defined by*

$$D(A_p) = W^{2,p}(\Omega) \cap W_0^{1,p}(\Omega), \;\; A_p u = \mathcal{A}u.$$

Then, the operator A_p *is sectorial in* $L^p(\Omega)$ *and* $D(A_p)$ *is dense in* $L^p(\Omega)$.

(iii) Let Ω *and* $\mathcal{A}$ *be as above, and let* A_p *be defined by*

$$D(A_p) = \{u \in W^{2,p}(\Omega) : \mathcal{B}_{|\partial\Omega} = 0\}, \;\; A_p u = \mathcal{A}u, \;\; u \in D(A_p),$$

where

$$\mathcal{B}(x) = b_0(x)u(x) + \sum_{i=1}^{N} b_i(x)D_i(x), \tag{A.6}$$

the coefficients b_i, $i = 1, \dots, N$ *are in* $C^1(\bar{\Omega})$ *and the transversality condition*

$$\sum_{i=1}^{N} b_i(x)n_i(x) \neq 0, \;\; x \in \partial\Omega \tag{A.7}$$

holds. Then, the operator A_p *is sectorial in* $L^p(\Omega)$ *and* $D(A_p)$ *is dense in* $L^p(\Omega)$.

Theorem A.0.4. (A. Lunardi [102, Thm. 3.1.1]).
Let the weaker ellipticity assumption given by (A.8) *and* (A.9) *hold for the operator defined in* (A.4).

$$\left|\sum_{i,j=1}^{N} a_{ij}(x)\xi_i\xi_j\right| \geq \mu|\xi|^2, \quad x \in \bar{\Omega}, \quad \xi \in \mathbb{R}^N, \tag{A.8}$$

$$\left\{\begin{array}{l} \textit{if } \xi,\, \mu \in \mathbb{R}^N \textit{ are linearly independent, then for each } x \in \bar{\Omega} \textit{ the} \\ \textit{polynomial } \tau \mapsto P(\tau) = \sum_{i,j=1}^{N} a_{ij}(x)(\xi_i + \tau\mu_i)(\xi_j + \tau\mu_j) \\ \textit{has a unique root with positive imaginary part.} \end{array}\right. \tag{A.9}$$

Let Ω be an open set with uniform C^2 boundary, and let a_{ij}, b_i, $c : \bar{\Omega} \mapsto \mathbb{C}$ be uniformly continuous and bounded functions, satisfying (A.8) *and* (A.9). *Let $\mathcal{A}$ be defined by* (A.4), *and in addition let b_0, b_i in* (A.5) *be uniformly continuous and bounded together with their first order derivatives in $\bar{\Omega}$. For every $u \in W^{2,p}(\Omega)$, with $p \in]1, \infty[$, set $f = \mathcal{A}(x)u$, $g = \mathcal{B}(x)u_{|\partial\Omega}$. Then there is a $c_p > 0$ such that*

$$\|u\|_{W^{2,p}(\Omega)} \leq c_p(\, \|u\|_{L^p(\Omega)} + \|f\|_{L^p(\Omega)} + \|g_1\|_{W^{1,p}(\Omega)}), \tag{A.10}$$

where g_1 is any $W^{1,p}$ extension of g to the whole Ω.

Theorem A.0.5. (A. Lunardi [102, Thm. 3.1.3]).
Fix $p \in]1, \infty[$ and let Ω be an open set with uniform C^2 boundary. Then there exist $\omega_p \geq \omega_1$, $M_p > 0$ such that if $\mathrm{Re}\,\lambda \geq \omega_\mathrm{p}$, then for every $u \in W^{2,p}(\Omega)$ we have, setting $g = \mathcal{B}(x)u_{|\partial\Omega}$,

$$|\lambda|\|u\|_p + |\lambda|^{1/2}\|Du\|_p + \|D^2u\|_p \leq M_p(\|(\lambda u - \mathcal{A}u\|_p + |\lambda|^{1/2}\|g_1\|_p + \|Dg_1\|_p), \tag{A.11}$$

where g_1 is any extension of g belonging to $W^{1,p}(\Omega)$.

Theorem A.0.6. (A. Pazy [123, Thm. 2.3.3]).
Let $S(t)$ be a C_0 (i.e., a strongly continuous) *semigroup and let A be its infinitesimal generator. $S(t)$ is a* compact semigroup *if and only if $S(t)$ is continuous in the uniform operator topology for $t > 0$ and $R(\lambda, A)$ is compact for $\lambda \in \rho(A)$.*

Theorem A.0.7. (A. Pazy [123, Thm. 2.6.13]).
Let $-A$ be the infinitesimal generator of an analytic semigroup $S(t)$ on a Banach space X. If $0 \in \rho(A)$ then,

(i) $S(t) : X \to D(A^\alpha)$ for every $t > 0$ and $\alpha \geq 0$.

(ii) For every $x \in D(A^\alpha)$ we have $S(t)A^\alpha x = A^\alpha S(t)x$.

(iii) For every $t > 0$ *and* $\delta > 0$ *the operator* $A^\alpha S(t)$ *is bounded and*

$$\|A^\alpha S(t)\|_{L(X)} \leq M_\alpha t^{-\alpha} e^{-\delta t}. \tag{A.12}$$

(iv) Let $0 < \alpha \leq 1$ *and* $x \in D(A^\alpha)$*. Then*

$$\|S(t)x - x\|_{L(X)} \leq C_\alpha t^\alpha \|A^\alpha x\|_{L(X)}. \tag{A.13}$$

Theorem A.0.8. (D. Henry [81, Thm. 1.4.8]).
If A *is a sectorial operator in a Banach space* X*, then* X^α *is a Banach space in the norm* $\|\cdot\|_\alpha$ *for* $\alpha \geq 0$, $X^0 = X$*, and for* $\alpha \geq \beta \geq 0$, X^α *is a dense subspace of* X^β *with continuous inclusion. If* A *has compact resolvent, the inclusion* $X^\alpha \subset X^\beta$ *is compact when* $\alpha > \beta \geq 0$.

Theorem A.0.9. (D. Henry [81, Thm. 1.6.1]).
Suppose that $\Omega \subset \mathbb{R}^N$ *is an open set having the* C^m *extension property,* $1 \leq p < \infty$ *and* A *is a sectorial operator in* $X = L^p(\Omega)$ *with* $X \subset W^{m,p}(\Omega)$ *for some* $m \geq 1$*. Then for* $0 \leq \alpha \leq 1$*,*

$$X^\alpha \subset W^{k,q}(\Omega) \quad \text{when } k - N/q < m\alpha - N/p, \quad q \geq p, \tag{A.14}$$

$$X^\alpha \subset C^\nu(\Omega) \quad \text{when } 0 \leq \nu < m\alpha - N/p. \tag{A.15}$$

Definition A.0.10. (A. Pazy [123, Sect. 6.1]).
Consider the semilinear initial value problem

$$\begin{cases} u'(t) + Au(t) = f(t, u(t)), & t > t_0 \\ u(t_0) = u_0 \end{cases} \tag{A.16}$$

where $-A$ *is the infinitesimal generator of a strongly continuous semigroup* $S(t)$, $t \geq 0$*, on a Banach space* X *and* $f : [t_0, T] \times X \to X$ *is continuous in* t *and satisfies a Lipschitz condition in* u*. Then for every* $u_0 \in X$*, the function* $u \in C([t_0, T], X)$ *defined by*

$$u(t) = S(t - t_0)u_0 + \int_{t_0}^t S(t - s) f(s, u(s))\, ds \tag{A.17}$$

is called the **mild solution** *of the initial value problem* (A.16).

Theorem A.0.11. Differential form of Gronwall's inequality (Evans [62, p. 624]).
Let $\eta(\cdot)$ *be a nonnegative, absolutely continuous function on* $[0, T]$*, which satisfies for a.e.* t *the differential inequality*

$$\eta'(t) \leq \phi(t)\eta(t) + \psi(t), \tag{A.18}$$

where $\phi(t)$ and $\psi(t)$ are nonnegative, summable functions on $[0, T]$ *. Then*

$$\eta(t) \le e^{\int_0^t \phi(s)\,ds}\left[\eta(0) + \int_0^t \psi(s)\,ds\right] \tag{A.19}$$

for all $0 \le t \le T$*.*

Definition A.0.12. (Lipschitz continuity); Hartman [77, p. 4].
A function $f(y)$ defined on a y-set $E \subset \mathbb{R}^d$ is said to be **uniformly Lipschitz continuous** *on E with respect to y if there exists a constant K satisfying*

$$|f_1(y) - f_2(y)| \le K|y_1 - y_2| \qquad \text{for } y_1, y_2 \in E. \tag{A.20}$$

Definition A.0.13. (Uniform boundedness); Hsieh and Sibuya [85, p. 9].
A family $\mathcal{F}$ of functions $f(y)$ defined on some y-set $E \subset \mathbb{R}^d$ is said to be **uniformly bounded** *if, for all $y \in E$ and $f \in \mathcal{F}$ there exists a non-negative number M such that $|f(y)| \le M$.*

Definition A.0.14. (Equicontinuity); Hartman [77, p. 3].
A family $\mathcal{F}$ of functions $f(y)$ defined on some y-set $E \subset \mathbb{R}^d$ is said to be **equicontinuous** *if, for every $\epsilon > 0$, there exists a $\delta > 0$ such that $|f_1(y) - f_2(y)| \le \epsilon$ whenever $y_1, y_2 \in E$, $|y_1 - y_2| \le \delta$ and all $f \in \mathcal{F}$.*

Definition A.0.15. (Uniform convergence); Royden [139, p. 49].
A family f_n of functions defined on some y-set E is said to **converge uniformly** *to a function f on E if given $\epsilon > 0$, there is a N such that for all $y \in E$ and all $n \ge N$, we have $|f(y) - f_n(y)| < \epsilon$.*

Theorem A.0.16. (Arzela-Ascoli); Hartman [77, p. 4].
On a compact y-set $E \subset \mathbb{R}^d$, let $f_1(y), f_2(y), \cdots$ be a sequence of functions which is uniformly bounded and equicontinuous. Then there exists a sub-sequence $f_{n(1)}(y), f_{n(2)}(y), \cdots$ which is uniformly convergent on E.

Lemma A.0.17. (Lemma 18 in J. Droniou and K. S. Talbot [53]).
Let Ω be a bounded subset of $\mathbb{R}^N$, $N \in \mathbb{N}$ and for each $n \in \mathbb{N}$, let $H_n : \Omega \times \mathbb{R}^N \to \mathbb{R}$ be a Carathéodory function such that

- *there exists positive constants C, γ such that for a.e. $x \in \Omega$,*

$$|H_n(x, \xi)| \le C(1 + |\xi|^\gamma) \quad \forall \xi \in \mathbb{R}^N,\ \forall n \in \mathbb{N}, \tag{A.21}$$

- *there is a Carathéodory function $H : \Omega \times \mathbb{R}^N \to \mathbb{R}$ such that for a.e. $x \in \Omega$,*

$$H_n(x, \cdot) \to H(x, \cdot) \quad \text{uniformly on compact sets as} \quad n \to \infty. \tag{A.22}$$

If $p \in [\gamma, \infty)$ and $(u_n)_{n \in \mathbb{N}} \subset L^p(\Omega)^N$ is a sequence with $u_n \to u$ in $L^p(\Omega)^N$ as $n \to \infty$, then

$$H_n(\cdot, u_n) \to H(\cdot, u) \quad \text{in} \quad L^{p/\gamma}(\Omega) \quad \text{as} \quad n \to \infty.$$

Appendix B

Hybrid algorithm and simulation parameters

Algorithm 3

1. Choose $u_{old} = u_0$, $X = X_0$, $g_{old} = 0$, $t_{old} = 0$, $\Delta t > 0$. Draw a uniform random number r_1 in [0,1] defining $\xi = \ln(1/r_1)$.

2. Deterministic step: If TOL_t is met, update solution u_{new} and g_{new}, $t_{new} = t_{old} + \Delta t$.

3. If $g_{new} < \xi$(no stochastic event), set $u_{old} = u_{new}$, $g_{old} = g_{new}$, $t_{old} = t_{new}$ and go to 2.

4. If $g_{new} \geq \xi$(some stochastic event in $[t_{old}, t_{new}]$)

   - Determine event time $t_s \in [t_{old}, t_{new}]$ by linear interpolation, compute Ca^{2+} concentration c_s at t_s by linear interpolation.
   - Draw a uniform random number r_2 in [0,1] and determine R_i according to Equation (2.7) based on c_s.

5. If the next event is non-channel transition

   - Perform stochastic event R_i to determine new channel state X.
   - Set $g_{old} = 0$, recompute g_{new} based on c_s, g_{old} and the remaining time step $t_{new} - t_s$.
   - Draw a new uniform random number r_1 in [0,1] defining $\xi = \ln(1/r_1)$, and go to 3.

6. If next event R_i is a channel transition

   - Perform the channel transition R_i to determine new channel state X.

- Set $g_{new} = 0$, draw a new uniform random number r_1 in [0,1] defining $\xi = \ln(1/r_1)$.
- Set $t_{new} = t_s$, define new time step $\Delta t > 0 = \Delta t_{channel}$ (a sufficiently small number).
- Set $u_{old} = u_s$, and go to deteministic step 2.

Parameter	Value	Unit
leak flux coefficient P_l	0.025	s^{-1}
channel flux coefficient P_{ch}	2.5×10^4	s^{-1}
single channel radius R_s	0.012	μm
pump flux coefficient P_p	5.0×10^3	$\mu M\ s^{-1}$
pump dissociation coefficient K_d	0.04	μM
diffusion coefficient D of the free cytosolic Ca^{2+}	223	$\mu m^2\ s^{-1}$
diffusion coefficient D of the free ER Ca^{2+}	200	$\mu m^2\ s^{-1}$
diffusion coefficient D_m of mobile buffer	40	$\mu m^2\ s^{-1}$
diffusion coefficient D_s of stationary buffer	0	$\mu m^2\ s^{-1}$
on-rates of fast buffers:		
k_s^+	50	$(\mu M\ s)^{-1}$
k_m^+	700	$(\mu M\ s)^{-1}$
dissociation constants of buffers $K_i = \frac{k_i^-}{k_i^+}$:		
k_s^-	100	s^{-1}
k_m^-	170	s^{-1}
total concentration of buffers:		
B_s	80	μM
B_m	40	μM
subunit kinetics, note $\mathrm{b_i = a_i d_i, i = 1, ..., 5}$		
$\mathrm{IP_3}$ binding		
$\mathrm{a_1, a_3}$	0.2	$(\mu M\ s)^{-1}$
$\mathrm{d_1}$	0.0013	μM
$\mathrm{d_3}$	2.0	μM
inhibiting, with $\mathrm{IP_3}$		
$\mathrm{a_2}$	0.02	$(\mu M\ s)^{-1}$
$\mathrm{d_2}$	78	μM
inhibiting, without $\mathrm{IP_3}$		
$\mathrm{a_4}$	0.1	$(\mu M\ s)^{-1}$
$\mathrm{d_4}$	0.4	μM
activating		
$\mathrm{a_5}$	100	$(\mu M\ s)^{-1}$
$\mathrm{d_5}$	0.25	μM

Table B.1: Parameters used in the numerical simulations.

Bibliography

[1] R. A. Adams. *Sobolev spaces.* Academic press, New York, 1975.

[2] S. Agmon. On the eigenfunctions and the eigenvalues of general elliptic boundary value problems. *Comm. Pure. Appl. Math.*, 15:119–147, 1962.

[3] R. Alexander. Diagonally implicit Runge - Kutta methods for stiff O.D.E's. *SIAM Journal on Numerical Analysis*, 14:1006–1021, 1977.

[4] A. Alfonsi, E. Cancs, G. Turinici, B. Di Ventura, and W. Huisinga. Exact stochastic simulation of hybrid stochastic and deterministic models for biochemical systems. *INRIA Rapport de Recherche, Thèmes NUM et BIO*, 5435, 2004.

[5] N. D. Alikakos. L^p-bounds of solutions of reaction-diffusion equations. *Comm. Partial Differential Equations*, 4:827–868, 1979.

[6] H. Amann. Dual semigroups and second order linear elliptic boundary value problems. *Israel Journal of Mathematics*, 45(2-3):225–254, 1983.

[7] H. Amann. *Linear and Quasilinear Parabolic Problems, Volume I, Abstract Linear Theory.* Birkhäuser Verlag, Basel, 1995.

[8] D. N. Arnold. An interior penalty finite element method with discontinuous elements. *SIAM J. Numer. Anal.*, 19:742–760, 1982.

[9] D. N. Arnold, F. Brezzi, B. Cockburn, and L. D. Marini. Unified analysis of discontinuous Galerkin methods for elliptic problems. *SIAM J. Numer. Anal.*, 39:1749–1779, 2002.

[10] J. F. G. Auchmuty and G. Nicolis. Bifurcation analysis of nonlinear reaction-diffusion equations–I. Evolution equations and steady state solutions. *Bull. Math. Biol.*, 37:323–365, 1975.

[11] I. Babuška. The finite element method with penalty. *Math. Comp.*, 27:221–228, 1973.

[12] I. Babuška and M. Zlámal. Nonconforming elements in the finite element method with penalty. *SIAM J. Numer. Anal.*, 10(5):863–875, 1973.

[13] G. A. Baker. Finite element methods for elliptic equations using nonconforming elements. *Math. Comp.*, 31(137):45–49, 1977.

[14] R. E. Bank, A. Sherman, and A. Weiser. Refinement algorithms and data structures for regular local mesh refinement. *Scientific Computing*, 1983.

[15] A. Barabanova. On the global existence of solutions of a reaction-diffusion equation with exponential nonlinearity. *Proc. Amer. Math. Soc.*, 122:827–831, 1994.

[16] R. Barrett, M. Berry, T. F. Chan, J. Demmel, J. Donato, J. Dongarra, V. Eijkhout, R. Pozo, C. Romine, and H. Van der Vorst. *Templates for the Solution of Linear Systems: Building Blocks for Iterative Methods, 2nd Edition.* SIAM, Philadelphia, PA, 1994.

[17] F. Bassi and S. Rebay. A high-order accurate discontinuous finite element method for the numerical solution of the compressible Navier-Stokes equations. *J. Comp. Phys.*, 131(2):267–279, 1997.

[18] P. Bastian. Parallel adaptive multigrid methods. Technical Report 93â60, Interdisziplinäres Zentrum für Wissenschaftliches Rechnen. 1993.

[19] P. Bastian. *Numerical computation of multiphase flow in porous media.* Habilitationsschrift. 1999.

[20] P. Bastian, K. Birken, S. Lang, K. Johannsen, N. Neuß, H. Rentz-Reichert, and C. Wieners. UG: A flexible software toolbox for solving partial differential equations. *Computing and Visualization in Science*, 1:27–40, 1997.

[21] P. Bastian, M. Blatt, A. Dedner, C. Engwer, R. Klöfkorn, R. Kornhuber, M. Ohlberger, and O. Sander. Ageneric grid interface for parallel and adaptive scientific computing. Part II: Implementation and tests in DUNE. *Computing*, 82(2):121–138, 2008.

[22] P. Bastian, M. Blatt, and R. Scheichl. Algebraic multigrid for discontinuous Galerkin discretizations. *Numer. Linear Algebra Appl.*, 00:1–22, 2012.

[23] P. Bastian, F. Heimann, and S. Marnach. Generic implementation of finite element methods in the distributed and unified numerics environment (DUNE). *Kybernetika*, 46(2):294–315, 2010.

[24] C. E. Baumann and J. T. Oden. A discontinuous hp finite element method for convection-diffusion problems. *Comput. Methods Appl. Mech. Engrg*, 175(3-4):311–341.

[25] S. Benachour and B. Rebiai. Global classical solutions for reaction-diffusion systems with nonlinearities of exponential growth. *J. Evol. Equ.*, 10(3):511–527, 2010.

[26] M. J. Berridge. Calcium oscillations. *J. Biol. Chem.*, 265:9583–9586, 1990.

[27] M. J. Berridge. Inositol triphosphate and calcium signalling. *Nature*, 361:315, 1993.

[28] M. J. Berridge. Elementary and global calcium signalling. *J. Physiol.*, 499:291–306, 1997.

[29] M. J. Berridge, M. D. Bootman, and P. Lipp. Calcium - a life and death signal. *Nature*, 395:645–648, 1998.

[30] M. J. Berridge, M. D. Bootman, and P. Lipp. The versatility and universality of calcium signaling. *Nature Rev. Mol. Cell Biol.*, 1:11–12, 2000.

[31] I. Bezprozvanny, J. Watras, and B. E. Ehrlich. Bell-shaped calcium-response curves of Ins(1,4,5)P_3- and calcium-gated channels from endoplasmatic reticulum of cerebellum. *Nature*, 351:751–754, 1991.

[32] M. D. Bootman, T.J. Collins, C.M. Peppiat, L.S. Prothero, L. Mackenzie, P. Desmet, M. Travers, S.C. Tovey, J.T. Seo, M.J. Berridge, F. Ciccolini, and P. Lipp. Calcium signalling - an overview. *Seminars in Cell and Developmental Biology*, 12(1):3–10, 2001.

[33] D. Braess. *Finite Elements: Theory, Fast Solvers, and Applications in Solid Mechanics.* Cambridge University Press, 2001.

[34] S. Brdar, A. Dedner, and R. Klöfkorn. Compact and stable discontinuous Galerkin methods for convection-diffusion problems. *SIAM J. Sci. Comput.*, 30(1):A263–A282, 2012.

[35] S. C. Brenner and L. R. Scott. *The mathematical theory of finite element methods,* volume 15 of *Texts in Applied Mathematics.* Springer, New York, 3rd edition 2008.

[36] N. Callamaras, X.P. Sun, J.S. Marchant, and I. Parker. Activation and coordination of IP_3 mediated elementary Ca^{2+} events during global Ca^{2+} signals in Xenophus oocytes. *J. Physiol*, 509(1):81–91, 1998.

[37] C. Caputo and A. Vasseur. Global regularity of solutions to systems of reaction-diffusion with sub-quadratic growth in any dimension. *Comm. Partial Differential Equations*, 34:1228–1250, 2009.

[38] P. Caussignac and R. Touzani. Solution of three-dimensional boundary layer equations by a discontinuous finite element method. I. Implementation and numerical results. *Comput. Methods Appl. Engrg.*, 79(1):1–20, 1990.

[39] P. Caussignac and R. Touzani. Solution of three-dimensional boundary layer equations by a discontinuous finite element method. I. Numerical analysis of a linear model problem. *Comput. Methods Appl. Engrg.*, 78(3):249–271, 1990.

[40] G. Chavent and B. Cockburn. The local projection P^0P^1-discontinuous-Galerkin finite element method for scalar conservation laws. *RAIRO Modél. Math. Anal. Numér.*, 23(4):565–592, 1989.

[41] P. G. Ciarlet. *The finite element method for elliptic problems,*volume 40 of *Classics in Applied Mathematics.* Society for Industrial and Applied Mathematics (SIAM), Philadelphia, PA, Reprint of the 1978 original [North-Holland, Amsterdam; MR0520174 (58 # 25001)], 2002.

[42] B. Cockburn, S. Hou, and C. W. Shu. TVB Runge-Kutta local projection discontinuous Galerkin finite element method for conservation laws. IV. The multidimensional case. *Math. Comp.*, 54:545–581, 1990.

[43] B. Cockburn, G. E. Karniadakis, and C. W. Shu. The development of discontinuous Galerkin methods. In B. Cockburn, G.E Karniadakis and C.W Shu(eds) *Discontinuous Galerkin Methods. Theory, Computation and Applications.*, volume 11. Springer-Verlag,pp3-50, 2000.

[44] B. Cockburn, S. Y. Lin, and C. W. Shu. TVB Runge-Kutta local projection discontinuous Galerkin finite element method for conservation laws. III. One-dimensional systems. *J. Comput. Phys.*, 84:90–113, 1989.

[45] B. Cockburn and C. W. Shu. TVB Runge-Kutta local projection discontinuous Galerkin finite element method for conservation laws. II. General framework. *Math. Comput.*, 52(186):411–435, 1989.

[46] B. Cockburn and C. W. Shu. The Runge-Kutta local projection P^1-discontinuous- Galerkin finite element method for scalar conservation laws. *RAIRO Modél. Math. Anal. Numér.*, 25(3):337–361, 1991.

[47] B. Cockburn and C. W. Shu. The local discontinuous Galerkin finite element method for convection-diffusion systems. *SIAM J. Numer. Anal.*, 35:2440–2463, 1998.

[48] B. Cockburn and C. W. Shu. The Runge-Kutta discontinuous Galerkin method for conservation laws. IV. Multidimensional systems. *J. Comput. Phys.*, 141(2):199–224, 1998.

[49] C. Dawson, S. Sun, and M. Wheeler. Compatible algorithms for coupled flow and transport. *Computer Methods in Applied Mechanics and Engineering*, 193:2565–2580, 2004.

[50] K. Deimling. *Multivalued Differential Equations.* Walter de Gruyter, Berlin-New York, 1992.

[51] L. Desvillettes and K. Fellner. Exponential Decay toward Equilibrium via Entropy Methods for Reaction-Diffusion Equations. *J. Math. Anal. Appl.*, 319:157–176, 2006.

[52] G. DeYoung and J. Keizer. A single-pool inositol 1,4,5-triphosphate receptor-based model for agonist-stimulated oscillations in Ca^{2+} concentration. *Proc. Natl. Acad. Sci. USA*, 89:9895–9899, 1992.

[53] J. Droniou and K. S. Talbot. On a miscible displacement model in porous media flow with measure data. *SIAM Journal on Mathematical Analysis*, 46(5):3158–3175, 2014.

[54] M. Dryja. On discontinuous Galerkin methods for elliptic problems with discontinuous coeffients. *Comput. Methods Appl. Math.*, 3(1):76–85, 2003.

[55] G. Dupont and A. Goldbeter. Properties of intracellular Ca^{2+} waves generated by a model based on Ca^{2+} - induced Ca^{2+} release. *J. Biophysics*, 67:2191–2204, 1994.

[56] G. Dupont and S. Swillens. Quantal release, incremental detection, and long period Ca^{2+} oscillations in a model based on regulatory Ca^{2+} binding sites along the permeation pathway. *J. Biophysics*, 71:1714–1722, 1995.

[57] Y. Epshteyn and B. Riviére. Estimation of penalty parameters for symmetric interior penalty Galerkin methods. *Journal of Computational and Applied Mathematics*, 206:843–872, 2007.

[58] A. Ern and J.-L. Guermond. Discontinuous Galerkin methods for Friedrichs' systems. I. General theory. *SIAM J. Numer. Anal.*, 44(2):753–778, 2006.

[59] A. Ern and J.-L. Guermond. Discontinuous Galerkin methods for Friedrichs' systems. II. Second-order elliptic PDEs. *SIAM J. Numer. Anal.*, 44(6):2363–2388, 2006.

[60] A. Ern and J.-L. Guermond. Discontinuous Galerkin methods for Friedrichs' systems. III. Multi-field theories with partial coercivity. *SIAM J. Numer. Anal.*, 46(2):776–804, 2008.

[61] A. Ern, F. A. Stephansen, and P.A. Zunino. A discontinuous Galerkin method with weighted averages for advection-diffusion equations with locally small and anisotropic diffusivity. *IMA J. Numer. Anal.*, 29:235–256, 2009.

[62] L. C. Evans. *Partial differential equations.* American Math. Soc., Providence, Rhode Island, 1998.

[63] M. Falcke. On the role of stochastic channel behaviour in intracellular Ca^{2+} dynamics. *J. Biophysics*, 84:42–56, 2003.

[64] M. Falcke. Reading the patterns in living cells - the Physics of Ca^{2+} signalling. *Advances in Physics*, 53:255–440, 2004.

[65] M. Falcke, L. Tsimring, and H. Levine. Stochastic spreading of intracellular Ca^{2+} release. *Phys. Rev . E*, 62:2636–2643, 2000.

[66] A. F. Filippov. *Differential Equations with Discontinuous Righthand Sides.* Kluwer Acad. Publ., The Netherlands, 1988.

[67] W. E. Fitzgibbon, S. L. Hollis, and J. J. Morgan. Stability and Lyapunov Functions for Reaction-Diffusion Systems. *SIAM J. Math. Anal.*, 28:595–610, 1997.

[68] D. T. Gillespie. A general method for numerically simulating the stochastic time evolution of coupled chemical reactions. *J. Comput. Phys.*, 22:403–434, 1976.

[69] D. T. Gillespie. Exact stochastic simulation of coupled chemical reactions. *J. Phys. Chem.*, 81:2340–2361, 1977.

[70] D. T. Gillespie. *Markov Processes - An Introduction for Physical Scientists.* Academic Press, 1992.

[71] B. C. Goodwin and L. E. H. Trainor. Tip and whorl morphogenesis in Acetabularia by Calcium-regulated strain fields. *J. Theor. Biol.*, 117:79–106, 1985.

[72] Th. Goudon and A. Vasseur. Regularity Analysis for Systems of Reaction-Diffusion Equations. *Annales Sci. ENS*, 2010.

[73] K. Gustafsson, M. Lundh, and G. Söderlind. A PI stepsize control for the numerical solution of ordinary differential equations. *BIT*, 28(2):270–287, 1988.

[74] E. Hairer, S. P. Nørsett, and G. Wanner. *Solving Ordinary Differential Equations I: Nonstiff problems.* Springer Series in Computational Mathematics, 1987.

[75] E. Hairer and G. Wanner. *Solving Ordinary Differential Equations II.* Springer Series in Computational Mathematics, 1991.

[76] A. Haraux and A. Youkana. On a result of K. Masuda concerning reaction-diffusion equations. *Tôhoku Math. J.*, 40:159–163, 1988.

[77] P. Hartman. *Ordinary Differential Equations.* John Wiley & Sons, Inc., New York, 1964.

[78] T. D. Hassinger, P. B. Atkinson, G.J. Strecker, L.R. Wahlen, F.E. Dudek, A.H. Kossel, and S.B. Kater. Evidence for glutamate-mediated activation of hippocampal neurons by glial calcium waves. *J. Neurobiol.*, 28:159–170, 1995.

[79] S. Heikkilä. On functional differential equations with discontinuous right hand side in ordered Banach spaces. *Funkcialaj Ekvacioij*, 33:519–526, 1990.

[80] S. Heikkilä and V. Lakshmikantha. *Monotone Iterative Techniques for Discontinuous Nonlinear Differential Equations.* Mercel Dekker, Inc. New York, 1994.

[81] D. Henry. *Geometric Theory of Semilinear Parabolic Equations.* Lecture Notes in Mathematics 840. Springer-Verlag, New York, 1981.

[82] J. S. Hesthaven and T. Warburton. *Nodal Discontinuous Galerkin Methods.* Springer, New York, 2008.

[83] S. L. Hollis and J. Morgan. On the blow-up of solutions to some semilinear and quasilinear reaction-diffusion systems. *Rocky Mountain J. Math.*, 14:491–511, 1994.

[84] P. Houston and R. Hartmann. An optimal order interior penalty discontinuous Galerkin discretization of the compressible Navier-Stokes equations. *J. Comput. Phys.*, 227:9670–9685, 2008.

[85] P. F. Hsieh and Y. Sibuya. *Ordinary Differential Equations.* Springer-Verlag, New York, Inc., 1999.

[86] S. C. Hu. Differential equations with discontinuous right-hand sides. *J. Math. Anal. Appl.*, 154:377–390, 1991.

[87] W. Hundsdorfer and J. Verwer. *Numerical Solution of Time Dependent Advection-Diffusion-Reaction Equations.* Springer, Berlin, 2003.

[88] J. K. Hunter. *Lecture Notes on Partial Differential Equations.* Department of Mathematics, University of California at Davis, https://www.math.ucdavis.edu/ hunter/pdes/pde-notes.pdf, 2012.

[89] J. Jaffré, C. Johnson, and A. Szepessy. Convergence of the discontinuous Galerkin finite element method for hyperbolic conservation laws. *M3AS*, 5(3):367–386, 1995.

[90] C. Johnson and J. Pitkäranta. An analysis of the discontinuous Galerkin method for a scalar hyperbolic equation. *Math. Comp.*, 46(173):1–26, 1986.

[91] J. Douglas Jr. and T. Dupont. *Lecture Notes in Physics,* volume 58, chapter Interior penalty procedures for elliptic and parabolic Galerkin methods. Springer-Verlag, Berlin, 1976.

[92] J. I. Kanel. Cauchy's problem for semilinear parabolic equations with balance law. *Differ. Uravn.*, 20:1753–1760, 1984.

[93] J. I. Kanel. The solvability on the whole of reaction-diffusion systems with condition of balance. *Differ. Uravn.*, 26:448–458, 1990.

[94] J. I. Kanel. On global initial boundary-value problems for reaction-diffusion systems with balance conditions. *Nonlinear Anal.*, 37:971–995, 1999.

[95] C. T. Kelly. *Iterative Methods for Linear and Nonlinear Equations.* SIAM, 1995.

[96] S. Kouachi. Existence of global solutions to reaction-diffusion systems via a Lyapunov functional. *Electron. J. Differential Equations*, 68:1–10, 2001.

[97] O. A. Ladyženskaja, V. A. Solonnikov, and N. N. Ural'ceva. *Linear and Quasi-linear Equations of Parabolic Type.* Translation of Mathematical Monographs. Amer. Math. Soc., 1968.

[98] S. Lang. *Parallele Numerische Simulation instationärer Probleme mit adaptiven Methoden auf unstrukturierten Gittern.* PhD thesis, Universität Stuttgart, 2001.

[99] P. Lesaint. Finite element methods for symmetric hyperbolic equations. *Numer. Math.*, 21:244–255, 1973/74.

[100] P. Lesaint and P. A. Raviart. On a finite element method for solving the neutron transport equation. In *Mathematical Aspects of Finite Elements in Partial Differential Equations*, pages 89-123. Publication No. 33, Math. Res. Center, Univ. of Wisconsin-Madison, Academic Press, New York. 1974.

[101] J. H. Lightbourne and R. H. Martin. Relatively continuous nonlinear perturbations of analytic semigroups. *J. Nonlinear Anal.-Theory Meth. Appl.*, 1:277–292, 1977.

[102] A. Lunardi. *Analytic Semigroups and Optimal Regularity in Parabolic Problems.* Birkhäuser, Basel, 1995.

[103] A. Madzvamuse. Time-stepping schemes for moving grid finite elements applied to reaction-diffusion systems on a fixed and growing domains. *J. Comput. Phys.*, 214:239–263, 2006.

[104] A. Madzvamuse, A. J. Wathen, and P. K. Maini. A moving grid finite element method applied to a model biological pattern generator. *J. Comput. Phys.*, 190:478–500, 2003.

[105] D. D. Mak and J. K. Foskett. Single-channel kinetics, inactivation and spatial distribution of inositol triphosphate (IP_3) receptor in Xenopus oocyte nucleus. *J. Gen. Physiol.*, 109:571–587, 1997.

[106] D. D. Mak, S. McBridge, V. Raghuram, Y. Yue, S. K. Joseph, and J. K. Foskett. Single-channel properties in endoplasmic reticulum membrane of recombinant type 3 inositol triphosphate receptor. *J. Gen. Physiol.*, 115:241–255, 2000.

[107] J. S. Marchant and I. Parker. Role of elementary Ca^{2+} puffs in generating repetitive Ca^{2+} oscillations. *The EMBO Journal*, 20:65–67, 2001.

[108] K. Masuda. On the global existence and asymptotic behavior of solutions of reaction-diffusion equations. *Hokkaido Math. J.*, 12:360–370, 1983.

[109] J. Morgan. Global existence for semilinear parabolic systems. *SIAM J. Math. Anal.*, 20:1128–1144, 1989.

[110] J. Morgan. Boundedness and decay results for reaction-diffusion systems. *SIAM J. Math. Anal.*, 21:1172–1189, 1990.

[111] K. Morton and D. Mayers. *Numerical solution of partial differential equations: an introduction.* Cambridge Univ. Press, 2005.

[112] C. Nagaiah. *Adaptive numerical simulation of reaction-diffusion systems.* PhD thesis, Otto-von-Guericke University, http://diglib.uni-magdeburg.de/Dissertationen/2007/chanagaiah.pdf, 2007.

[113] C. Nagaiah and S. Rüdiger. Whole-cell simulations of hybrid stochastic and deterministic calcium dynamics in 3D geometry. *Journal of Computational Interdisciplinary Sciences*, 3(1-2):3–18, 2012.

[114] C. Nagaiah, S. Rüdiger, G. Warnecke, and M. Falcke. Adaptive numerical simulation of intracellular calcium dynamics using domain decomposition methods. *Applied Numerical Mathematics*, 58:1658–1674, 2008.

[115] C. Nagaiah, S. Rüdiger, G. Warnecke, and M. Falcke. Adaptive space and time numerical simulation of reaction-diffusion models for intracellular calcium dynamics. *Applied Mathematics and Computations*, 218:10194–10210, 2012.

[116] E. A. Newman and K. R. Zahs. Calcium waves in retinal glial. *Science*, 275:844–847, 1997.

[117] J. Nitsche. Über ein Variationsprinzip zur Lösung von Dirichlet-Problemen bei Verwendung von Teilräumen, die keinen Randbedingungen unterworfen sind. *Abh. Math. Sem. Uni. Hamburg*, 36:9–15, 1971. Collection of articles dedicated to Lothar Collatz on his sixtieth birthday.

[118] J. Nitsche. On Dirichlet problems using subspaces with nearly zero boundary conditions. In *The mathematical foundations of the finite element method with applications to partial differential equations (Proc. Sympos., Univ. Maryland, Baltimore, Md., 1972).* Academic Press, New York, 1972.

[119] J. T. Oden, I. Babuška, and C. E. Baumann. A discontinuous hp finite element method for diffusion problems. *J. Comput. Phys.*, 148:491–519, 1998.

[120] E. T. Olsen and J. Douglas Jr. Bounds on spectral condition numbers of matrices arising in the p-version of the finite element method. *Num. Math.*, 69(3):333–352, 1995.

[121] S. Orszag and G. Patterson. Numerical simulation of turbulence. *Statistical models and Turbulence*, pages 127–147, 1972.

[122] I. Parker and Y. Yao. Ca^{2+} transients associated with openings of inositol triphosphate gated channels in Xenopus oocytes. *J. Physiol.(Lond.)*, 491:663–668, 1996.

[123] A. Pazy. *Semigroups of Linear Operators and Applications to Partial Differential Equations.* Applied Math. Sciences, 44. Springer-Verlag, New York, 1983.

[124] J. Peraire and P.-O. Persson. The compact discontinuous Galerkin (CDG) method for elliptic problems. *SIAM J. Sci. Comput.*, 30:1806–1824, 2008.

[125] P. O. Persson and J. Peraire. Newton-GMRES preconditioning for discontinuous Galerkin discretizations of the Navier-Stokes equations. *SIAM J. Sci. Comp.*, 30(6):2709–2733, 2008.

[126] M. Pierre. Global Existence in Reaction-Diffusion Systems with Control of Mass: a Survey. *Milan J. Math.*, 78:417–455, 2010.

[127] M. Pierre. Reaction-Diffusion systems with positivity and mass control: global existence and singular limits. *Lecture Notes, 3rd Spring School, University Duisburg-Essen*, 2011.

[128] D. A. Di Pietro, A. Ern, and J.-L. Guermond. Discontinuous Galerkin methods for anisotropic semi-definite diffusion with advection. *SIAM J. Numer. Anal.*, 46(2):805–831, 2008.

[129] D. Di Pietro and E. Alexandre. *Mathematical Aspects of Discontinuous Galerkin Methods.* Springer, Berlin, 2012.

[130] J. W. Putney and G. S. J. Bird. The inositolphophate-calcium signalling system in nonexcitable cells. *Endocrine Reviews*, 14:610–631, 1993.

[131] A. Quarteroni, R. Sacco, and F. Saleri. *Numerical Mathematics.* Springer Verlag, Berlin, 2000.

[132] W. H. Reed and T. R. Hill. *Triangular mesh methods for the neutron transport equation.* Los Alamos Scientific Laboratory Report, 1973.

[133] E. B. Ridgway, J. C. Gilkey, and L. F. Jaffe. Free calcium increases explosively in activating medaka eggs. *Proc. Natl. Acad. Sci. USA*, 74:623–627, 1977.

[134] B. Riviére. *Discontinuous Galerkin Methods for Solving Elliptic and Parabolic Equations: Theory and Implementation.* SIAM, 2008.

[135] B. Riviére, M. F. Wheeler, and V. Girault. Improved energy estimates for interior penalty, constrained and discontinuous Galerkin methods for elliptic problems. *Comput. Geom.*, 3:337–360, 1999.

[136] H. L. Roderick, M. J. Berridge, and M. D. Bootman. The Endoplasmic Reticulum: A Central Player in Cell Signalling and Protein Synthesis. In *Understanding Calcium Dynamics: Experiments and Theory.* Springer-Verlag, Berlin, 2003.

[137] T. A. Rooney, E. J. Sass, and A.P. Thomas. Characterization of cytosolic calcium oscillations induced by phenylephrine and vasopressin in single fura-2-loaded hepatocytes. *J. Biol. Chem.*, 264:17131–17141, 1989.

[138] F. Rothe. *Global Solutions of Reaction-Diffusion Systems. Lecture Notes in Mathematics.*, volume 1072. Springer, Berlin, 1984.

[139] H. L. Royden. *Real Analysis.* Macmillan publishing company, New York, 3rd edition, 1988.

[140] S. Rüdiger, J. Shuai, W. Huisinga, N. Chamakuri, G. Warnecke, L. Parker, and M. Falcke. Hybrid stochastic and deterministic simulations of calcium blips. *Biophys. J.*, 93:1847–1857, 2007.

[141] S. Ruuth. Implicit-explicit methods for reaction-diffusion problems in pattern formation. *J. Math. Biol.*, 34(2):148–176, 1995.

[142] Y. Saad. *Iterative Methods for Sparse Linear Systems,* 2nd ed. SIAM, Philadelphia, 2003.

[143] J. Schnakenberg. Simple chemical reaction systems with limit cycle behavior. *J. Theor. Biol.*, 81:389–400, 1979.

[144] I. E. Segal and R. A. Kunze. *Integrals and Operators,* Grundlehren der Math. Wissenschaften 228. Springer-Verlag, Berlin, 1978.

[145] L. Shampine. *Numerical solution of ordinary differential equations.* Chapman & Hall, 1994.

[146] J. W. Shuai. Optimal intracellular calcium signalling. *Phys. Rev. Lett.*, 88:068102–1–4, 2002.

[147] J. Smoller. *Shock Waves and Reaction-Diffusion Equations.* Springer-Verlag, New York, 1994.

[148] J. Sneyd and J. Keener. *Mathematical Physiology.* Springer, 2009.

[149] J. Sneyd, J. Keizer, and A. Duffy. Travelling waves in buffered systems: Applications to calcium waves. *SIAM J. Appl. Math.*, 58:1178–1192, 1998.

[150] J. Sneyd, B. Wetton, C. Charles, and M. J. Sanderson. Intercellular calcium waves mediated by the diffusion of inositol triphosphate: a two-dimensional model. *Am. J. Physiol.*, 264:C1537–C1545, 1995.

[151] H. Tanabe. *Functional Analytic Methods for Partial Differential Equations.* Marcel Dekker, Inc., New York, 1997.

[152] C. W. Taylor. Inositol triphosphate receptors: Ca^{2+}-modulated intracellular Ca^{2+} channels. *Biochimia and Biophysica Acta*, 1436:19–33, 1998.

[153] D. Thomas, P. Lipp, M. J. Berridge, and M. D. Bootman. Hormone-evoked elementary Ca^{2+} signals are not stereotypic, but reflect activation of different size channel clusters and variable recruitment of channels within a cluster. *J. Biol. Chem.*, 273(42):27130–27136, 1998.

[154] R. Thul and M. Falcke. Release Currents of IP_3 Receptor Channel Clusters and Concentration Profiles. *J. Biophysics*, 86:2660–2673, 2004.

[155] S. C. Tovey, P. de Smet, P. Lipp, K. W. Young, L. Missiaen, H. De Smedt, J. B. Parys, M.J. Berridge, J. Thuring, A. Holmes, and M. D. Bootman. Calcium puffs are generic $InsP_3$-activated elementary calcium signals and are downregulated by prolonged hormonal stimulation to inhibit cellular calcium responses. *J. cell. Science.*, 114(22):3979–3989, 2001.

[156] H.A. van der Vorst. Bi-CGSTAB: A fast and smoothly converging variant of bi-cg for the solution of nonsymmetric linear systems. *SIAM J. Sci. Stat. Comp.*, 13:631–644, 1994.

[157] H. Versteeg and W. Malalasekera. *An introduction to computational fluid dynamics: the finite volume method.* Prentice Hall, 2007.

[158] J. L. Wagner and J. Keizer. Effects of rapid buffers on Ca^{2+} oscillations and Ca^{2+} diffusion. *J. Biophys.*, 67:447–456, 1994.

[159] J. L. Wagner, J. Pearson, and J. Keizer. Simulation of the fertilization Ca^{2+} wave in Xenopus laevis eggs. *J. Biophys.*, 75:2088–2097, 1998.

[160] M. F. Wheeler. An elliptic collocation-finite element method with interior penalties. *SIAM J. Numer. Anal.*, 15:152–161, 1978.

[161] S. Zeller, S. Rüdiger, E. W. Heineken, J. Sneyd, G. Warnecke, I. Parker, and M. Falcke. Modelling of the modulation by buffers of Ca^{2+} release through clusters of IP_3 receptors. *Biophys. J.*, 97(4):992–1002.

[162] J. Zhu, Y. T. Zhang, and S. A. Newman. Application of Discontinuous Galerkin Methods for Reaction-Diffusion Systems in Developmental Biology. *J. Sci. Comput.*, 40:391–418, 2009.

Curriculum Vitae

Personal Information

Name:	**Jared Ouma Okiro**
Date of birth	18.08.1973
Place of birth	Kisumu, Kenya

Education

2011 - 2016	PhD Graduation, Faculty of Mathematics, Otto-von-Guericke University, Magdeburg, Germany
2003 - 2006	M.Sc. (Applied Mathematics), Maseno University, Kenya
1993 - 1997	B. Sc. Education (Honours) in Mathematics and Physics, Moi University, Kenya
1988 - 1991	Kenya Certificate of Secondary Education (KCSE), Olembo Secondary School
1980- 1987	Kenya Certificate of Primary Education (KCPE), Olembo Primary School

Research Publications

- J. Okiro, V. Ssemaganda, Ch. Nagaiah, and G. Warnecke. Global existence of strong solutions for an intracellular calcium dynamics model. *under review.*
- J. Okiro, Ch. Nagaiah, G. Warnecke and M. Falcke. Higher Order Numerical Simulation of Intracellular Calcium Dynamics using Discontinuous Galerkin Methods. *under review.*
- J. O. Okiro, A. W. Manyonge, N. O. Ongati, J. M. Shichikha, and J. K. Kimaiyo. On the Solution of Confined Aquifer Flow Equations : Finite Difference Approximations, Appl. Math. Sci. 7(58), 2885-2896, 2013.

Academic Honours

- SIAM Student Travel Award and Conference registration fee for the SIAM Conference on Dynamical Systems, Snowbird, Utah, USA, May 2013.
- Centro Internazionale Per La Ricera Matematica (CIRM) Grant for the European Conference on "High Order Nonlinear Numerical Methods for Evolutionary PDEs: Theory and Applications", Trento-Italy, April 2011.
- German Academic Exchange Service(DAAD - Deutscher Akademischer Austausch Dienst) PhD scholarship at Otto-von-Guericke University, October 2010 - March 2014.
- African Mathematics Millennium Science Initiative (AMMSI) scholarship for starting PhD in Kenya (2009).
- Kenya Government scholarship for B.Sc. Education (1993 - 1997).